Progress at the Intensity Frontier on Neutrino-Nucleus Interaction Cross Sections and Muon Ionization Cooling

Edward Kevin Perdigão dos Santos

High Energy Physics
Blackett Laboratory
Imperial College London

A Thesis submitted to Imperial College London
in partial fulfilment of the requirements
for the degree of Doctor of Philosophy
and the Diploma of Imperial College

Summer 2014

Abstract

This thesis presents work done in the context of the Neutrino Intensity Frontier. Cross section measurements for charged current coherent pion production by neutrinos and antineutrinos on argon are presented. These measurements are performed using the Argon Neutrino Test (ArgoNeuT) detector exposed to the NuMI beam at Fermilab. The cross sections are measured to be $2.6^{+1.2}_{-1.0}(stat)^{+0.3}_{-0.4}(syst) \times 10^{-38}\text{cm}^2$ per argon nucleus for neutrinos at a mean energy of 9.6 GeV and $5.5^{+2.6}_{-2.1}(stat)^{+0.6}_{-0.7}(syst) \times 10^{-39}\text{cm}^2$ per argon nucleus for antineutrinos at a mean energy of 3.6 GeV. This is the first time this interaction has been measured in argon and the first time it has been measured using an automated analysis.

In the context of the Muon Ionization Cooling Experiment (MICE), the later chapters of this thesis present work concerning the precise tracking of muons in the MICE detectors which will be fundamental for the demonstration of ionization cooling. The relation between MICE, the Neutrino Factory and nuSTORM is explored in the early chapters of this thesis and the physics potential of neutrino beams from the decay of muons is reviewed.

Declaration of Originality

The work presented in this thesis is my own unless stated otherwise.

Chapters 2 and 3 introduce concepts necessary for the understanding of the rest of the text. The sources are a large number of published articles and books which are properly acknowledged.

Chapter 4 presents a cross section measurement at ArgoNeuT. My contribution to this experiment is the analysis presented which uses event reconstruction as developed by the ArgoNeuT collaboration and other LArSoft developers.

Chapter 5 introduces some accelerator concepts and the MICE experiment. The sources are books and articles which are cited. Finally, Chapter 6 describes the construction of a Kalman Filter, a well-known estimator, which is here optimised for the task of track fitting using the MICE scintillating fibre spectrometers.

Copyright Declaration

Contents

List of Tables

List of Figures

Glossary

ADC Analogue to Digital Converter. 50

ArgoNeuT Argon Neutrino Test. 1

CC Charged Current. 27

CCQE Charge Current Quasi-Elastic. 31

CKM Cabibbo-Kobayashi-Maskawa. 4

CP Charge Parity. 5

CVC Conserved Vector Current. 27

EMR Electron-Muon Ranger. 93

FFAG Fixed-Field Alternating Gradient. 19

FSI Final State Interactions. 34

genie Generates Events for Neutrino Interaction Experiments. 49

KL KLOE-like scintillating fibre detector. 93

LarSoft Liquid Argon Software. 49

LArTPC Liquid Argon Time Projection Chamber. 48

MICE Muon Ionization Cooling Experiment. 1

MINOS Main Injector Neutrino Oscillation Search. 45

NC Neutral Current. 27

NuMI Neutrinos from the Main Injector. 45, 48

nuSTORM Neutrinos from Stored Muons. 1

PCAC Partially Conserved Vector Current. 27

PID Particle Identification. 51

PMNS Pontecorvo-Maki-Nakagawa-Sakata. 4

POT Protons On Target. 46

SciFi Scintillating fibre detector. 92

TOF Time-Of-Flight. 92

TPC Time Projection Chamber. 48

Acknowledgements

A scientist, like an artist, is not immune to the influences exercised over him. The work shown in this thesis is the result of the sum of experiences I have lived. I wish to take this occasion to acknowledge people who I met and who somehow contributed to shape my work and my opinions. I was fortunate to meet so many bright and kind people who have inspired me.

First of all I would like to thank my supervisor, Ken Long, for drawing the program that filled three and a half years of my life. In particular, I would like to thank him for giving me the opportunity to work in such variate experiments – MICE, nuSTORM, ArgoNeuT. Ken wins the hearts and minds of the people who surround him and I greatly enjoyed every discussion we ever had.

Henrique Araujo was important during my transition from a master student to a Ph.D. student and has been a friend since those days. I owe him my first publication. Without his efforts it would either not happen or be of much less quality.

During my first few months with the MICE tracker team, I had the privilege to work closely with Alan Bross, Paul Rubinov and David Adey for the tracker cosmic tests. That was a gratifying experience during which I grew a lot. I was lucky to keep meeting Alan every time I visited Fermilab, I have great admiration for him.

I am also thankful to Chris Tunnell and Chris Rogers for all coding advice they gave me and for their efforts to build a software framework for the MICE collaboration. With Ian Taylor I had a lot of fun working on nuSTORM cross section studies while in Vietnam. His experience, brightness and sense of humour made the experience enjoyable and useful. I would also like to thank Jean-Baptiste Lagrange and Jaroslaw Pasternak for helping me understand accelerator concepts and sorting out any doubts I ever had about the nuSTORM or MICE beam lines.

I was lucky enough to be granted two placement periods at Fermilab. Regarding the first, I am particularly indebted to Brian Rebel. His support was fundamental for the writing of the cross section studies for the nuSTORM PAC proposal. Jorge Morfin was also a mentoring figure which I greatly value and which I wish had spent more time with. In the same way, I also regret not having used Morgan Wascko more. I still thank him for always being so open to talk to me and for offering spot-on advice or comments.

During my second visit to Fermilab, I was working with the ArgoNeuT collaboration. This was the best time of my Ph.D. I was very lucky to meet such an incredible group of people such as Ornella Palamara, Flavio Cavanna, Mitch Soderberg, Eric Church, Bonnie Fleming, Sam Zeller, Rob Acciarri, Anne Schukraft. Teaming up with Tingjun Yang in order to produce our cross section measurement was an experience I highly enjoyed and during which I learned a lot. I am very thankful to Tingjun for his mentoring and his friendship.

I wish to thank Aparna Ashok for her companionship and for all the experiences we shared. I also want to thank my family for always supporting me the best they could.

All of the above, who have touched me with their brilliance or kindness, have my most heartfelt appreciation.

I acknowledge the support from Fundação para a Ciência e Tecnologia, through the grant SFRH/BD/69814/2010.

1 Introduction

1.1 The Contents of this Thesis

The recent years have been rich in cornerstone discoveries in Particle Physics. The year of 2012 was marked by the measurement of θ_{13} and 2013 by the discovery of the Higgs boson at the LHC. While these are significant steps towards the completion of the Standard Model, there are still fundamental questions that are unanswered, many of these belonging to the neutrino sector.

This thesis comprises work done in two different experiments, Argon Neutrino Test (ArgoNeuT) and Muon Ionization Cooling Experiment (MICE), which are, each in their own way, breaking ground in the neutrino Intensity Frontier. A consensual statement that can be made at the time of this writing is that the pathway to a better understanding of the neutrino sector comprises better knowledge of neutrino cross sections and better neutrino beams. The unfolding of the physics in the neutrino sector can only be achieved from the analysis of neutrino oscillation data if the uncertainties associated to the neutrino beam and the interaction cross sections are controlled.

Chapters 2 and 3 contain the neutrino physics theory necessary for the understanding of the rest of this thesis. These chapters cover the domains of neutrino mixing and neutrino interactions with matter, making an overview of the basic formalism and the main experimental results to date. The production of neutrino beams in accelerator experiments is reviewed. The alternatives to the state-of-the-art accelerator beams are presented, with particular attention being given to the Neutrino Factory and Neutrinos from Stored Muons (nuSTORM) concepts.

The physics opportunities at nuSTORM are briefly discussed in Chapter 2 and resumed later in Chapter 3 where the potential for cross section measurements is emphasised. The length of the discussion concerning the Neutrino Factory and nuSTORM facilities is a consequence of the authors involvement in the nuSTORM project and of the relation between the Neutrino Factory and the MICE experiment. Chapter 4 presents a cross section measurement of charged current coherent pion production using the ArgoNeuT detector.

Chapter 5 introduces some accelerator concepts culminating with the description of the ionization cooling technique and the experiment designed to demonstrate it, MICE. Chapter 6 shows work done towards the precise tracking of muons in MICE's scintillating fibre spectrometers, which will be fundamental for the success of the experiment.

2 Neutrino Mixing

Due to the illusive nature of neutrinos granted by their charge and colour neutrality, the history of Neutrino Physics has been rich in mysteries. The knowledge built up to the date is a result of decades of effort and we are indebted for it to a large number of experiments observing neutrinos. This chapter presents a review of the fundamental concepts for understanding neutrino mixing and its measurement via the observation of neutrino oscillations. A summary of the results obtained so far is given and current experimental requirements are discussed. The focus in the final sections is on how neutrino beams are currently produced – conventional beams – and what the alternatives are. Special emphasis is given to the Neutrino Factory case.

2.1 Neutrino Mixing

We know today that the neutrinos have non-zero masses and that the leptons mix. There are at least three mass eigenstates, ν_1, ν_2, ν_3, and the three neutrino flavours ν_μ, ν_e, ν_τ result from the quantum-mechanical superposition of the former, although the fraction of each mass eigenstate leading to each flavour state is not known with precision. Experiments studying solar and atmospheric neutrinos have shed some light on the spectrum of the mass eigenstates. We know that two are separated by a small difference and the third is separated from the other two by a larger difference. The way these mass eigenstates are ordered, the *Hierarchy*, is still not known. In one scenario, the closest pair would be at the bottom and the third eigenstate would be at the top. This would resemble the quark and the charged lepton spectra, for which this scheme is known as *Normal*. The other possibility is to have the third mass eigenstate at the bottom, in which case the spectra is referred to as *Inverted*. This is the problem of the mass hierarchy and it is one of the outstanding challenges in the neutrino sector. Moreover, while the mass differences have been measured, the absolute mass value of each mass eigenstate is still unknown. Since there are three mass eigenstates, there are only two independent mass splittings. For historical reasons, we usually refer to $\Delta m_{21}^2 = m_2^2 - m_1^2$ and $\Delta m_{32}^2 = m_3^2 - m_2^2$, known as the "solar" and the "atmospheric" neutrino mass squared differences. The other splitting can be inferred from $\Delta m_{12}^2 + \Delta m_{23}^2 + \Delta m_{31}^2 = 0$. These concepts, of neutrino mixing and mass splittings, are illustrated in Figure 2.1.

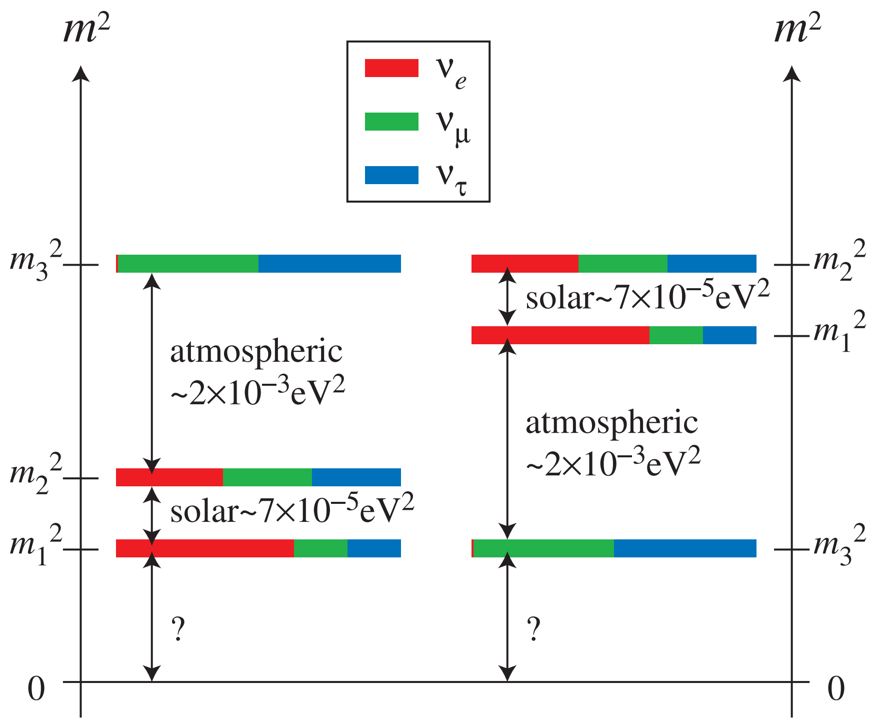

Figure 2.1: Neutrino mass eigenstates in Normal and Inverted order. The splittings Δm_{12}^2 and $|\Delta m_{23}^2|$ have been measured but the order – the *mass hierarchy* – is still unknown. In addition, the absolute mass scale of the eigenstates is also unknown. *Figure extracted from* [1].

Formally, the three flavour neutrino mixing is described by a 3×3 mixing matrix known as the Pontecorvo-Maki-Nakagawa-Sakata (Pontecorvo-Maki-Nakagawa-Sakata (PMNS)) matrix or the Leptonic Mixing matrix [2, 3]. It is an analog of the quark Cabibbo-Kobayashi-Maskawa (CKM) mixing matrix [4]. Using the PMNS matrix, one can relate mass and flavour eigenstates:

$$\begin{bmatrix} \nu_1 \\ \nu_2 \\ \nu_3 \end{bmatrix} = \begin{bmatrix} U_{e1}^* & U_{\mu 1}^* & U_{\tau 1}^* \\ U_{e2}^* & U_{\mu 2}^* & U_{\tau 2}^* \\ U_{e3}^* & U_{\mu 3}^* & U_{\tau 3}^* \end{bmatrix} \begin{bmatrix} \nu_e \\ \nu_\mu \\ \nu_\tau \end{bmatrix} . \tag{2.1}$$

The mixing matrix is expected to be unitary, otherwise the mixing would not conserve the number of neutrinos because the particle number depends on the square of the amplitude of the mixing terms. We can decompose the PMNS matrix in four parts, separating the three rotation angles θ_{23}, θ_{13}, θ_{12} and the Charge Parity (CP)-violating phases ϕ_2, ϕ_3 and δ:

$$\begin{aligned} U = &\begin{bmatrix} 1 & 0 & 0 \\ 0 & c_{23} & s_{23} \\ 0 & -s_{23} & c_{23} \end{bmatrix} \begin{bmatrix} c_{13} & 0 & s_{13}e^{-i\delta} \\ 0 & 1 & 0 \\ -s_{13}e^{i\delta} & 0 & c_{13} \end{bmatrix} \begin{bmatrix} c_{12} & s_{12} & 0 \\ -s_{12} & c_{12} & 0 \\ 0 & 0 & 1 \end{bmatrix} \begin{bmatrix} 1 & 0 & 0 \\ 0 & e^{i\phi_2/2} & 0 \\ 0 & 0 & e^{i\phi_3/2} \end{bmatrix} \\ = &R(\theta_{23})U(\theta_{13},\delta)R(\theta_{12})U(\phi_2,\phi_3) \end{aligned} \tag{2.2}$$

where, for concision, $s_{ij} \equiv \sin\theta_{ij}$ and $c_{ij} \equiv \cos\theta_{ij}$. The rotation angles θ_{23}, θ_{13}, θ_{12} are constrained to the interval $[0, \pi]$ because only squares of the mixing matrix will enter into observable quantities, thus making the change in sign brought to the matrix by an angle $\theta = \theta + \pi$ indistinguishable. The CP violating phases can have any value in $[0, 2\pi]$. The phases ϕ_2 and ϕ_3 are non-zero only in the case of the neutrinos being Majorana particles – i.e., their own antiparticles. Experiments observing neutrino oscillations are insensitive to them, they are the subject of interest of experiments measuring double beta decay. They will not be mentioned again in this text.

The matrix decomposition presented is interesting because it separates terms logically (and experimentally) related. R(θ_{23}) and R(θ_{12}) are rotation matrices between the neutrino states in index. As will be shown later, the θ_{12} angle was measured by experiments studying solar neutrinos, θ_{23} by atmospheric experiments and θ_{13} was recently measured by the T2K [5] and Daya Bay [6] collaborations. The elements of the CKM matrix have been known for many years and it was anticipated that the leptonic mixing matrix would be similar, but it is not. While CKM matrix is uniform along the diagonal and small or very tiny off the diagonal, the PMNS matrix has elements which are large everywhere. The fact that the two matrices look so different puzzles the theoretical community.

However, the greatest reason for interest in the measurement of the PMNS matrix elements is the CP violating phase δ, commonly referred to as δ_{CP}. This phase enters physics through θ_{13}, which is relatively large. CP violation in the leptonic sector is of the uttermost importance as it may play a fundamental role in the generation, via leptogenesis, of the baryonic asymmetry observed in the Universe (see reference [7] for an introductory text on the subject). A measurement of δ_{CP} is the most relevant goal of the physics program of the neutrino sector, but also a difficult one which requires many advance in the whole field. New facilities, whether based on current designs or entirely new ideas are in order. Better understanding of the interaction of neutrinos with matter – see Chapter 3 – will also be required so that the systematic uncertainties are compatible with the precision necessary for this measurement.

2.1.1 Constrains on Neutrino Number and Total Mass

The number of neutrinos, so far assumed to be three in order to match the number of charged leptons, has been constrained by collider and cosmological data.

At the Large Electron Positron (LEP) collider $e^+ + e^-$ collisions were observed and the production of the Z boson was measured. The total width of the Z resonance is the sum of the visible width, from Z decays to quarks and charged leptons, and the invisible width, from the decay into neutrino species with mass less than half of the Z mass. This number was used to constrain the number of active *light* neutrino eigenstates. It was found to be 2.984 ± 0.008 [8]. This measurement can't be used to constrain the existence of hypothetical heavier or *sterile* neutrino species, i.e., neutrinos that don't couple to the weak gauge bosons.

Notably, cosmological data has also been used to constrain the number of neutrino species and the sum of their masses. An explanation of how the radiation density and the cosmic matter density can be used to constrain these values can be found in reference [9]. The *effective* number of neutrinos,

N_{eff}, determined by these experiments consists of the number of neutrinos, active or sterile, that were light enough ($< 10\,\text{eV}$) to be relativistic in the early Universe. Combining the Planck measurements [10] with other notable datasets [11–15], estimations of N_{eff} have been presented. Although the exact estimation depends on the choice of experiments that are combined, $N_{eff} = 3$ is favoured. However, $N_{eff} = 4$, which would add one light sterile neutrino, is not ruled out. A combined analysis is also used to place an upper bound on the sum of the neutrino masses which is estimated to be less than $0.230\,\text{eV}$ to 95% confidence level [10].

2.2 Neutrino Oscillations

Neutrino oscillations are a manifestation of neutrino mixing. They were first suggested by Bruno Pontecorvo [16] in 1967, eleven years after the experimental discovery of neutrinos by Cowan and Reines [17]. Experiments observing atmospheric, solar, reactor or accelerator neutrinos have offered compelling evidence that neutrinos change flavour while they travel. From the study of these oscillations, the mixing angles and the squared mass differences of the mass eigenstates can be determined. In this section, the formalism of neutrino mixing is presented and the oscillation probability is described [18].

At the moment of its creation, a neutrino of flavour $\alpha = \{\mu, e, \tau\}$ can be decomposed in terms of the mass eigenstates as:

$$|\nu_\alpha(0)\rangle = \sum_{i=1}^{3} U_{\alpha i} \, |\nu_i\rangle \,, \tag{2.3}$$

where the sum runs over the mass eigenstates $i = \{1, 2, 3\}$ and $U_{\alpha i}$ are complex conjugates of the matrix elements introduced in 2.1. The evolution of the weak flavour state for later times t can be written using the time propagator:

$$|\nu_\alpha(t)\rangle = \sum_{i=1}^{3} e^{-iE_i t} U_{\alpha i} \, |\nu_i\rangle \,, \tag{2.4}$$

where $E_i = \sqrt{p_i^2 + m_i^2}$ is the energy of the i^{th} mass eigenstate. The probability of oscillation from one weak eigenstate to another (α') is found by taking the square of the quantum mechanical amplitude for that transition:

$$P_{osc}(\nu_\alpha \to \nu_{\alpha'}) = |\langle \nu_{\alpha'} | \nu_\alpha \rangle|^2 \,, \tag{2.5}$$

where, using the orthogonality between mass eigenstates, $< \nu_i | \nu_j >= \delta_{ij}$, the amplitude is:

$$\begin{aligned} \langle \nu_{\alpha'} | \nu_\alpha \rangle &= \sum_{i,j}^{3} \langle \nu_i | \, U^\dagger_{i\alpha'} e^{-iE_i t} U_{\alpha j} \, | \nu_j \rangle \\ &= \sum_{i}^{3} e^{-iE_i t} U_{\alpha i} U^*_{\alpha' i}. \end{aligned} \tag{2.6}$$

Assuming propagation in vacuum, a relativistic neutrino of momentum $p \approx E$ and a traveled distance L, the probability of oscillation is:

$$\begin{aligned} P_{osc}\left(\nu_\alpha \to \nu_{\alpha'}\right) &= \left| \sum_i U_{\alpha' i} \exp\left(-i \frac{\Delta m^2_{ki} L}{2E}\right) U^*_{\alpha i} \right|^2 \\ &= \left| \sum_{i \neq k} U_{\alpha' i} \left(\exp\left(-i \frac{\Delta m^2_{ki} L}{2E}\right) - 1 \right) U^*_{\alpha i} + \delta_{\alpha' \alpha} \right|^2 . \end{aligned} \tag{2.7}$$

The oscillation probability is simplified when admitting that the oscillation happens between only two weak states, which is a good approximation for a number of experiments. In this case, we obtain:

$$P_{osc}\left(\nu_\alpha \to \nu_{\alpha'}\right) = \sin^2\left(2\theta\right) \sin^2\left(1.27 \Delta m^2 \frac{L(\mathrm{km})}{E(\mathrm{GeV})}\right). \tag{2.8}$$

The oscillation probability is now easier to understand. The mixing angle, θ, determines how different the weak states are from the mass states. If θ is zero, no oscillation can happen, the weak states are conserved and equal to the mass states. If $\theta = \pi/4$, the mixing is maximal and at some point all ν_α convert into $\nu_{\alpha'}$. In experiments using artificial neutrino sources, the L/E ratio must optimised by the design of the experiment so that the oscillation probability is maximised at the detector location.

2.2.1 Matter Effects

The probability of oscillation 2.7 assumes propagation in vacuum. In the presence of matter [19], all neutrinos can interact with the medium via Z^0 exchange. However, electron neutrinos have the additional possibility of exchanging charged $W^{\pm}$ bosons with the surrounding electrons. Therefore, the electron neutrino electro-weak potential changes differently relatively to the other flavour eigenstates. The difference in the potential is:

$$V_e = G_F \sqrt{2} N_e; \tag{2.9}$$

where N_e represents the local electron density and G_F is the Fermi coupling constant. The effective mass of electron neutrino becomes:

$$m^2 = E^2 - p^2 = (E + V_e)^2 \approx m^2 + 2EV_e. \tag{2.10}$$

So the difference relatively to the vacuum mass is:

$$\Delta m_M^2 = 2\sqrt{2} G_F N_e E. \tag{2.11}$$

The patterns of oscillation are, therefore, modified. The modification is also dependent on the density profile the neutrinos transverse. For a medium of constant density, the oscillation probabilities have the same form, with the mass squared difference being replaced by the effective mass-squared difference. In the case of a medium with varying density new effects arise. Moreover, the calculation becomes particularly extensive if sterile neutrinos or new, non-standard, neutrino interactions are admitted.

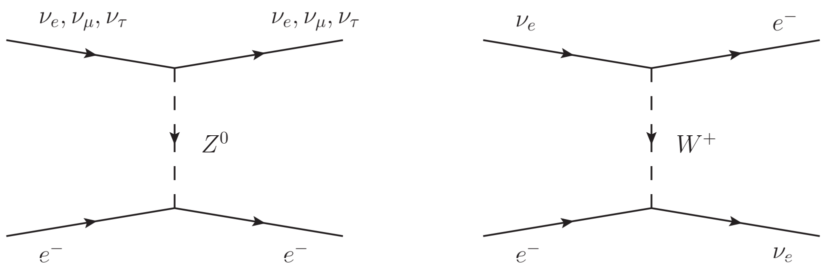

Figure 2.2: Feynman diagrams for neutral and charged current interactions of neutrinos with electrons. While all neutrino flavours can interact with the electrons of the environment via neutral current exchange (left), only the electron neutrinos can exchange charged currents (right).

2.3 Neutrino Sources

The measurement of all the neutrino properties mentioned so far is not possible without very intense neutrino sources. It is common to list neutrino sources in two groups: natural sources and artificial sources.

The highest intensity natural sources of neutrinos are extra-terrestrial. Most of the neutrinos that travel through the Earth are produced in the Sun as a result of the thermonuclear fusion reactions at its core. The main reaction source is proton fusion, $p+p \rightarrow d+e^{+}+\nu_e$, which accounts for about 86% of the solar neutrinos. The whole fusion chain into heavier elements is well understood, which means that the resulting neutrino spectra can be predicted with good precision – see Figure 2.3 from John Bahcall [20].

At the same time a precise estimation of the solar-neutrino flux was obtained, an experiment was built to measure it, the Homestake Solar Neutrino Detector [21], via the observation of the inverse beta decay reaction $\nu_e +^{37} Cl \rightarrow^{37} Ar + e^-$. The observed event rate was one third of that expected and this puzzling observation became celebrated as the "Solar Neutrino Problem". It would lead to the discovery of neutrino oscillations: the electron neutrinos oscillate into muon neutrinos while travelling from the Sun to the Earth.

Another natural source is atmospheric neutrinos. Atmospheric neutrinos are created by the interaction of cosmic rays in the upper layers of the atmosphere producing pions and muons that decay into neutrinos. The

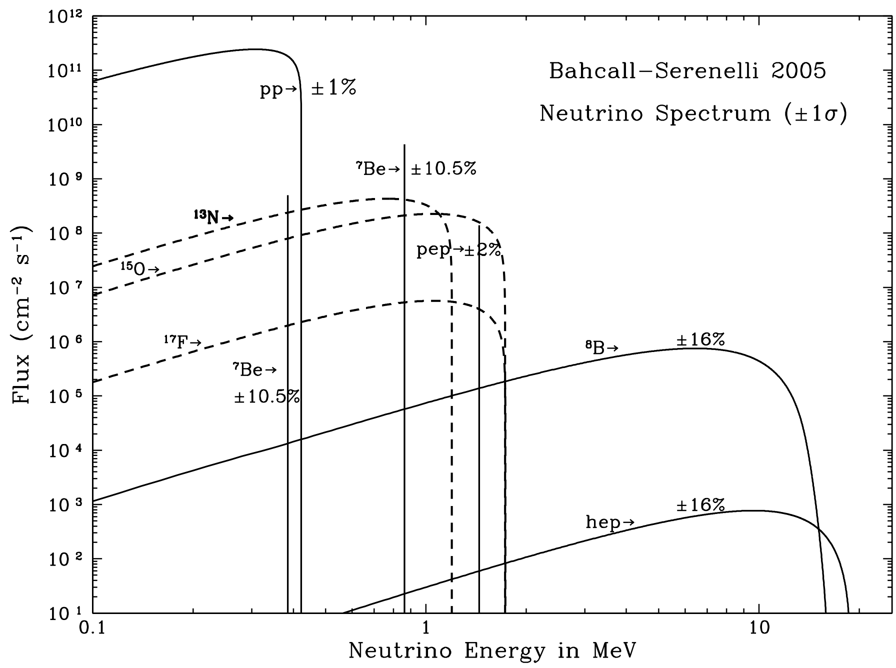

Figure 2.3: The solar neutrino spectrum, John Bachcall's solar model [20]. The disagreement between the Bachcall's prediction of the solar neutrino spectrum and the measurements at the Homestake Solar Neutrino Detector [21] are the basis of the Solar neutrino problem.

energy spectra of these neutrinos can also be estimated [22]. Although the uncertainties in this case are higher, they cancel out when estimating the expected ratio of electron to muon neutrinos that are produced: the number of muon neutrinos created is expected to be twice the number of electron neutrinos. The uncertainty associated to this ratio is 5% [23]. The ratio observed showed fewer muon neutrinos that expected and this was believed to be due to $\nu_\mu \to \nu_\tau$ oscillations. The ratio of muon to electron neutrinos is expected to be ~ 2, but a deficit of muon neutrinos was found – this is know as the "Atmospheric Neutrino Problem". The Super-Kamiokande collaboration would measure the zenith angle dependance of the deficit, finding it consistent with $\nu_\mu \to \nu_\tau$ oscillations [24].

Cataclysmic events such as a supernova collapse produce a brief emission of neutrinos which outshines any other source. In 1987, such a burst occurred in the Large Magellanic cloud, the supernova SN1987A. The neutrinos created induced short periods of great activity in the Kamiokande [25] and IMB [26] water Cherenkov detectors. Although intense, these bursts are rare and their appearance unpredictable so they cannot be relied upon for continuos research. The list of natural sources of neutrinos wouldn't be complete without mentioning geo-neutrinos, which are electron neutrinos created by the β-decay of heavy elements inside the Earth and relic neutrinos which are a remnant of the early Universe just after the Big Bang, just like the cosmic microwave background. Although the flux of geo-neutrinos is very small, it still contributes with a measurable background to some neutrino experiments. The density of relic neutrinos is estimated as $340\,\nu$ cm^{-3} and they are assumed to be nearly at rest.

Artificial or man-made sources consist of reactor and accelerator neutrinos. At nuclear reactors, antineutrinos are produced from the β-decay process $n \to p + e^{+} + \bar{\nu}_e$. The neutrinos are emitted isotropically so the flux decreases with the square of the distance between the reactor and the detector. The energy of the antineutrinos produced is low, $< 10\,\mathrm{MeV}$. Finally, neutrinos can also be produced in dedicated accelerator experiments with some degree of control over the energy spectra and flavour content of the neutrinos that are produced. The production of these starts with the creation and acceleration of a proton beam onto a target where mesons are created. The mesons are captured using magnetic lenses and form a beam. Once the mesons decay, a neutrino beam is created. The set of stages just described are those usually employed at conventional-facilities. More detail will be given on these later and on the proposals for new facilities where the quality of the neutrino beams produced is improved.

2.4 Experimental Anomalies or The Case for Sterile Neutrinos

The theory outlined so far admits the existence of three neutrino mass eigenstates. However, there are experimental hints that suggest other light mass eigenstates might exist that do not incur in weak interactions. These hypothetical particles are known as *sterile neutrinos.* From the experimentalist's point of view, the sterile neutrino hypothesis is born from a set of experimental anomalies measured with low significance.

The first experimental hint of extra neutrino mass eigenstates came from the LSND (Liquid Scintillator Neutrino Detector) experiment [27]. Using a water filled tank doped with scintillator, LSND aimed at measuring a short baseline oscillation (30 m) of $\bar{\nu}_\mu \to \bar{\nu}_e$. At this oscillation length, the experiment was sensitive to a mass-squared splitting $\Delta m^2 \approx 1\,\mathrm{eV}^2$. An excess of $\bar{\nu}_e$ events was found and the best fit suggested a mass splitting of $\sim 1.2\,\mathrm{eV}^2$ [28]. This value is incompatible with the three mass splittings known which are 3 to 5 orders of magnitude smaller, suggesting the existence of at least one new sterile neutrino specie. In order to test the LSND result, another short-baseline experiment was setup to look for ν_e appearance: MiniBooNE (Booster Neutrino Experiment). This time, excesses in both $\nu_\mu \to \nu_e$ and $\bar{\nu}_\mu \to \bar{\nu}_e$ were found, but at a different energy scale [29, 30]. More stress with the LSND result was added by the KARMEN collaboration, an experiment similar to LSND which failed to observe the excess of electron neutrinos [31].

There are also hints of sterile neutrinos in reactor experiments. These became celebrated as the "Gallium Anomaly" from the GALLEX and Sage experiments [32], both counting the rate of conversion $^{71}Ga+\nu_e \to^{71} Ge+e^-$ and the "Reactor Antineutrino Anomalies" [33], from multiple experiments counting the rate of inverse decays $\bar{\nu}_e + p \to n + e^+$ (see Figure [33]). The number of electron antineutrinos measured in these experiments is below the expectation. Their results are consistent with scenarios with one or even two sterile neutrinos, usually referred to as the $3+1$ or $3+2$ scenarios.

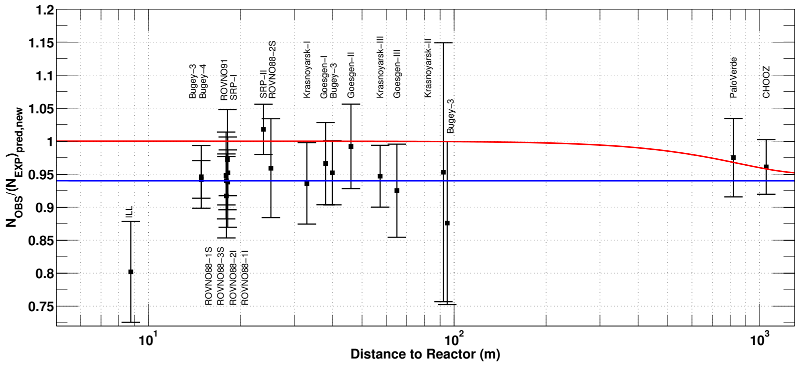

Figure 2.4: Experimental results which embody the Reactor Antineutrino Anomaly. The red line represents a three neutrino mixing solution, the blue line consists of a solution where a fourth neutrino mass state is added, with a mass splitting bigger than $1\,\mathrm{eV}^2$. *Extracted from* [33].

2.5 Summary of Experimental Results

Experiments observing solar, atmospheric, reactor and accelerator neutrinos have determined the parameters of the mixing matrix to the level of precision shown in Table 2.1. The remaining unmeasured parameters are δ_{CP} and the sign of Δm^2_{32}, which fixes the hierarchy of the neutrino masses. However, better precision in the measurement of the mixing angles is desirable. There is also some experimental hints of the existence of sterile neutrino species which requires investigation. Although there is much controversy, due to the low significance of the anomalies observed, the contradiction between accelerator-based experiments and the constraints emerging from cosmological data, the existence of sterile neutrinos is still a possibility.

Table 2.1: Current knowledge of the PMNS matrix parameters. Values are extracted from the 2013 edition of the Particle Data Group review [4].

Parameter	Measured Value
$\sin^2(2\theta_{12})$	0.857 ± 0.024
$\sin^2(\theta_{13})$	0.095 ± 0.010
$\sin^2(\theta_{23})$	$0.950^{+0.035}_{0.036}$
δ_{CP}	unknown
Δm^2_{21}	$(7.50 \pm 0.20) \times 10^{-5}\,\mathrm{eV}^2$
$\lvert\Delta m^2_{32}\rvert$	$(2.32^{+0.12}_{-0.08}) \times 10^{-3}\,\mathrm{eV}^2$

2.6 Current Experimental Requirements

It is accepted that a measurement of mass hierarchy is within reach of experiments operating in the near future. To cite some of these experiments, there is PINGU [34] measuring atmospheric neutrinos, Daya Bay II [35] which is a medium baseline reactor experiment and NOνA [36], a long baseline accelerator experiment.

At the same time, the upcoming experiments will also be able to increase the precision with which the oscillation parameters are known. However, sensitivity studies suggest that measuring δ_{CP} might be out of the reach of any experiment in the near future. The experimental probe for the δ_{CP} measurement are the oscillations $\overset{(-)}{\nu}_{\mu,e} \rightarrow \overset{(-)}{\nu}_{e,\mu}$. The determination of the relative ratio of the oscillation probabilities is affected not only by the δ_{CP} phase but also by matter effects. A successful measurement will require precise knowledge content of the un-oscillated neutrino beam.

In the best of scenarios, an experiment like NOνA could measure δ_{CP} with a significance level of 1.74σ – see Figure 2.5. It is most likely that the measurement of δ_{CP} will not be possible with any of the neutrino sources we know today and will require the construction of a new class of neutrino facility.

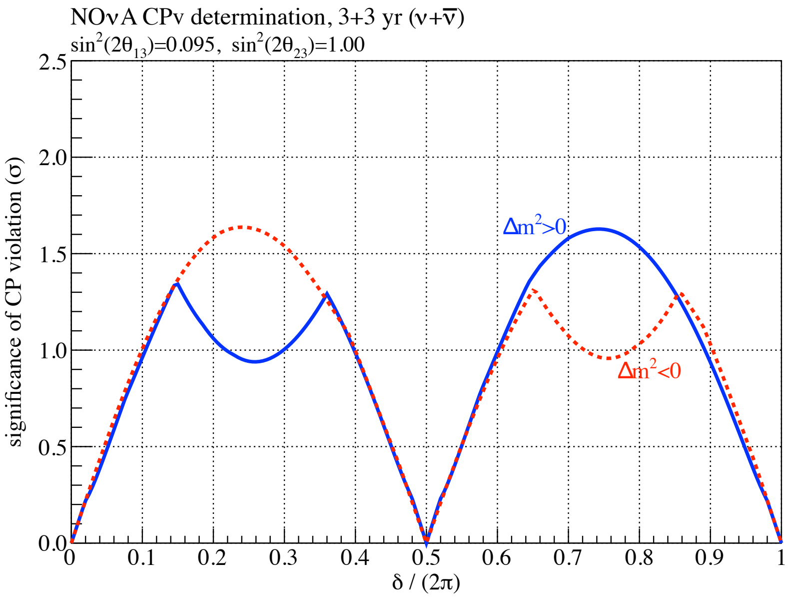

Figure 2.5: Significance with which NOνA can establish CP violation ($\delta_{CP} \neq 0,\ \pi$) for the given values of $sin^2(2\theta_{13})$ and $sin^2(2\theta_{23})$ as a function of delta. This assumes a nominal 3+3 year run plan. The blue solid (red/dashed) curve shows the sensitivity given a normal (inverted) hierarchy. It is instructive to look at the bi-probability plots together with this figure to understand the dips. NOνA will be the first experiment to provide constraints on delta, but NOνA will have a difficult time firmly establishing CP violation after a 6-year run. In the best-case scenario, the significance of the measurement is 1.74 sigma ($\sim$ 92% C.L.) *Figure and caption from "Nova Official Plots and Figures"* [37].

2.7 Conventional Neutrino Beams

The current generation of accelerator experiments, which we can refer to as *conventional beams*, employ a proton beam colliding with a target to produce mesons which decay into neutrinos. An in-dept review of the accelerator elements used in conventional neutrino beams can be found in reference [38]. In the case where positively charged mesons are selected, the pion and kaon decays $\pi^+(K^+) \to \mu^+\nu_\mu$ render a ν_μ neutrino beam, typically with about 1% contamination of electron neutrinos coming from the three body decay $K^+ \to e^+\pi^0\nu_e$. An antineutrino beam ($\bar{\nu}_\mu$) can be produced by setting the beam line currents for the selection of the opposite charge mesons. However, the neutrino beam is always far from pure in it's flavour content. In the case of beams in which the muon neutrino content is enhanced by the selection of positive mesons, the contamination from antineutrinos is about 5%; in antineutrino-enhanced beams, the neutrino contamination can be as high as $30 - 50\%$. This is due to the abundance of positively charged mesons leaving the pion-production target; many of these mesons travel along the axis of the magnetic horns and cannot be excluded from the beam. The contamination with undesired neutrino flavours can be an added difficulty if we cannot determine the charge of the muons produced in the interactions, which usually requires magnetisation of the detector volume. The most important limitations of conventional beams, however, consist in the low neutrino intensity and the large uncertainties in the energy spectrum.

2.8 The Way Ahead

The way ahead for future experiments can follow three different routes. These consist of three different types of facilities that have been proposed. The closest to the current technology is the Superbeam. The Superbeam consists of the upgrade of current accelerator capabilities to a much higher power. LBNE [39] and LBNO [40] are two Superbeam proposals under development at the time of this writing. Another concept is the Beta Beam [41], which consists of accelerating radioactive ions that could provide $\bar{\nu}_e$ and ν_e beams from the decay of different isotopes. Finally, there is the Neutrino Factory proposal [42]. At the Neutrino Factory, the neutrino beam is delivered by the decay in flight of muons $\mu^+ \to \bar{\nu}_\mu + e^+ + \nu_e$. Comparative studies show that the Neutrino Factory delivers the optimal neutrino beam and has the best reach for scientific discovery [43, 44].

2.8.1 The Neutrino Factory

The building blocks of the Neutrino Factory, as suggested in the latest design studies are shown in Figure 2.6. The proton driver may consist of a LINAC or a ring producing a 4 MW proton beam. The proton beam is led to a liquid-mercury target where pions are extracted. The pions are focused using a 20 T super-conducting magnet and transported through a 100 m long decay channel with a 1.5 T solenoidal field. The muon beam, which originates from pion decay, is prepared for acceleration. First, a chicane is used to remove the protons, pions and electrons that contaminate the muon beam. The magnet currents are set so that the muons in the desired momentum range are selected and particles with higher momentum are dumped. This is followed by an absorber which removes the low energy particles. In the following section, the muons meet a straight segment, 33 m long, where Radio-Frequency (RF) cavities bunch the beam, i.e., the muon beam is broken into a sequence of short bunches with a structure defined by the RF frequency. The next part is the phase rotation section. This is a 42 m long segment in which RF cavities are employed to reduce the energy spread of the muons in the beam by slowing down the faster muons and accelerating the slower ones. The sequence of steps from the production of the muon beam until the phase-rotation is referred to as the "muon front-end". The next stage consists of cooling the muon beam. The muons are created with high dispersion and momentum spread and in order to transport and accelerate them, accelerator *cooling* techniques which control the dispersion and angular spread must now come into play. The cooling techniques usually employed are not an option for this purpose, as their application is incompatible with the short muon lifetime. It is well known within the accelerator community that the technique required for reducing the muon beam phase-space is *ionization cooling* [45], which has been proposed but never experimentally demonstrated. This is the purpose of the Muon ionization Cooling Experiment (MICE) [46] which is the subject of the later chapters of this thesis. After the cooling channel, the muons are accelerated to 10 GeV. There are two options for this stage. The first consists of a linac followed by two Recirculating Linear Accelerators (RLAs). The other, is a linac, followed by an RLA and a non-scalling Fixed Field Alternating Gradient (Fixed-Field Alternating Gradient (FFAG)) accelerator. The FFAG option is an experimental concept which is being demonstrated by the EMMA (Electron Model for Many Applications) collaboration [47]. Although it hasn't been demonstrated, it is believed that the FFAG option has the advantage of accelerating the muons faster and having a larger acceptance.

Finally, the muons are injected into the decay ring. The decay of the muons in the straight section of the decay ring produces a neutrino beam oriented towards the far detectors. In the latest proposal, the energy of the neutrino beam is 10 GeV and the oscillation baseline is about 2000 km, which would require to have the ring tilted 10° downwards. The energy spread of the muons in the beam is expected to be only 2%, making the Neutrino Factory a very accurate source of neutrinos.

It is possible, however, to obtain a lower energy but high intensity and accurate neutrino source in a scheme that resembles the Neutrino Factory – i.e., without requiring muon cooling and acceleration. That is the concept of the nuSTORM facility [49].

2.8.2 NuSTORM

NuSTORM (neutrinos from STORed Muons) is a facility currently being proposed for construction. It resembles the Neutrino Factory in that the neutrino beam is generated from the decay of muons. However, at nuSTORM the muon beam is not accelerated, so the facility can be thought of as a *Very Low Energy Neutrino Factory*, and it could be built at this date as it is based only on well demonstrated accelerator techniques. This facility would render a neutrino beam of $\bar{\nu}_\mu$ and ν_e (or ν_μ and $\bar{\nu}_e$) from the decay of μ^+ (μ^-) with a central momentum of 3.8 GeV/c and only 10% momentum spread [49]. The neutrino beam created would be very intense and its flavour content and energy spectra well known.

There are proposals for construction at CERN and Fermilab. In this section, the Fermilab option documented in reference [49] is assumed. The production of the nuSTORM neutrino beam at Fermilab would start with the extraction of the 120 GeV/c protons from the Main Injector (see Fig-

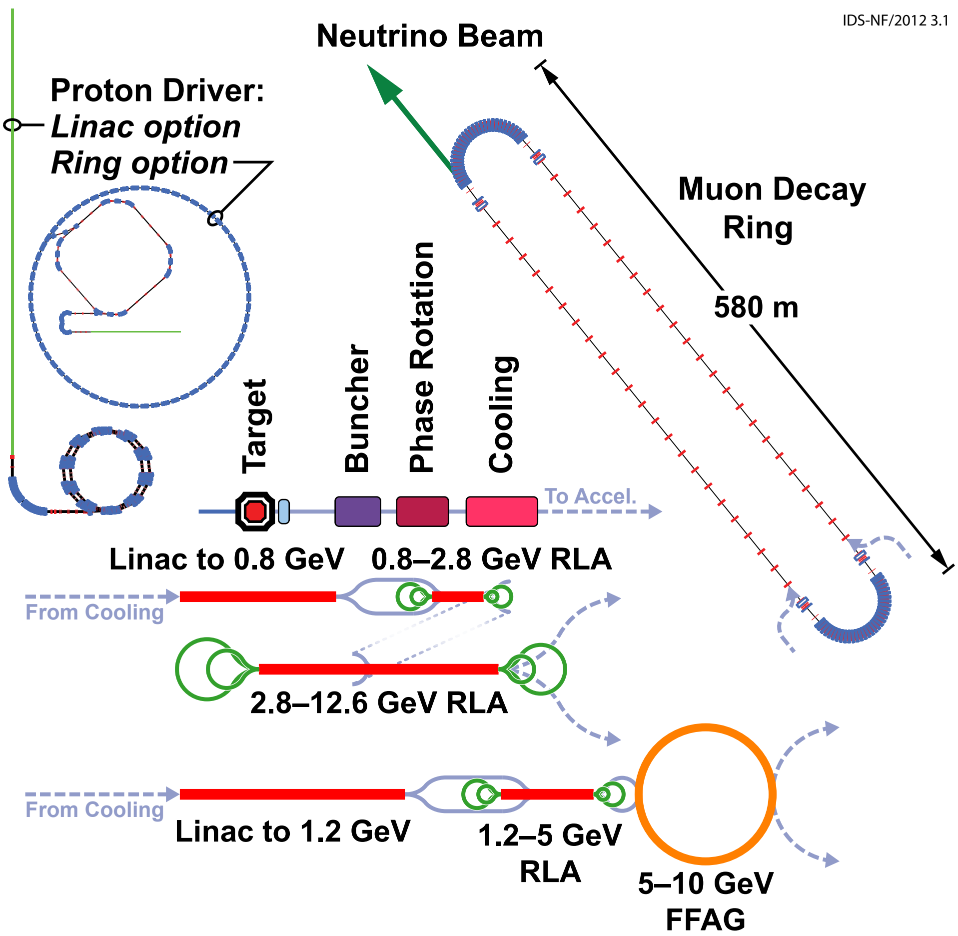

Figure 2.6: Layout of the Neutrino Factory. The different options for the proton driver and the acceleration stage are shown. In the last step, the muons are stored in the decay ring which has a total perimeter of 1300 m, with straight sections 580 m long. The ring would be tilted 10° downwards so that the resulting neutrino beam is pointed at the far detector 2000 km away. This design is a development of the one shown in [48].

ure 2.7). These would be transported to a target hall using six quadrupole

Figure 2.7: The nuSTORM facility as it is conceived at Fermilab. Protons would be extracted from the Main Injector into the nuSTORM target hall. The pions produced at the target would then be led to the storage ring where subsequent decay into muons and then neutrinos would happen. The decay at one of the straight sections would produce a neutrino beam towards the Near and Far Detector halls, located at 50 m and 1 km, respectively. *Figure extracted from* [49].

magnets and four dipole magnets. The currents in these can be tuned to accept protons with energies as low as 60 GeV/c if interesting for experiments. The proton beam would then meet a conventional target followed by a focusing horn for pion capture. The injection of these pions into a decay ring is done in a short beam line in which a chicane is used to introduce momentum selection. The pions injected into the start of the first straight section of the storage ring decay into muons. The pions that haven't decayed before the end of the first straight section are extracted. The design must optimise the ratio of the length of the straight section to the ring circumference in order to maximise the number of useful decays.

The storage ring can be composed of normal and superconducting magnets (FODO option) or Fixed-Field Alternating Gradient magnets (FFAG option). Both designs are explored in reference [49]. The FODO ring is the default option and it is envisaged to have straight sections 185 m long and curved sections with 480 m radius. The momentum acceptance of the muons kept in the ring is 10%. With the FFAG option, only normal-conducting magnets are used. The ring radius needs to be increased to 606 m and the straight sections increased to 240 m, so overall, the ratio of the straight to the ring circumference is increased from 0.39 to 0.40. The big advantage of the FFAG lattice, however, is the fraction of pions accepted per POT, which improves the number of useful decays per POT by a factor of approximately 3.3, although the momentum acceptance in this case is broader, 16%.

Figure 2.8: Momentum distribution of the muons at the end of the first straight section in the FODO lattice. The green box corresponds to the momentum range of the muons kept in the ring; the red box delimits the acceptance for muons to be extracted for ionization cooling R&D. *Figure extracted from* [49].

The nuSTORM collaboration aims at creating a very important impact in three different fronts: short baseline neutrino oscillation to probe sterile neutrinos at the LSND mass scale, neutrino-nucleus cross sections and accelerator R&D towards muon ionization cooling.

The demonstration of ionization cooling, a fundamental step towards a Neutrino Factory or a Muon Collider, is a mission currently in the hands of the MICE collaboration, at the Rutherford Appleton Laboratory. MICE is a single particle experiment, i.e., the beam measurements are made one particle at a time. At nuSTORM, there would be an opportunity to measure ionization cooling using an intense beam. About $\sim 48\%$ of the pions injected into the ring decay before meeting the first arc. The undecayed pions amount to a power of $2\,\mathrm{kW} - 3\,\mathrm{kW}$ so a beam dump is necessary. Using a reflection of the beam combination section used for the pion injection, the pions can be extracted at the start of the first arc. The momentum of these pions is $5 \pm 0.5\,\mathrm{GeV/c}$ and muons at the same energy range are also extracted (see Figure 2.8). These particles can be stopped at some absorber or used for another purpose. The option is to replace the absorber by a degrader which would stop the pions and slow down the muons, producing a low energy muon beam which could be used for an ionization cooling experiment. This muon beam is estimated to have 10^{10} muons per $1.6\,\mu$s spill, with a momentum of $100\,\mathrm{MeV} - 300\,\mathrm{MeV}$.

One of the main motivations for nuSTORM is the light sterile neutrino search. As explored in Chapter 2, there are experimental hints of neutrinos oscillating into sterile species with masses of a few eV. Probing this mass range requires an oscillation experiment with $L(km)/E(GeV) \sim 1$. It is part of the nuSTORM proposal to build a magnetised iron detector very similar to the MINOS type, with iron plates alternating with scintillator. The differences would be thinner plates and larger magnetic field. This would be the Super B Iron Neutrino Detector (SuperBIND), placed at the far detector hall, $\sim 2000\,\mathrm{m}$ away from the end of the straight section of the decay ring. Admitting the accelerator is tuned to produce a $\bar{\nu}_\mu + \nu_e$ neutrino beam, this detector would be used for the appearance search $\nu_e \to \nu_\mu$, which would lead to the detection of muons with the wrong-sign (μ^-) relative to the expected flavour content of the neutrino beam (which should yield only μ^+) and for the disappearance search of $\bar{\nu}_\mu$. The expected signal significance is 10σ.

Finally, there is potential at nuSTORM to make important cross sections measurements. The neutrino beam at nuSTORM would be an unique opportunity for interaction-physics studies, due to its high intensity and the precision with which flavour content and energy spectra are known. The absolute flux scale can also be determined to 1% using instrumentation in the storage-ring. Furthermore, the richness in electron neutrino and antineutrino would be an opportunity for measurements never made before. This topic will be covered in more detail in Section 3.6.1.

2.9 Summary

The basics of neutrino mixing and its measurement through the observation neutrino oscillation have been explored. The creation of neutrino beams at particle accelerators was discussed with special emphasis given to the proposals for new facilities which would use neutrinos from muon decay: the Neutrino Factory and nuSTORM. A conceptual comparison of conventional-beams, MICE, nuSTORM and the Neutrino Factory is shown in Figure 2.9. In the near future, ionization cooling will be demonstrated. However, the large investment required to build a Neutrino Factory is likely to place it decades away from today. Even nuSTORM, despite its modest cost, seems to be out of the picture in the short term. Experiments at conventional beams will remain our learning instrument and collaborations like NOνA *might* bring discovery if δ_{CP} is *large* and the Hierarchy is *just right*. Nevertheless, the complete unfolding of the physics of neutrinos is unlikely to happen without a Neutrino Factory.

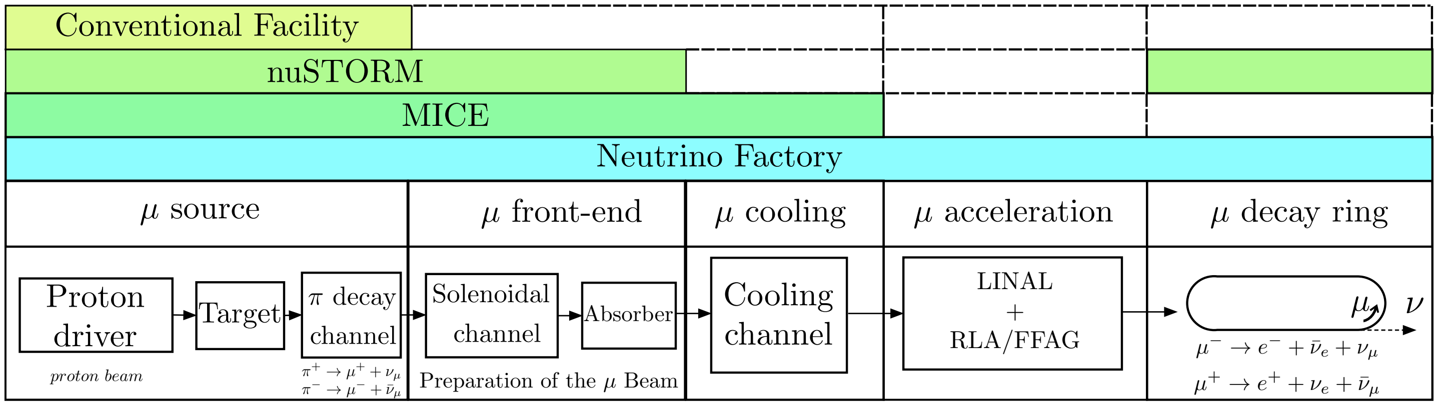

Figure 2.9: Stages of particle production at conventional beams, MICE, nuSTORM and Neutrino Factory facilities. Conventional facilities consist only of the μ source: the neutrino beam comes from the pion decay $\pi^+ \to \mu^+ + \nu_\mu$ or $\pi^- \to \mu^- + \bar{\nu}_\mu$. At MICE, nuSTORM and Neutrino Factory, the muons are prepared for further stage in the μ front-end. At nuSTORM, they are led directly to a decay ring while at the Neutrino Factory they are first cooled and accelerated. With the sole purpose of demonstrating ionization cooling, there is MICE.

3 Neutrino Interactions

The study of neutrino interactions was a fundamental field of research half a century ago, when the electroweak theory was being built. While other particles had their interactions obscured by the other forces, neutrinos were a clean probe used to study the weak force. Nowadays, the community is interested in neutrino interactions mainly as a means to understand neutrino oscillation data better. As neutrino physics moves from discovery to precision measurements, the interactions of neutrinos with matter returns to the spotlight as it will be crucial to reduce the systematic uncertainties affecting future experiments.

Notably, the neutrino energy range at which current and future oscillation experiments are being planned ($\sim 1\,\mathrm{GeV}$) has the peculiarity of not being dominated by a particular interaction channel. Several interaction modes are available in this energy range and the uncertainty on the cross section for each is rather large, typically at the level of 20% [50]. On top of this, nuclear effects contribute to obscure the visible topology of neutrino interactions. This is due to the choice of complex target material (heavy elements) for which the modeling of these effects also suffers from large uncertainties.

In this chapter, a brief review of neutrino interaction physics is presented. For completeness, we start with neutrino-electron interactions and then step into the neutrino-nucleus domain. The tone is that of an experimentalist, so the considerations made are a qualitative overview of the key effects. Special attention will be given to a particular interaction channel: coherent pion production by charged current neutrino-nucleus interactions. This interaction amounts to only a few percent of the total neutrino-nucleus cross section and a measurement of it is presented in the Chapter that follows.

The Chapter ends with some considerations on the difficulties related to cross section measurements using conventional beams. An argument is made for nuSTORM.

3.1 Introduction

For the purpose of describing neutrino interactions, neutrinos can be treated as massless particles. In the electroweak description summarised in this chapter they are considered to be purely left-handed particles and their interactions are mediated by weak charged currents (Charged Current (CC)) which involve the exchange of $W^{\pm}$ bosons and the weak neutral currents (Neutral Current (NC)) mediated by the Z^0 boson. The weak currents conserve flavour and have both vector and axial-vector (V-A) structure which violates parity conservation maximally. Many cross section calculations build up from the conserved vector current (Conserved Vector Current (CVC)) hypothesis [51, 52] and the partially conserved axial current (Partially Conserved Vector Current (PCAC)) hypothesis, which leads to Adler's theorem [53]. The CVC hypothesis, by Feynman and Gell-Mann, implies that because the electromagnetic current is conserved, the weak current is also conserved and can be used to express the neutrino cross sections in terms of electromagnetic form factors which can be obtained from electron scattering through electromagnetic interactions. In a similar way, Adler's theorem, uses the PCAC theorem to relate the cross section for the $\nu + p \to l + X$ interaction with the cross section for $\pi + p \to X$, in the limit where the momentum transfer from the neutrino to the nucleus is zero and the mass of the lepton can be neglected. Using these frameworks, the neutrino cross sections can be estimated from much more abundant electron and pion scattering data, although corrections need to be added as well as some tuning to the neutrino data which should be as precise as possible.

3.2 Neutrino-Electron Interactions

When neutrinos interact with matter they will either interact with an atomic electron or a nucleus. Interactions with electrons are free of the complications brought by the strong interactions. The first observations of neutrino-electron scattering were made at the Gargamelle bubble chamber in 1973 [54] at a mean neutrino energy of $\sim 2\,\mathrm{GeV}$. These consisted of the observation of the forward-scattered electron from the diagrams in Figure 2.2: three $\bar{\nu}_\mu + e^-$ and ten $\nu_\mu + e^-$ events were found. These measurements and the higher statistics ones that would follow provided a confirmation of the

Standard Model at tree level.

The scale (κ) of the cross section values estimated from theory is determined by the Fermi constant, G_f, and the electron's mass m_e:

$$\kappa = \frac{G_F^2 m_e}{(2\pi)} = 4.3 \times 10^{-42}\,\mathrm{cm}^2/\mathrm{GeV}. \tag{3.1}$$

Using a four-fermion interaction approach ($Q^2 << M_W$) the cross sections for neutrinos of energy E_ν are [55]:

$$\sigma(\nu_{\mu(\tau)} + e) = 1.56 \times 10^{-42}\,\mathrm{cm}^2 \frac{E_\nu}{GeV}, \tag{3.2}$$

$$\sigma(\bar{\nu}_{\mu(\tau)} + e) = 1.33 \times 10^{-42}\,\mathrm{cm}^2 \frac{E_\nu}{GeV}, \tag{3.3}$$

$$\sigma(\nu_e + e) = 9.46 \times 10^{-42}\,\mathrm{cm}^2 \frac{E_\nu}{GeV}, \tag{3.4}$$

$$\sigma(\bar{\nu}_e + e) = 3.96 \times 10^{-42}\,\mathrm{cm}^2 \frac{E_\nu}{GeV}. \tag{3.5}$$

$$\tag{3.6}$$

The enhancement of electron-neutrino cross section is due to the CC current contribution which is absent for the other neutrino flavours. These values are in agreement with the experimental data: neutrino-electron interactions are well understood.

3.3 Neutrino-Nucleus Interactions

Neutrino-electron interactions are purely electroweak processes. When we step into the domain of neutrino-nucleus interactions, strong interactions come into play. Modeling this class of interaction is more complex and the approach taken depends on the neutrino energies considered. Commonly, the neutrino-nucleus interactions are divided into a few subprocesses which might be more or less probable, depending on the neutrino energy: coherent, elastic/quasi-elastic, resonant and deep inelastic. This section presents an overview of such processes. A generic CC interaction is shown in Figure 3.1 and some useful parameters are there defined. The four-momentum transferred by the neutrino to the target system is denoted q and its Lorentz invariant is $Q^2 = -q^2 = (p_\nu - k_l)^2$.

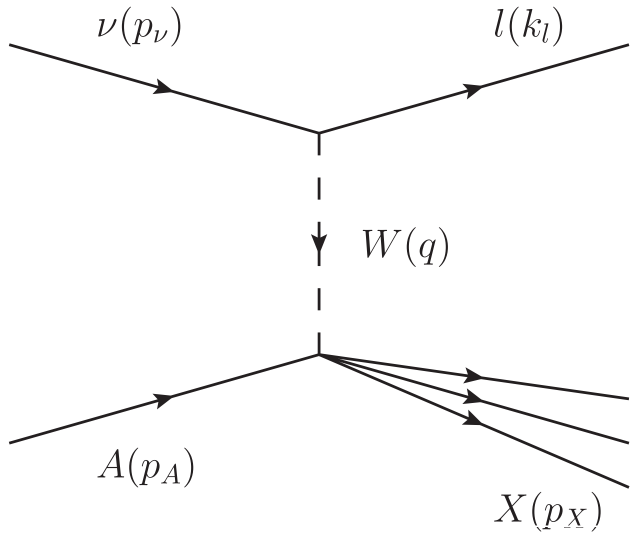

Figure 3.1: Feynman diagram for a generic CC neutrino-nucleus interaction. The difference between the lepton and neutrino momentum, $q = \kappa_l - p_\nu$ is carried by a charged W boson.

3.3.1 Coherent

Coherent $\nu + A \rightarrow \nu + A$ interactions have been postulated [56] but never observed. In this mode, the neutrino interacts with the nucleus as a whole. The Q^2 for the interactions needs to be low, so that the nucleus remains in its ground state and unfragmented. The cross section is well known:

$$\frac{d\sigma}{dT} = \frac{G_F^2}{4\pi} Q_W^2 M \left(1 - \frac{MT}{2E_\nu^2}\right) F(Q^2)^2; \tag{3.7}$$

where T is the recoil energy of the nucleus, M is the mass of the nucleus, E_ν the neutrino energy, G_F the Fermi constant, $Q_W = N - (1 - 4\sin^2\theta_W Z)$ the weak charge of the nucleus and $F(Q^2)$ is the nuclear form factor at momentum transfer Q^2. The neutrino energy domain of this interaction is below 50 MeV. The observable signature, the recoil of a nucleus, is very hard to detect. The maximum recoil energy of the nucleus is $\sim {}^{2E_\nu^2}/_{M}$ which in practice means a few keV, the exact value depending on the nuclear target. Collaborations searching for cold dark matter have analysed the possibility of making this measurement [56–60] and efforts are currently underway to deploy a detector dedicated to finding experimental evidence of this interaction [61].

3.3.2 Elastic and Quasi-Elastic

At the few GeV scale elastic NC and quasi-elastic CC interactions dominate. In the elastic NC, the neutrino scatters elastically off a nucleon whereas in the CC interaction some energy is expended to create the lepton, hence the quasi-elastic (QE) designation – see diagrams in Figure 3.2.

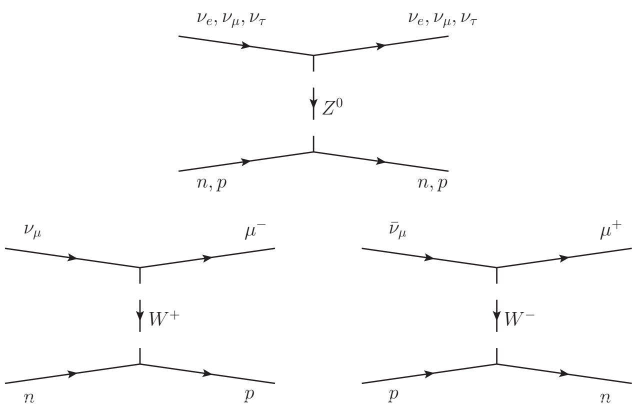

Figure 3.2: Feynman diagrams from neutrino elastic and quasi-elastic interactions.

In NC interactions the only potentially visible signal is the knocked-out nucleon, whereas in CC interactions a lepton is also produced. Neutrino generator codes use a cross section calculated using the Llewellyn Smith formula [62]. In this framework, approximations like the *Fermi Gas model* (used to estimate the nucleon momentum) or the *Impulse Approximation* (the exchange boson is absorbed by one nucleon) are used. The final formula depends on several form factors through which the interaction with the nucleus is parameterised. Most parameters can be extracted from electron scattering experiments. The only free parameter in the cross section models ends up being the axial mass M_A. This is an energy and target independent constant estimated to be around 1.02 GeV from fitting historical data [63–65]. However, more recent data from the MiniBooNE collaboration suggests

Table 3.1: Measured values of M_A.

Experiment	M_A	Reference
BNL+ANL+FNAL	1.02 ± 0.03	[63–65]
K2K	1.200 ± 0.12	[68]
K2K	1.140 ± 0.10	[69]
MiniBooNE	1.350 ± 0.17	[70]
MINOS	1.190 ± 0.17	[71]
NOMAD	1.050 ± 0.06	[72]

a higher $M_A = 1.35\,\text{GeV}$. It has been suggested that the disagreement is a consequence of the Impulse Approximation not being valid at the 1 GeV energy scale [66, 67].

An important feature of Charge Current Quasi-Elastic (CCQE) interactions is the calculation of the neutrino energy which comes directly from the measurement of the outgoing lepton momentum and angle with respect to the neutrino incoming direction. The lepton carries most of the neutrino energy so its track is easy to reconstruct. Oscillation experiments rely on this calculation for the determination of the neutrino energy. Naturally, the presence of backgrounds which mimic the CCQE signal affects not only the estimation of the event rate but also the calculation of the neutrino energy. One of the main difficulties is therefore to correctly tag CCQE events, a problem associated to the use of heavy targets which induce nuclear effects – see section 3.4.

3.3.3 Resonant

As we look to increasing neutrino energies still in the few GeV range, resonance production becomes dominant. The most important hadronic resonance is the $\Delta(1232\,\text{MeV})$ which typically leads to the production of a single pion. Reference [73] presents a complete overview of this process. The experimental data is well described by a cross section formulated in terms of a (V-A) current. If enough energy is available, the production of multiple resonances becomes possible. The cross section for the production of each resonance increases with the neutrino energy until a plateau is reached – see Figure 3.3.

3.3.4 Deep Inelastic Scattering

Beyond resonance production, the Q^2 eventually becomes high enough to break-down the nucleus. This interaction is modelled using parton distribution functions.

While the cross sections for the elastic, QE and pion resonances reach plateaus, the cross section for DIS rises linearly with energy – see Figure 3.3.

The total DIS CC cross sections are:

$$\sigma(\nu + n) = 0.881 \times 10^{-38}\,\mathrm{cm}^2 \frac{E_\nu}{GeV}, \tag{3.8}$$

$$\sigma(\nu + p) = 0.451 \times 10^{-38}\,\mathrm{cm}^2 \frac{E_\nu}{GeV}, \tag{3.9}$$

$$\sigma(\bar{\nu} + n) = 0.250 \times 10^{-38}\,\mathrm{cm}^2 \frac{E_\nu}{GeV}, \tag{3.10}$$

$$\sigma(\bar{\nu} + p) = 0.399 \times 10^{-38}\,\mathrm{cm}^2 \frac{E_\nu}{GeV}, \tag{3.11}$$

and the NC equivalents are:

$$\sigma(\nu + N) = 0.209 \times 10^{-38}\,\mathrm{cm}^2 \frac{E_\nu}{GeV}, \tag{3.12}$$

$$\sigma(\bar{\nu} + N) = 0.115 \times 10^{-38}\,\mathrm{cm}^2 \frac{E_\nu}{GeV}. \tag{3.13}$$

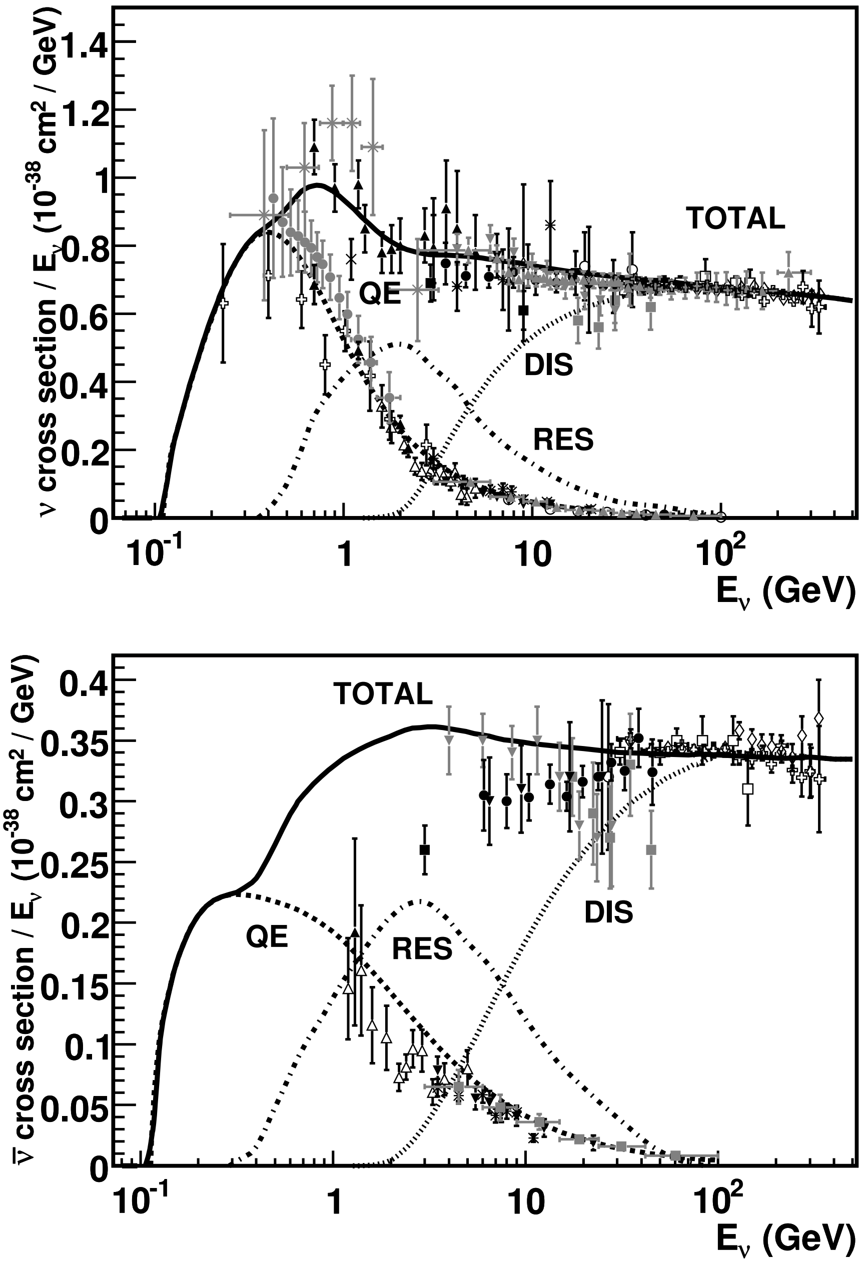

Figure 3.3: Neutrino and antineutrino cross sections divided by neutrino energy in the 100 MeV to 100 GeV range. Existing data is overlaid to the theoretical expectation which is decomposed in the QE, RES and DIS contributions. The successive regimes of QE, RES and DIS dominance can be seen. The plateau the QE and RES cross sections reach corresponds to the linear decrease with energy in this representation. *Figures extracted from* [74].

3.4 Final State Interactions

Experiments measuring or being proposed to measure neutrino interactions have complex nuclear targets, such as carbon, oxygen, iron or argon. As a consequence, the particle products from the neutrino interaction can undergo further interactions with the nuclear environment. These are called final state interactions (Final State Interactions (FSI)) and their effect is hard to measure [50]. Notably, they are the reason why some collaborations choose to present their cross section measurements in terms of final state topology, which means that rather than measuring the cross section for the interaction channel alone, this is folded with the FSI contribution. For this reason, light elements such as hydrogen or helium are ideal target materials.

In Monte Carlo generator codes, FSI effects are added using nuclear cascade models. In these, each particle produced by the neutrino interaction is tracked within the nuclear medium of varying density. The modeling of FSI requires a good understanding of hadronic physics, in particular of π absorption and effective nucleon-nucleon cross sections, which add effective mass corrections and Pauli Blocking[1] to the free nucleon-nucleon cross section. The impact off FSI corrections seems to be particularly important for pions, which can be absorbed, produce other pions, scatter elastically from the nucleons or exchange electric charge with them. It is generally assumed that FSI do not affect the final state lepton.

Progress in the understanding of FSI requires higher precision on the neutrino cross section measurements which they obscure.

3.5 Coherent Pion Production

Coherent interactions may induce π production through both CC and NC processes (Figure 3.4). These interactions are characterised by pions and muons that are forward going with respect to the incoming neutrino direction, a consequence of the low momentum transfer to the target nucleus in the coherent interaction. The following paragraphs summarise some experimental and theoretical background.

[1] Fermi-Dirac statistics do not allow scattered nucleons to move to a state already occupied by other nucleon.

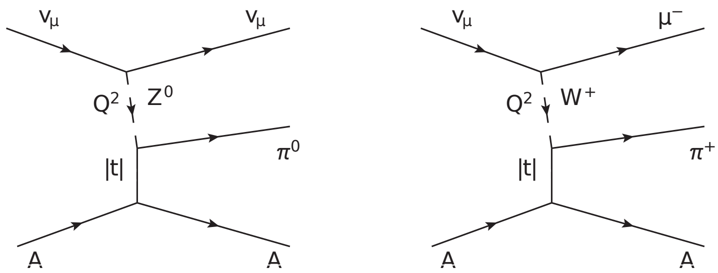

Figure 3.4: Coherent π production from ν_μ. The outgoing pion carries the same charge as the incoming current. The low momentum transfer to the nucleus, $|t| = (q - p_\pi)^2$, is the experimental evidence of this interaction.

3.5.1 Early Theory and Data

During the 60's and the 70's, the coherent production of mesons in neutrino interactions was a subject of interest to several authors working on the description of weak interactions [75–77]. These discussions emphasised that the (V-A) nature of weak currents could be tested by the measurement of an enhancement of the cross sections for forward going pions, which would be a result of the coherent interactions. Lackner [78] produced an estimation of the cross sections based on the PCAC theorem, according to which the cross section for π^0 production off the nucleus could be related to the cross section for π^0 scattering off the same nucleus. Assuming that the πN cross section was independent of the pion energy, Lackner estimated the cross section in Aluminium nuclei to be:

$$\sigma_{coh\pi^0} = 3 \cdot 10^{-40} E_\nu \text{ GeV}^{-1}\text{cm}^2/\text{nucleon}. \tag{3.14}$$

In the early 80's, the neutrino experiments at the CERN-PS, the Aachen-Padova spark chamber and the Gargamelle bubble chamber, observed the predicted excess of low angle π^0 showers [79, 80] at a mean neutrino energy of $\sim 2\,\text{GeV}$. These were reported to be consistent with a NC coherent π^0 production. Following these measurements, Rein and Sehgal [81] extended Lackner's work by employing a parametrisation for the πN cross section derived in their own previous work. The results obtained were in agreement with the measurements made by the Aachen-Padova and Gargamelle collaborations, which Lackner's prediction underestimated by a factor of ~ 5.

Rein and Sehgal also predicted with success the cross section the CHARM experiment ($E_\nu \simeq 30\,\mathrm{GeV}$) would measure [82].

Further measurements of NC coherent pion production would follow and the CC counterpart would be measured as well [83, 84]. The measurements were made at relatively high neutrino energies ($7-100\,\mathrm{GeV}$) and found to be compatible with the Rein-Sehgal (RS) model to the level of their precision.

3.5.2 Late Developments

The modeling of coherent π production met renewed interest when data that couldn't be described by the RS model emerged. In 2005 the K2K experiment, at a neutrino energy of 1.3 GeV, found no evidence of coherent π production [85]. Their limit (at 90% confidence level) was about a factor of two below the RS estimation. The same sort of result came from the SciBooNE experiment, which also published upper limits below the RS prediction at $E_\nu = 1.1\,\mathrm{GeV}$ and $2.2\,\mathrm{GeV}$ [86].

The new results motivated the writing by Berger and Sehgal of a correction that extended the PCAC formalism to low energy neutrino interactions; in this regime, the π mass cannot be neglected. This model, known as the Berger-Sehgal model [87], reduced the RS original prediction and agreed with the K2K and SciBooNE data. However, as pointed out by the authors, it was much lower than a new measurement by MiniBooNE for π^0 production [88] at a neutrino energy of 1.2 GeV. Schalla and Paschos also published a model [89] based on the PCAC theorem which agreed with the MiniBooNE data. Besides all the PCAC based models, microscopic models arose as an alternative approach. These consist in a full quantum mechanical treatment that describes the excitation and decay of the Δ resonance [90–92]. Within the last year, two new measurements of CC coherent pion production have been made – besides the one that will be presented in this thesis, that is. One, uses T2K's ND280 detector [93], although it is not an official T2K result. The other, being presented at the same time of this writing, comes from the Minerνa collaboration [94].

3.5.3 The Whole Picture

Neutrino induced coherent π production is possible via NC and CC exchange. There are PCAC-based models and microscopic models. In the

PCAC-based models, the ratio σ_{CC}/σ_{NC} is equal to two and the cross sections for the interactions of neutrinos or antineutrinos are the same. In the microscopic models, these ratios don't hold exactly: σ_{CC}/σ_{NC} approaches two for energies above 500 MeV but $\sigma_{NC} > \sigma_{CC}$ below that energy; the neutrino cross section is slightly higher than the antineutrino one – see Figure 4 or reference [92]. The dependance with the target effective atomic number is also disputed, although the scaling with $A^{1/3}$ from the RS model is usually assumed by the experimentalists. The predicted $\sigma(E_\nu)$ shape is different between models and, furthermore, the scale of the cross section can also be different by orders of magnitude.

The RS model is the only option available in neutrino generator codes. However, comparison between different generators will still render different results as these use different hadronic data.

Experimental evidence for coherent π production in neutrino-nucleus interactions exists since the operation of the bubble chamber experiments despite the fact that the cross section for these interactions is $\sim 1\%$ of the total neutrino cross section. Data exist for the NC and CC processes and it is summarised in Tables 3.4 and 3.5. The NC process is important because it is a background for the ν_e appearance in oscillation experiments. Due to the well understood ratio between the NC and CC cross sections, the easier to measure CC cross section can be used to gain knowledge of the NC one.

3.6 The Measurement of Neutrino-Nucleus Cross Sections

The measurement of neutrino-nucleus cross sections is affected by many experimental difficulties. The use of complex target materials in the detectors introduces FSI effects (Section 3.4) which are hard to decouple from the neutrino interaction. For this reason, the trend has become to report measurements in terms of observed final state products. For example, rather than report a measurement of $\bar{\nu}_\mu$ CCQE, a collaboration might report the cross section for production of the "final-state topology" $1\mu^+ + 0\pi + N$neutrons. This is a more transparent way of presenting results and, most important, a model-independent one. However, this approach relegates to the theorist the unfolding of the measurement and that is something which requires detector expertise so that, for example, detection and reconstruction efficiencies for different particle types are taken into account. Whichever the approach chosen, model-independency is not easily attained. The improvement in the cross section knowledge seems to be an iterative process where the addition of measurements with improved precision corrects the Monte Carlo estimation of what the next measurement would be. The measurements and predictions should converge to the true values of Nature.

However, the precision on neutrino cross section measurements seems to be bound to remain affected by large uncertainties intrinsic to the neutrino beams used. Conventional-facilities provide beams with broad energy spectrum and the flavour content is not known with precision. Table 3.2 lists recent measurements and systematic uncertainties associated. Even if all other sources of error are suppressed, the beam systematic uncertainties that affect both the cross section mean value estimation and the neutrino energy determination still render the measurements rather imprecise. This feature is transverse to all experiments measuring neutrino-nucleus cross sections.

3.6.1 Neutrino Cross Sections at NuSTORM

The only way of reaching significantly improved precision on cross section measurements is by using better neutrino beams and that is what the nuSTORM facility offers. Furthermore, while muon neutrino and antineutrino interactions have been measured over the years, the electron counterparts haven't. This is due to the lack of an electron neutrino/antineutrino source, which nuSTORM also presents.

Recall from Section 2.8.2 that at nuSTORM the flavour-composition of the neutrino beam will be known (either $\nu_\mu + \bar{\nu}_e$ or respective antiparticles) and the absolute flux will be determined with a precision of 1% using the storage-ring instrumentation. In these conditions, an exercise was performed with the goal of illustrating the potential for cross section measurement at nuSTORM. The discussion is not meant address the detector options, although assumptions of the detector systematics must be reasonable. The HiResMν detector [101] was found to be a suitable choice for this exercise. Table 3.3 lists the design parameters of the HiResMν detector. Under such detector assumptions, the precision on the measurements achievable

Table 3.2: Sources of systematic uncertainties for different experiments [95–100]. The systematic uncertainties are classified as uncertainties related to: the performance of the detector, the Monte Carlo simulation of the experiment and others which might be experiment specific. The "Sub-total" column reports the combination of these uncertainties, added in quadrature. The flux uncertainty is then listed just before the total systematic error.

	Systematic uncertainty (%)					
Experiment	Detector	Monte Carlo	Other	Sub-total	Flux	Total
MiniBooNE NCE ($E_\nu \sim 1$ GeV)	15.6	6.4	–	16.9	6.7	18.1
MiniBooNE CCQE ν_μ ($E_\nu \in 0.2 - 3.0$ GeV)	3.2	15.7	–	16.1	6.9	17.5
MiniBooNE CCQE ν_e ($E_\nu \in 0.2 - 3.0$ GeV)	14.6	8.5	–	16.1	9.8	19.5
MiniBooNE CCπ^0 ν_μ ($E_\nu \in 0.5 - 2.0$ GeV)	5.8	14.4	–	15.6	10.5	18.7
MiniBooNE QE$\frac{d^2\sigma}{dT_\mu d\cos\theta_\mu}$ ν_μ ($E_\nu \in 0.5 - 2.0$ GeV)	4.6	4.4	–	6.4	8.7	10.7
T2K Inclusive ν_μ CC ($E_\nu \sim 1$ GeV)	0.7–12	0.4–9	–	1.3–15	10.9	10.9–18.6
Minerva $\bar{\nu}_\mu$ CCQE ($Q^2 < 1.2$ GeV^2)	8.9–15.6	2.8	2–6	9.6–17	12	15.3–20.8
LSND $\bar{\nu}_\mu p \rightarrow \mu^+ n$ 0.1GeV	5	12	–	13	15	20

Table 3.3: In order to take maximal advantage of the nuSTORM accurate beam the detector errors need to be kept small. The HiresMν small uncertainties [102] make it a suitable detector for this effect. The "Reconstruction" error refers to the track reconstruction error. It is dominated by the proton-reconstruction in the QE event. The "Background" estimate corresponds to the contamination of resonant and DIS events. Finally, the "FSI error" estimation corresponds to the impact of final state interactions on the topology of the measured tracks.

Systematic Error	Contribution (%)
Reconstruction	0.8
Background	2.1
FSI error	1.5
Total	2.9

using the nuSTORM flux are shown in Figure 3.5, for the CCQE channels. The figure shows the precision with which the cross section would be measured if the systematic uncertainties estimated for the HiResMν detector are combined with the 1% flux uncertainty that nuSTORM will provide. For comparison, the performance of HiResMν combined with a flux uncertainty of 10% is also shown. Existing data is superimposed for comparison. The figure shows that nuSTORM has the potential to improve the systematic uncertainty on ν_μ and $\bar{\nu}_\mu$ CCQE cross section measurements by a factor of $\sim 5-6$ while the $\nu_e N$ ($\bar{\nu}_e N$) cross section measurements would be unique. With such small uncertainties associated with the beam, it is important to keep detector systematics low as these are likely to set the limit on the precision of cross sections measurements at nuSTORM.

Figure 3.5 is no more than an illustration of points made in the text. The relevant work that needs to be done is the study of how cross section uncertainties propagate to the sensitivity of a δ_{CP} or a mass hierarchy measurement. Some authors have already engaged in this important task [44], but this is still a field which needs to be extended and that collaborations suggesting experiments for the future must take into account so that their assumptions are more realistic.

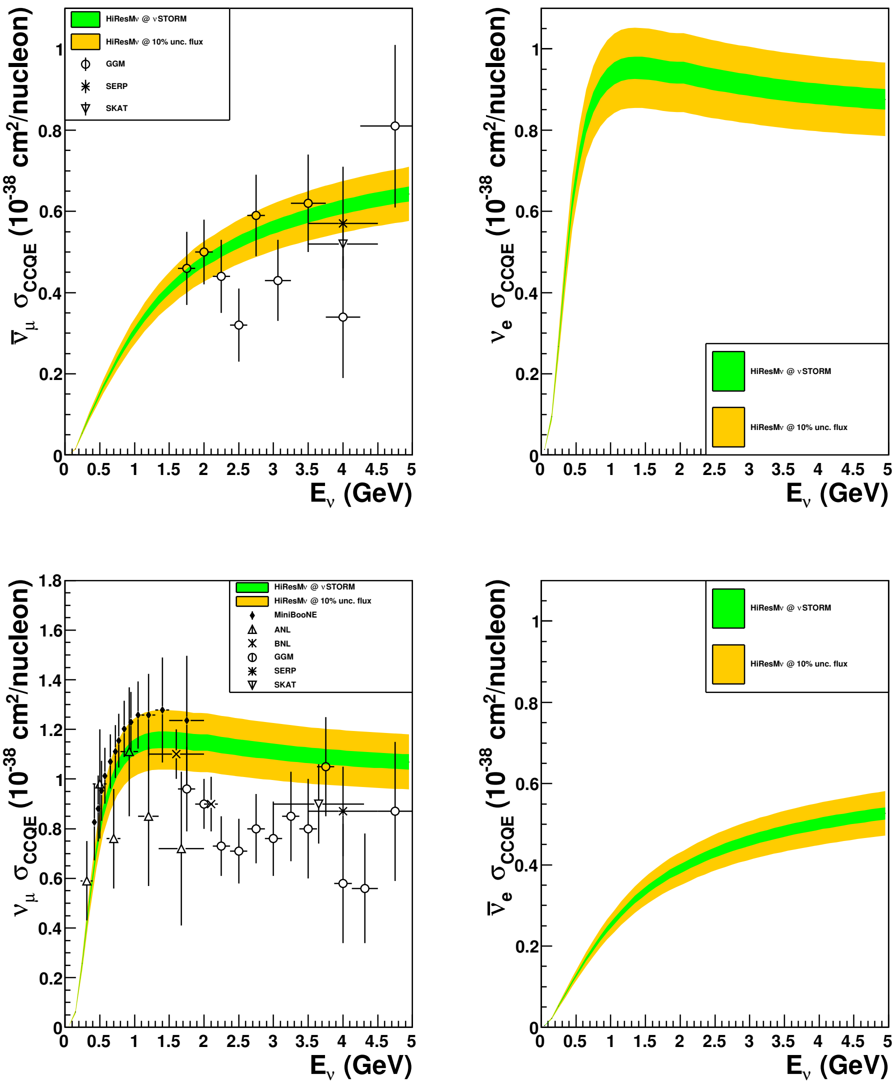

Figure 3.5: The CCQE cross section (σ_{CCQE}) plotted as a function of incident neutrino energy (E_ν). The cross sections that would be obtained with stored μ^+ beams are shown in the top row: $\bar{\nu}_\mu$ and ν_e. The cross sections that would be obtained with stored μ^- beams are shown in the bottom row: ν_μ and $\bar{\nu}_e$. The width of the coloured bands represent the systematic uncertainty on the cross sections determined using the HiResMν detector at the nuSTORM facility (see text for details). The green band shows the detector uncertainties combined with the 1% uncertainty on the neutrino flux at nuSTORM. The yellow band shows the detector uncertainties combined with a flux uncertainty of 10%. Measurements made by the MiniBoNE (⧫), ANL ($\triangle$), BNL ($\times$), Gargamelle ($\bigcirc$), SERP ($*$) and SKAT ($\bigtriangledown$) collaborations are also shown [98, 103–109]. The data can be found at [110].

3.7 Summary

An overview of the different neutrino interaction modes was made, with special attention given to the coherent production of pions. Final state interactions, which follow the neutrino scattering and change both the particles that come out of the interaction vertex and their energy spectrum where also discussed. This and other difficulties associated with the extraction of neutrino cross section measurements were explored. From the conclusion that the beam systematic uncertainties dominate and limit the precision with which cross sections can be measured, the potential for such measurements using the nuSTORM beam was discussed. In summary, the unprecedented neutrino energy uncertainty, the precise knowledge of flavour content of the beam and the richness in electron neutrinos would lead to unique and precise cross section measurements.

Table 3.4: Existing cross section measurements of coherent π^0 production in neutrino-nucleus interactions. The experiments at the CERN-PS provided the first experimental evidence of coherent π production. MiniBooNE and SciBooNE, both at Fermilab's Booster Neutrino Beam (BNB), performed the only measurements of coherent π production (CC or NC) below the neutrino energy of 2 GeV.

Experiment	Target ($\langle A \rangle$)	Neutrino Beam	$\langle E_\nu \rangle$	Neutrino	σ (10^{-40} cm^2/nucl.)	Reference
Aachen-Padova	Aluminium (27)	CERN-PS	2	ν_μ	27 ± 7	[79]
Aachen-Padova	Aluminium (27)	CERN-PS	2	$\bar{\nu}_\mu$	27 ± 7	[79]
Gargamelle	Freon (30)	CERN-PS	3.5	ν_μ	31 ± 20	[80]
Gargamelle	Freon (30)	CERN-PS	3.5	$\bar{\nu}_\mu$	45 ± 24	[80]
CHARM	Marble (20)	CERN-SPS	31	ν_μ	96 ± 42	[111]
CHARM	Marble (20)	CERN-SPS	24	$\bar{\nu}_\mu$	79 ± 26	[111]
SKAT	Freon (30)	Serpukhov	7	ν_μ	52 ± 19	[83]
MiniBooNE	CH_2 (12)	BNB	0.7	ν_μ	7.7 ± 3.9	[112]
NOMAD	Carbon (12.8)	CERN-SPS	24.8	ν_μ	72.6 ± 10.6	[113]
SciBooNE	Carbon (12)	BNB	0.8	ν_μ	3 ± 1	[114]

Table 3.5: Cross section measurements of CC coherent π production. Experiments observing neutrinos at energies below 7 GeV reported null results.

Experiment	Target ($\langle A \rangle$)	Neutrino Beam	$\langle E_\nu \rangle$	Neutrino	σ (10^{-40} cm^2/nucl.)	Reference
SKAT	Freon (30)	Serpukhov	7	ν_μ	106 ± 16	[83]
SKAT	Freon (30)	Serpukhov	7	$\bar{\nu}_\mu$	113 ± 35	[83]
BEBC	Neon (20)	CERN-SPS	30.4	$\bar{\nu}_\mu$	175 ± 25	[84]
BEBC	Neon (20)	CERN-SPS	31.7	ν_μ	250 ± 49	[115]
FNAL E632	Neon (20)	Main Ring	91.1	ν_μ	350 ± 80	[116]
FNAL E632	Neon (20)	Main Ring	74.5	$\bar{\nu}_\mu$	270 ± 110	[116]
CHARM II	Glass (20.7)	CERN-SPS	23.7	ν_μ	168 ± 41	[117]
CHARM II	Glass (20.7)	CERN-SPS	19.1	$\bar{\nu}_\mu$	161 ± 40	[117]
K2K	Carbon(12)	KEK	1.3	ν_μ	$< 0.077(90\%CL)$	[85]
SciBooNE	Carbon(12)	BNB	1.1	ν_μ	$< 0.0844(90\%CL)$	[86]
SciBooNE	Carbon(12)	BNB	2.2	ν_μ	$< 0.287(90\%CL)$	[86]

4 Measurement of CC Coherent Pion Production at ArgoNeuT

Compared to the old bubble chamber experiments, most modern neutrino detectors seem to render more *inclusive* measurements, in the sense that some scattering products may be left unmeasured. That's due to the choice of dense interaction medium combined with limited pixel size which leads to a loss of sensitivity to the particle products created in the neutrino interaction: they must be energetic enough to travel through the dense medium and leave a trace in enough detector pixels to be reconstructed. Liquid argon detectors are perhaps the exception. Liquid argon detectors are capable of three-dimensional imaging of neutrino events with a quality that surpasses the old bubble chamber while delivering, at the same time, precise calorimetry. In this Chapter such capabilities are explored in order to measure a neutrino interaction with very low cross section, CC coherent π production. In the few GeV neutrino energy range in which the measurements are reported, this interaction is estimated to amount to only a few percent of the total neutrino-nucleus cross section. The experiment takes place at Fermilab's Neutrinos from the Main Injector (NuMI) beam [118, 119] and the detector used is ArgoNeuT [120].

4.1 The NuMI Beam

The Neutrinos at the Main Injector (NuMI) facility at Fermilab was designed to produce an intense neutrino beam that would allow the study of neutrino interactions and oscillations. The planned physics program included measurement of oscillation parameters (Main Injector Neutrino Oscillation Search (MINOS) [121]), cross sections measurements (MINERVA [122]), measurement of the mass hierarchy and a search for CP invariance violation in the neutrino sector (NOνA [36]).

The production of the NuMI beam fits the conventional-facility scheme discussed in Chapter 2. Spills of 120 GeV protons from Fermilab's Main Injector are extracted every 1.9 s. These are 10 μs long and bent downwards through an angle of 3.3° so that the resulting neutrino beam is directed at the MINOS far detector in Soudan, Minnesota (see Figure 4.1). The protons are focused onto a 94 cm long graphite target where $\sim 85\%$ of the protons interact. At the target, the proton beam has an RMS width of about 1 mm. The mesons produced by the interaction with the target are captured by two magnetic horns, 3.3 m and 3.8 m long, placed 10 m from each other. The current supplied to the horns defines the toroidal magnetic field within their volume which is used to select the charge and the momentum of the mesons that are kept in the beam. The decay of the pions into muons and neutrinos happens in the 675 m long decay tunnel. Protons and undecayed mesons are removed by a beam absorber placed at the downstream end of the decay pipe. This consists of a water-cooled aluminium core surrounded by layers of steel and concrete blocks. The muons in the beam are stopped by 240 m of Dolomite rock, before the MINOS near detector hall is reached. The resulting neutrino beam has an average energy of $3 - 16$ GeV.

The data used in this work was collected in an antineutrino-enhanced mode which provides a flux that is mostly muon antineutrino but still rich in muon neutrinos (see Figure 4.2). The total Protons On Target (POT) accumulated during a 6-month run was 1.2×10^{20}. The estimated integrated fluxes are 6.56×10^{11} muon neutrinos per cm^2 and 2.94×10^{12} muon antineutrinos per cm^2.

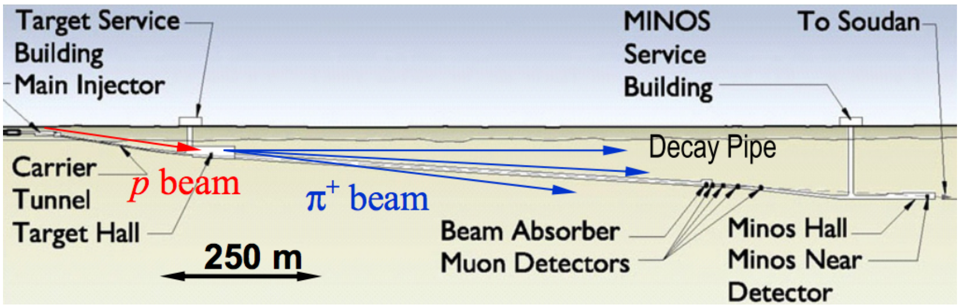

Figure 4.1: Schematic view of the NuMI beam line. From left to right, the figure depicts the main stages in the production of the neutrino beam. Protons from the Main Injector are bent downwards, directed to the MINOS Far Detector in Soudan. The protons reach the target hall shortly after being extracted; the mesons that are then produced travel along the decay pipe. After meeting several beam absorbers and rock, a neutrino beam reaches the Minos Hall where the MINOS Near Detector and ArgoNeuT are placed. *Figure source:* [119]

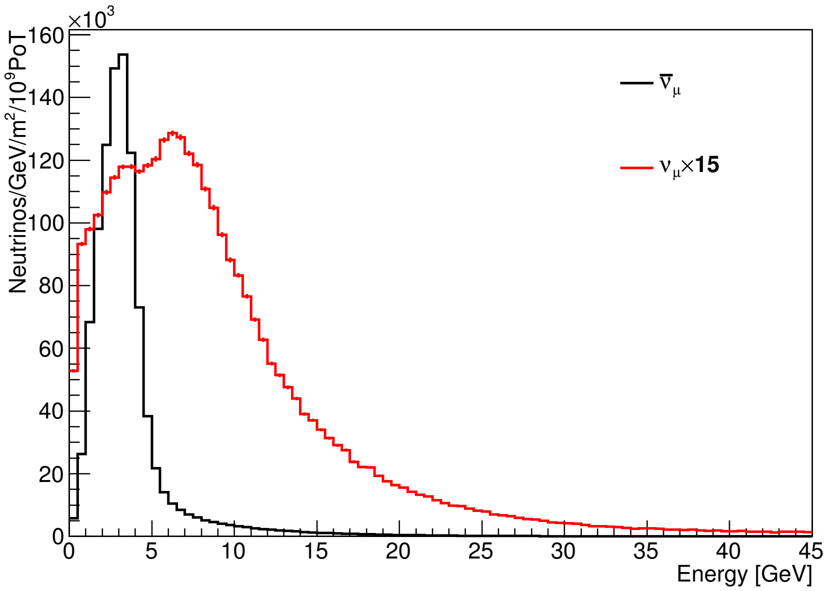

Figure 4.2: Estimated flux for the antineutrino-enhanced run. The neutrinos that contaminate the antineutrino beam originate from forward going mesons which are not defocused by the magnetic horns. The flux estimation shown is the result of a FLUKA simulation tuned with data from NA49 [123] and the MINOS Near Detector.

4.2 The ArgoNeuT Detector

The liquid argon time projection chamber (Liquid Argon Time Projection Chamber (LArTPC)) [124] is a technique that has met great interest in the experimental neutrino physics community. This class of detector has shown the capability to provide mm-scale resolution and precise calorimetry. The prospective use of this class of detectors in future experiments measuring oscillations motivated the construction of a test-stand at Fermilab: the Argon Neutrino Test (ArgoNeuT) [120]. This prototype detector is the first Time Projection Chamber (TPC) in a low energy ($1 - 10\,\mathrm{GeV}$) neutrino beam; the NuMI beam introduced in the previous section.

ArgoNeuT's liquid argon is contained by a stainless steel vessel (see Figure 4.3). Inside, sits a TPC with dimensions $40 \times 47 \times 90\,\mathrm{cm}^3$. The longest direction is oriented parallel to the beam and the drift direction ($47\,\mathrm{cm}$) is the horizontal perpendicular to it. On one side there is a solid copper sheet which is the cathode plane held at $-25\,\mathrm{kV}$. On the opposite side there are three wire planes. The wire pitch in each is $4\,\mathrm{mm}$ and the planes are also separated by $4\,\mathrm{mm}$ one after the other. The first plane has 255 wires oriented vertically and it is not instrumented for readout. This is the *shield plane*, used to shape the electric field and protect the outer planes from drifting ionization. The second plane is the *induction plane*, consisting of 240 wires rotated $60°$ with respect to the beam direction. The third and last plane is the *collection plane*, also consisting of 240 wires but rotated by $-60°$. The drift volume between the cathode and the wire planes is enclosed by 23 copper strips (again, see Figure 4.3). These strips are $1\,\mathrm{cm}$ wide and spaced by $1\,\mathrm{cm}$. They are wired to the cathode along a resistor chain assuring the field throughout the TPC is uniform. The technical specifications of the detector relevant for this work are summarised in Table 4.1.

Table 4.1: Specifications of the ArgoNeuT detector.

Cryostat Volume	500 L
TPC Volume	170 L
Numb. Electronic Channels	480 (240 per plane)
Numb. Planes	2
Wire Pitch	4 mm
Max. Drift Length	47 cm
Field	500 V/cm

ArgoNeuT is placed in the MINOS hall, 1.5 m upstream from the front facade of the MINOS near detector – see Figure 4.4. The MINOS Near Detector, hereafter referred to simply as MINOS, is a 980 ton magnetised detector. It is made of 282 alternating steel-scintillator planes. The scintillator planes are 1 cm thick and the steel planes are 2.45 cm thick. Each plate has an octagonal shape, 3.8 m diameter. The total detector length is 16.8 m. Muons, which escape the ArgoNeuT volume, can be linked to MINOS. The MINOS collaboration has provided the data and the software tools to run their detector reconstruction and simulation. The combination of the reconstruction of both detectors results in great analysis potential, as ArgoNeuT is an excellent probe of the vertex of the interactions and delivers precise calorimetry of the products emerging while MINOS is capable of identifying the charge and momentum of the muons.

The ArgoNeuT collaboration uses the Liquid Argon Software (LArSoft) software framework [126]. This is a C++ framework used by all Fermilab-based collaborations running liquid argon TPC's, such as MicroBooNE or LBNE. With this package, both MC simulation and data reconstruction are possible. The Monte Carlo simulation uses Generates Events for Neutrino Interaction Experiments (genie)-v.2.8.0 [127] as the neutrino generator and geant4 [128] for the propagation of particle products in the detector. An overview of the reconstruction stages is given in the following paragraphs.

4.2.1 ArgoNeuT Reconstruction

The propagation of charged particles in ArgoNeuT's liquid argon volume induces the creation of electron-ion pairs that are free to drift in the noble liquid medium. The electric field accelerates the electrons towards the anode wires where they induce pulses to be analysed. At the induction plane, the electrons induce a current; at the collection plane they are captured. The Analogue to Digital Converter (ADC) value readout is related to the number of electrons collected by an electronic calibration factor. However, the estimation of the number of electrons extracted will require a few corrections which take into account the loss of electrons due to recombination with ions at the interaction point and with impurities while drifting in the liquid.

In order to collect efficiently the ionisation electrons, the liquid argon must be kept free from electro-negative impurities, such as Oxygen or Nitrogen, which can lead to recombination. The impurity level must be no greater than a few parts per trillion. This is achieved by constantly pumping the liquid argon through a purification system. The free electron lifetime, τ, is the mean time an electron remains free before it is captured. It can be measured using tracks reconstructed in the detector. For a drift time t, the corrected charge (Q_{cor}) can be calculated from the measured (Q_{meas}) using the electron lifetime:

$$Q_{cor} = Q_{meas} \exp(t/\tau). \tag{4.1}$$

Dividing Q_{cor} by the wire pitch renders the number of electrons extracted per cm, which is then related to the density of energy deposition, dE/dx, using Birk's law [129]:

$$\frac{dQ_{cor}}{dx} = A \frac{dE/dx}{1 + K_B(dE/dx)}, \tag{4.2}$$

where A and K_B are measured parameters, constant for a given electric field in a given medium. In this work, A (0.8) and K_B ($0.097 g.MeV.cm^2$) are extracted from [130]. Birk's law introduces a correction for the charge that is collected: it is possible to have the electrons recombine with the ions created at the interaction point. This effect depends on the density of the energy deposition and the electric field which drifts the electrons away.

Liquid argon generates about 28 thousand electrons per MeV of energy deposited, which is well above the typical noise signal generated in the wires (below one thousand electrons). When combined with the estimation of the residual distance from a track point to the end of the track, the energy loss can provide conclusive information of the particle type. As shown in Figure 4.5, protons are much more ionising than other particle types, while pions and muons are hard to discriminate based on calorimetry alone. The templates shown in Figure 4.5 are used in ArgoNeuT's calorimetric Particle IDentification (Particle Identification (PID)) algorithm. For every fully contained track, the residual distance to the end of the track can be calculated and data points compared to each template. The best agreement determines the PID of the track.

Using the wire pitch (0.4 cm) and the bottom plot of Figure 4.5, one can estimate the energy threshold for detection of different particles. For protons, the limit is at $\sim 22\,\mathrm{MeV}$ and for muons and pions it is at $\sim 10\,\mathrm{MeV}$. The considerations made so far refer to the calorimetric reconstruction of the detector. The topological reconstruction, that is the identification of particle trajectories, is performed in a set of stages. In LArSoft, each stage is a block for which several algorithms are available and can be interchanged. The reconstruction elements described here are the ones used in this analysis, and they are optimised for ArgoNeuT [131].

Hit Finding

The "hit finding" is a process applied to the smoothed and Fast Fourier Transformed signals. It starts with a search for local maxima in the readout of a single wire *ADC* values over time. For each local maxima, the two local minima around it are found and they determine the full width of the signal pulse. In the case where the maximum is below the threshold, the hit is rejected. In order to identify events in which multiple hits overlap, the hit finding algorithm attempts a fit of N Gaussians to the pulse shape, where each Gaussian has a characteristic, detector specific, pulse width. At the end of this stage, all hits found in the detector are characterised by a signal amplitude, the integrated ADC count above and below the signal baseline, the start and end times and the central time, and a flag indicating if the hit is close in time to another hit.

Clustering

The next step consists in grouping hits in clusters, based on their proximity in wire and time. This process is applied in each plane independently. The clustering method is inspired by the "Density-Based Spatial Clustering of Applications with Noise (DBSCAN) [132]. In this approach, hits are characterised as belonging to a cluster or being isolated based on the surrounding density of hits. Isolated hits are considered noise while hits clustered in ellipses in a (wire, time) coordinate system are carried on to the next reconstruction stage.

Line finding and line merging

The search for line-like objects starts with a Hough Transform. All the hits surviving the DBSCAN are used in this algorithm. The $(wire, time)$ coordinates are transformed into (r, θ) lines and accumulated on a two dimensional histogram, the Hough Accumulator. The cell in the Hough Accumulator with the highest weight contains the parameters for a candidate-line. The hits belonging to a line that has been found can be removed and the process repeated until all lines are found - in practice, until the maximum weight found in the Hough Accumulator is below the minimum acceptable value. It is observed that sometimes a single line object is broken into multiple segments. In order to fix this feature, a simple "line merger" step is added. The end product are line objects which contain the slope, end-points and all the hits associated with the line.

Three dimensional tracking

The algorithms explained so far operate in both detector views separately. The merging of these reconstructed objects into a three dimensional image is done by comparing the time the objects are registered in both planes. Signals induced in the collection and induction plane by the same particle trajectory are readout at nearly the same time, the difference being the time the drifting charge takes to propagate between the two wire planes.

A fundamental tool for the reconstruction and analysis of the ArgoNeuT data is the LArSoft event display. The event display can be used to hand-scan the neutrino interactions. This is very useful for the development of the reconstruction algorithms and for the production of physics analyses.

Even in the case of automated analysis like that which the ArgoNeuT collaboration has pioneered, hand-scanning provides a compelling verification. An example of a full event display is shown in Figure 4.6.

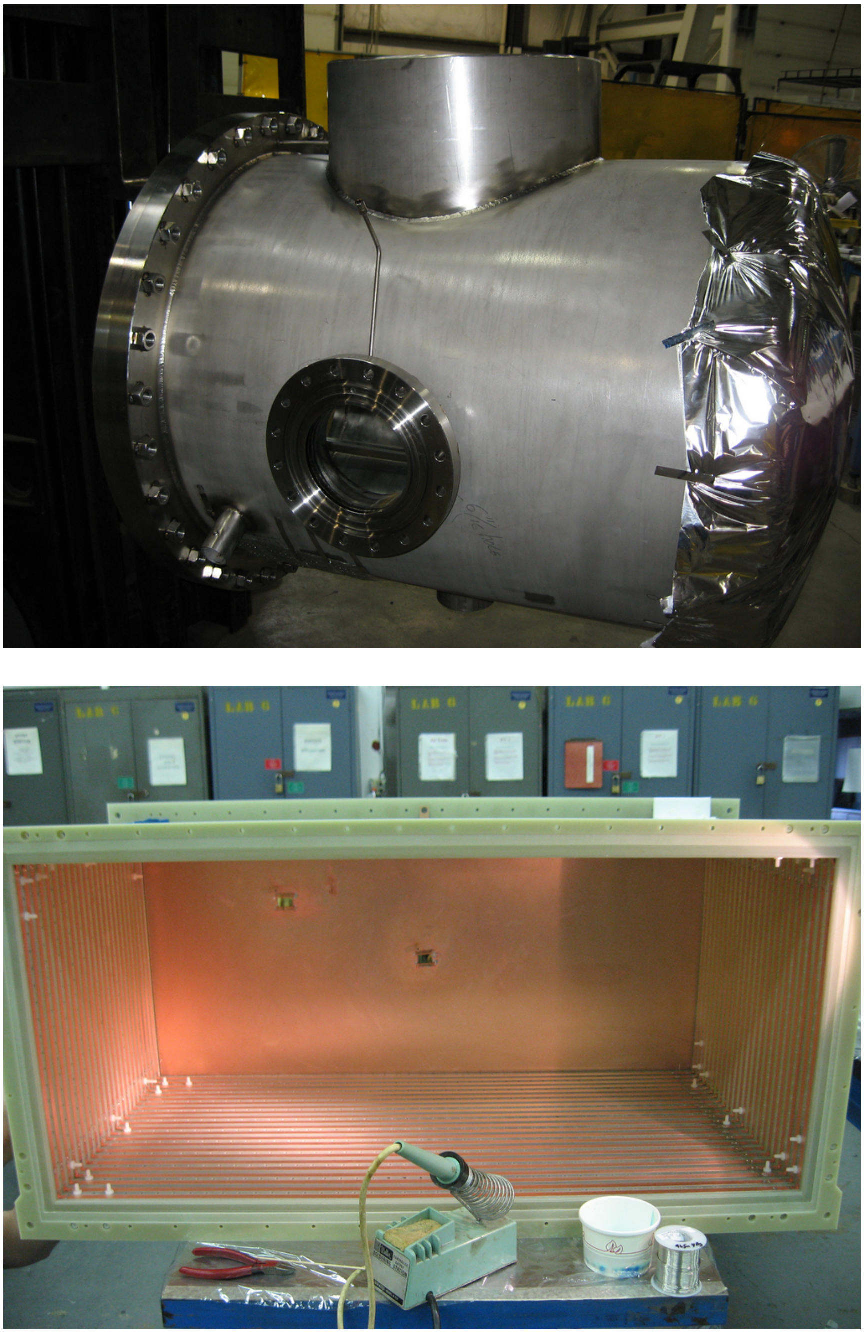

Figure 4.3: On the top, the vessel where the TPC and the liquid argon are contained. On the bottom, ArgoNeuT's TPC. The solid copper plane is visible in the foreground. The 1 cm copper strips placed along the drift direction and enclosing the entire drift volume are also visible. Image Credit: ArgoNeuT Collaboration [125].

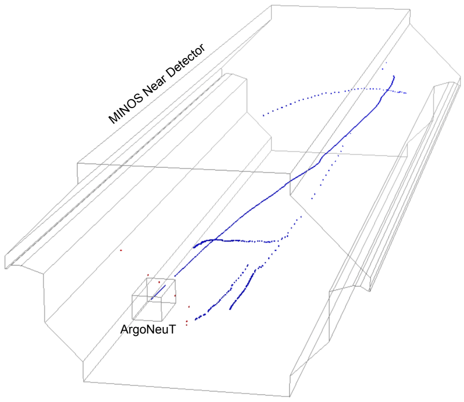

Figure 4.4: Event display of a data event where a muon is produced in ArgoNeuT and linked to the MINOS near detector.

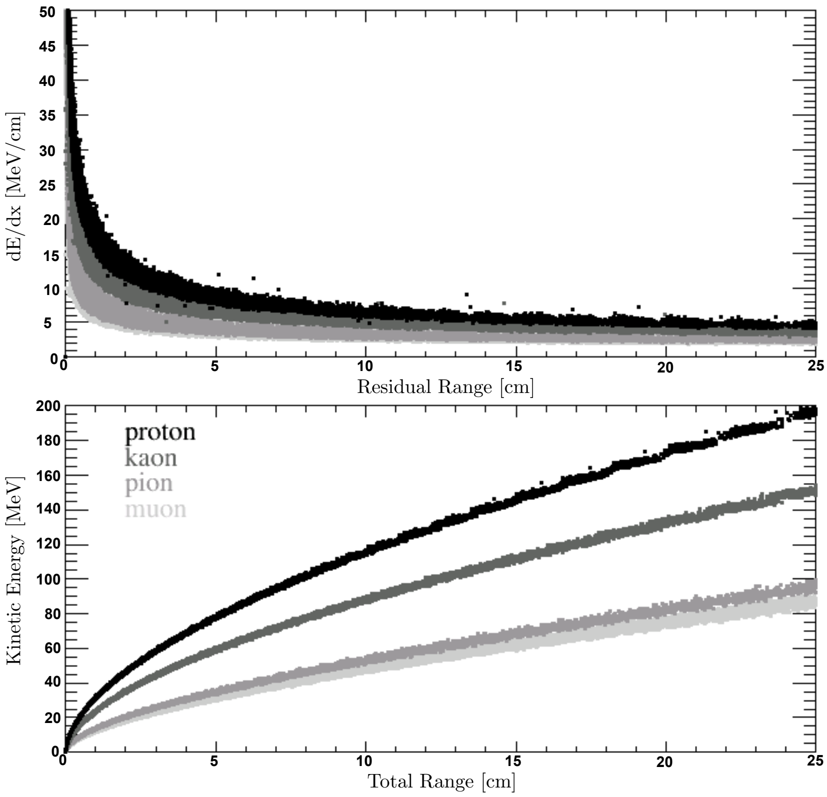

Figure 4.5: Templates of dE/dx vs residual range and kinetic energy vs total range for different particle species. The differences are the basis of ArgoNeuT's PID capability.

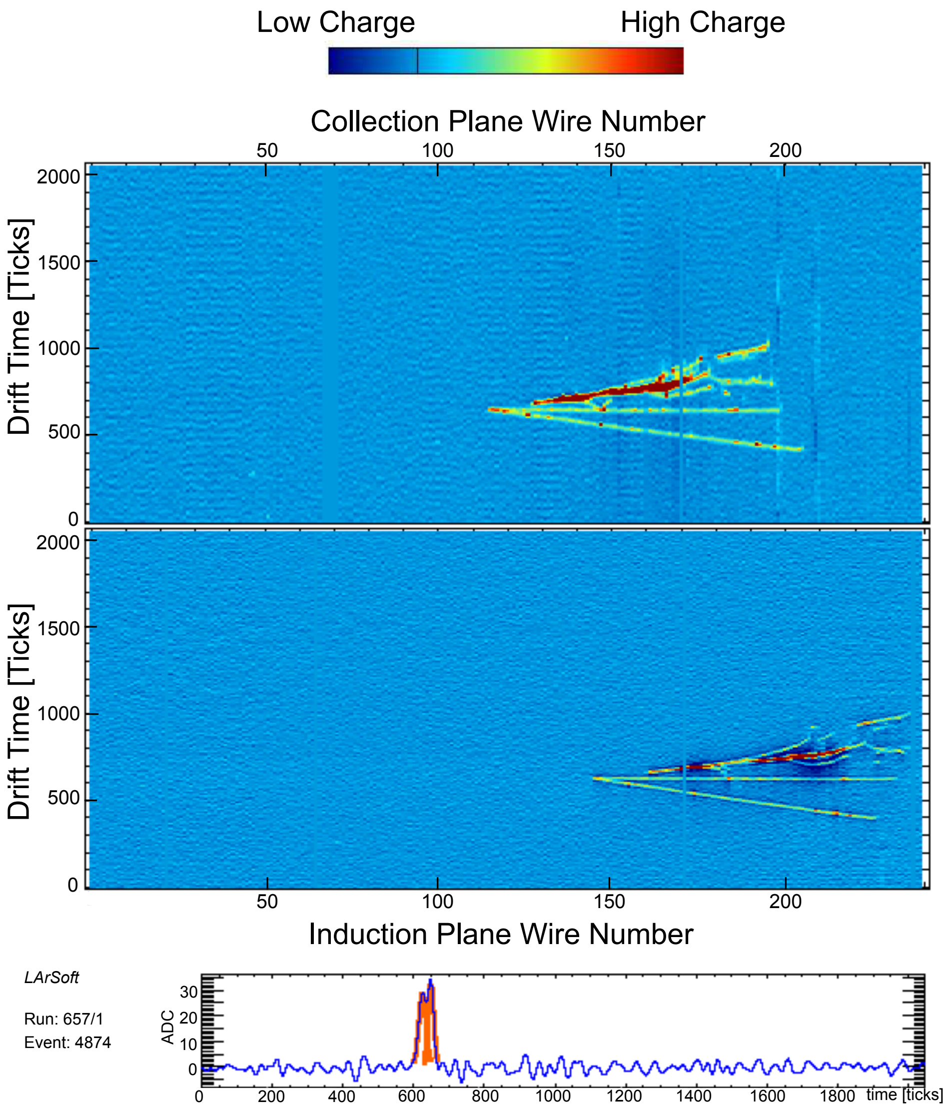

Figure 4.6: Example of a data event display. The collection plane is shown on the top, followed by the induction plane view. The colour scheme indicates the level of energy deposition at each hit. A time series of the charge readout along a wire is also shown at the bottom, for wire 125 of the collection plane. The double peak corresponding to the two tracks shown in the plane views is distinguishable. The electromagnetic shower emerges a few wires after. The separation between the shower and the event vertex is a π^0 signature.

4.3 Overview of the Analysis

The analysis presented in the following sections follows a set of stages quite conventional. In the first stage, *event selection*, a set of reconstruction cuts are introduced in order to select a sample of events with the topology of interest. The next stage is *event classification*, where the events previously selected are classified into signal or background. The number of signal events, N, is then estimated (*signal extraction*) and flux-averaged cross section is calculated:

$$\langle\sigma\rangle = \frac{N}{\epsilon N_{Ar} \int \phi \, dE}; \tag{4.3}$$

where N_{Ar} represents the number of argon target nuclei in the detector, ϵ is the efficiency of the event selection and $\int \phi \, dE$ is the integrated neutrino/antineutrino flux per cm^2.

4.4 Event Selection

The final state topology of the signal events consists of two charged tracks:

$$\bar{\nu}_\mu + \mathrm{Ar} \rightarrow \mu^+ + \pi^- + \mathrm{Ar}, \tag{4.4}$$

$$\nu_\mu + \mathrm{Ar} \rightarrow \mu^- + \pi^+ + \mathrm{Ar}; \tag{4.5}$$

where the argon nuclei recoils slowly and is undetected. In order to select these $\mu + \pi$ events, a set of cuts is defined. The starting requirements are the existence of two reconstructed tracks inside the TPC, one of them being matched to a MINOS track. The matching criteria is a requirement on the collinearity of the ArgoNeuT and MINOS tracks: the extrapolation from ArgoNeuT to MINOS must fall within 12 cm of the start of the MINOS track and the difference between track angle must be less than 0.17 rad. The matched track corresponds to the muon and the unmatched track is the pion candidate. The pion may or may not be contained inside the TPC volume and it does not need to be matched to MINOS. From here, further cuts on the *topology* of the event, on the *vertex activity* and on the *calorimetric* information are applied. Combined, the cuts aim at verifying that the unmatched track corresponds to a pion and that there are no other particles emerging from the vertex of the interaction. In the following paragraphs, some parameter distributions are studied and cuts are applied to them. The optimal cut values are found independently for the neutrino and antineutrino samples. The Monte Carlo simulation is used to try all possible combinations of cut values and find the one that maximises the significance of the selection here defined to be $\sigma_1 = s/\sqrt{s+b}$, where s and b are the number of signal and background events that pass the cuts. This definition of significance includes more signal than the sometimes preferred $\sigma_2 = s/\sqrt{b}$.

4.4.1 Drift-Time Cut

The drift-time cut is used to exclude events in which the two tracks show a vertical separation that suggests the tracks are not produced at the same vertex – see Figure 4.7. The signal events of this analysis can show some degree of overlap between the pion and muon tracks. As a consequence, it is possible that the overlap region is reconstructed as belonging to only one of the tracks and a second track is found a few wires downstream of the interaction point, once the particles have separated sufficiently. However, the vertical displacement of the new track with respect to the first should be small, unlike what is shown in Figure 4.7. In the event displays shown, photon production induces activity which is tagged as a track, with the vertex at the photon conversion point. The vertical distance between this point and the muon track corresponds to a time difference (Δt) measured in time ticks (each time tick corresponds to 198 ns). In order to remove this type of background event, the distributions of Δt on the collection plane for signal and background events were studied and selection cuts were defined (Figure 4.8). The cut values chosen, in units of time ticks, are 35 and 30 for antineutrino and neutrino, respectively.

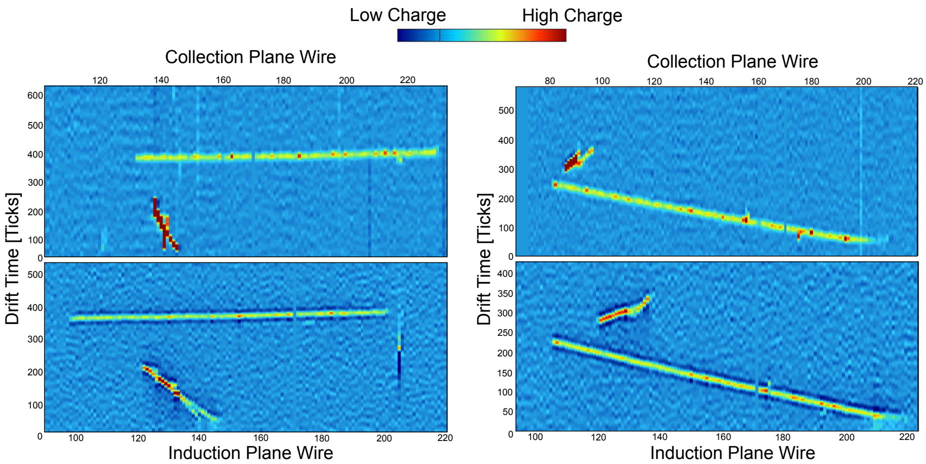

Figure 4.7: Data events with two-track topology where the unmatched track is induced by photon conversion. The vertical separation (Δt) is incompatible with the expected signal topology. Events like the ones shown might be related to the excess of electron-like events in MiniBooNE [133].

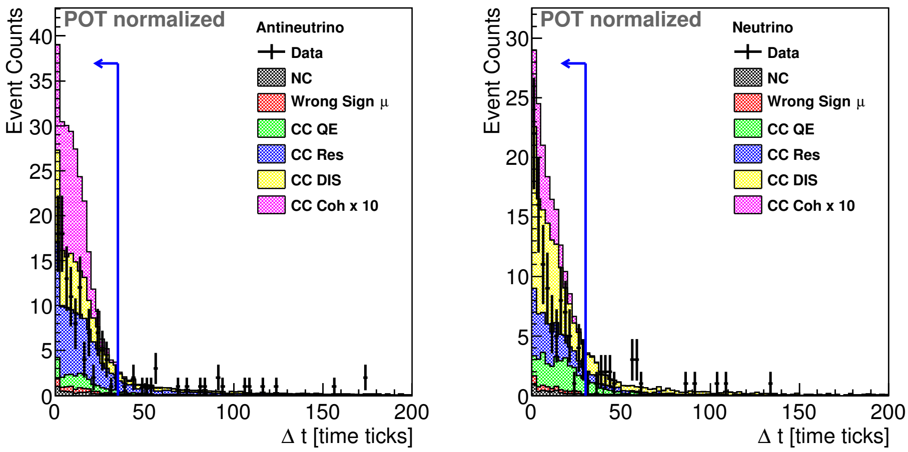

Figure 4.8: Δt values as reconstructed for signal and background events. The cut values are represented by the blue lines. For the anti-neutrino events, the cut is set to 35 time ticks; neutrino events, it is set at 30 time ticks.

4.4.2 Vertex Activity Cut

ArgoNeuT has great capability for discriminating any activity that comes out of the interaction vertex. Photons and even neutrons leave scattered hits which are detected, even if not usable for tracking. This potential is exploited by defining a box around the event vertex in the collection plane and analysing the charge deposition within. The Fractional Charge is defined as

$$\text{Frac. Charge} = \frac{\text{total charge inside box associated to the 2 tracks}}{\text{total charge collected inside box}}, \quad (4.6)$$

where the box is centred at the interaction vertex and is 80 wires long, 600 time ticks tall - shown in red in Figure 4.9 The dimensions chosen correspond to approximately 20 cm × 20 cm. The cuts defined (86% and 84%) are a lower bound on the acceptable fraction of charge that belongs to the two reconstructed tracks (Figure 4.10).

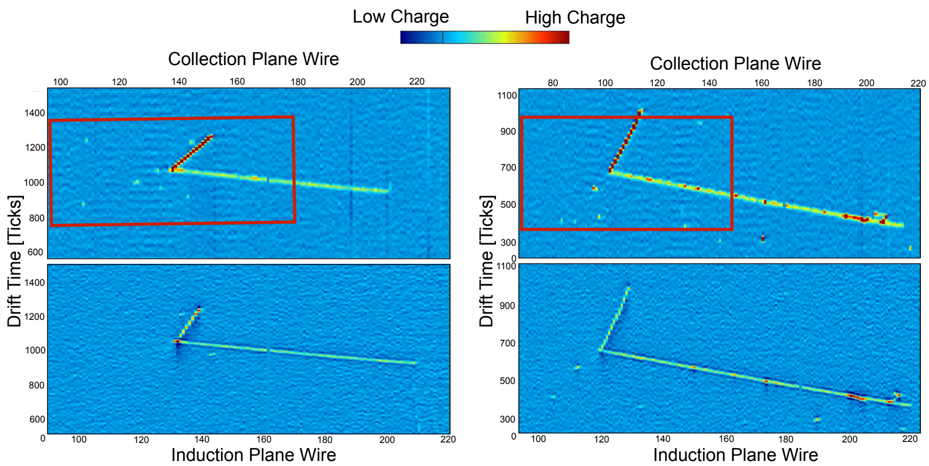

Figure 4.9: Two data events where the two track topology is found but where there is also activity around the vertex compatible with gamma de-excitation on the nucleus. These events are excluded by the vertex activity cut. The box, in the collection plane, inside which the charge deposition is studied is also shown. The scattered hits in these figures correspond to energy depositions of a few MeV per hit.

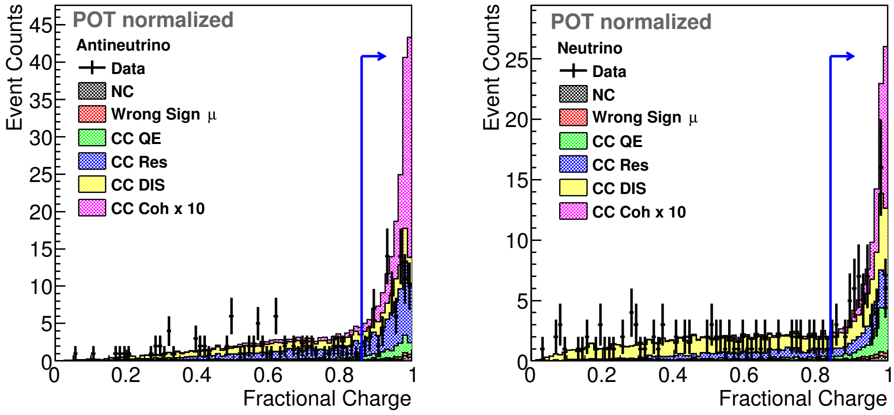

Figure 4.10: The fraction of charge inside a $\sim 20\,\text{cm} \times 20\,\text{cm}$ box in the collection plane must be mostly assigned to the two tracks. Cut values on this fraction are shown in blue: 0.86 for antineutrino and 0.84 for neutrino events.

4.4.3 Calorimetry Cuts

The calorimetry cuts are used to exclude proton activity in three ways. The first and most straightforward comes into play when the unmatched track is contained. In this case, the calorimetric-based PID is used to identify the particle that produced the track by using the measured residual range and stopping power along the track (revisit Figure 4.5). Tracks tagged as protons are promptly rejected. The second case is when the unmatched track is not contained. The calorimetric PID reconstruction is not possible in this case because the residual range cannot be estimated. However, the stopping power along this track can still be used to assert that it is consistent with that of a pion. The charge readout from pions and muons corresponds to minimum ionising particles (MIP) while protons are much more ionising, at least $2-3$ MIP equivalent. This is used to define a cut on the average stopping power of the pion candidate, $\langle dE/dx \rangle_{\pi}$ (Figure 4.11, top row). The third and last consideration is more subtle. Low energy protons frequently emerge from the interaction vertex leaving no more than one or two wire hits. These are hits with high ADC readout that often end up being associated with longer tracks produced by other particles, in this analysis, the muon or the pion track. In order to exclude events with these protons, a cut is set on the ADC readout of the first and second wire hits (Figure 4.11, bottom rows). The second wire hit is added because the first wire hit is affected by incomplete charge readout. Therefore, protons that do not lead to substantial charge deposition on the first wire may still be tagged using the second wire.

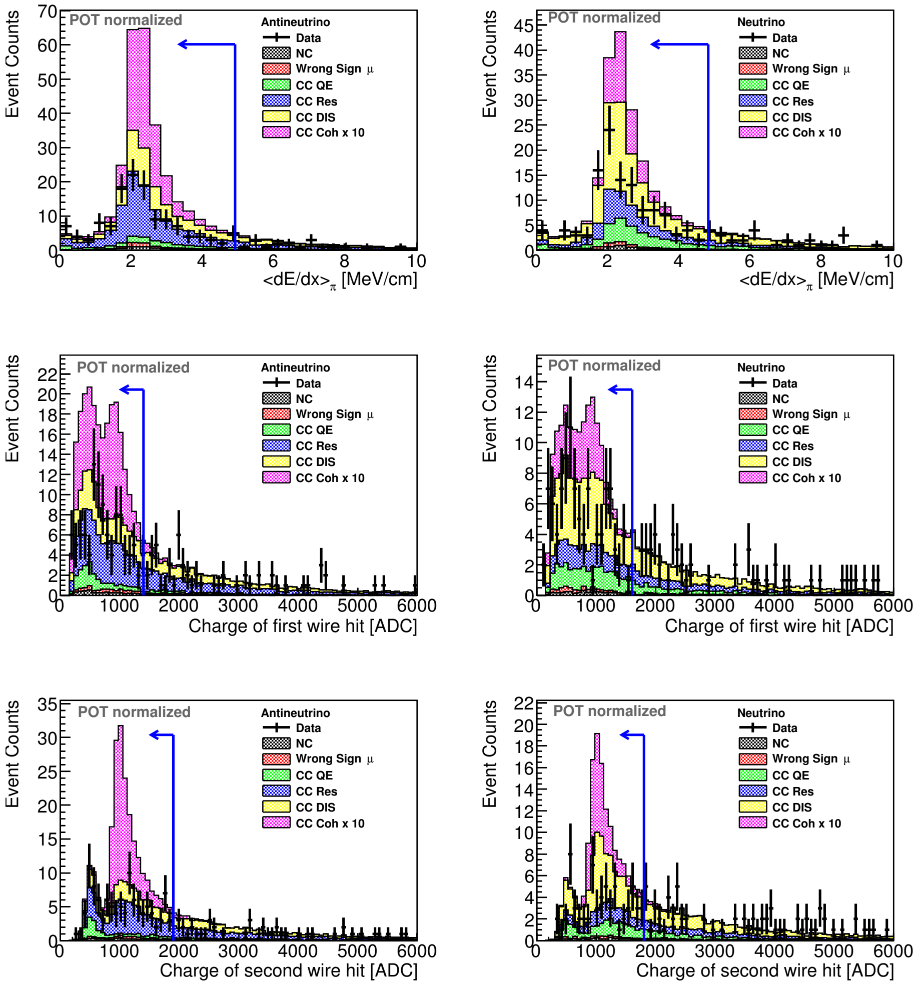

Figure 4.11: The calorimetry cuts (blue lines) applied on the mean dE/dx of the pion candidate track and on the ADC values of the first and second wire hits. The cut on the mean stopping power is used to exclude unconfined proton tracks; the cuts on the ADC readout are used to exclude events where low energy protons are created.

4.4.4 Summary of the Event Selection

Overall, the cuts presented in the previous paragraphs define an exclusive selection. As a consequence, the efficiency is rather low: 21.8% for anti-neutrino and 18.4% for neutrino events. This efficiency is defined as the ratio

$$\epsilon = \frac{\text{number of signal events selected}}{\text{number of signal events generated inside the TPC}} \tag{4.7}$$

The efficiency is limited by the 2-track reconstruction efficiency. The cut values and some figures of merit of the selection are listed in Table 4.2.

Table 4.2: Summary table of the event selection: cuts applied, resulting significance ($s/\sqrt{s+b}$) and efficiency of the cuts. Number of data events passing these cuts are also shown. The efficiency loss is dominated by the 2-track finding efficiency. Tables 4.3 and 4.4 add more information.

	$\bar{\nu}_\mu$	ν_μ
Number of tracks	2	2
Drift-time cut	35 ticks	30 ticks
Charge cut	0.86	0.84
$\langle dE/dx \rangle_\pi$ cut	4.9 MeV/cm	4.8 MeV/cm
1st hit ADC cut	1400	1600
2nd hit ADC cut	1900	1800
$s/\sqrt{s+b}$	10.1	3.6
ϵ	21.8%	18.4%
Numb. of data events passing cuts	30	24

The uncertainty associated to the efficiency is investigated using a new Monte Carlo dataset of signal events produced by NuWro. The limiting factor afectting the efficiency is the 2-track reconstruction in part due to the overlap of the pion and muon tracks; by using a different generator, the dependance on the original signal assumptions – which come from GENIE – are gauged. Using the relative difference as an estimate of the uncertainty associated to the efficiency values, it is determined that $\epsilon_{\bar{\nu}_\mu} = (21.8 \pm 0.8)\%$ and $\epsilon_{\nu_\mu} = (18.4 \pm 1.8)\%$.

4.5 Event Classification

The event selection is used to define a sample of events which include background, predominantly π production via resonant production and deep-inelastic scattering. Ideally, the reconstruction of the kinematic parameters of the interaction:

$$Q^2 = 2(E_\mu + E_\pi)(E_\mu - P_\mu cos\theta_\mu) - m_\mu^2; \tag{4.8}$$

and

$$|t| = \left|(q - P_\pi)^2\right|; \tag{4.9}$$

would be used to select the CC coherent pion events, characterised by low $|t|$ (revisit Figure 3.4). However, the ArgoNeuT data doesn't allow the full calculation of these variables due to the incomplete tracking of the exiting pions – E_π and P_π in Equations 4.8 and 4.9 are not completely measured. The natural approach is to use the information left in the TPC to attempt a classification using multivariate methods. The classification into signal or background is based on the following input parameters:

- the angle of the pion candidate track, θ_π;
- the angle of the muon track, θ_μ;
- the opening angle between the two tracks, $\Delta\theta$ – see Figure 4.12;
- the muon momentum, P_μ, based on the MINOS reconstruction and corrected for the momentum loss inside ArgoNeuT;
- the kinetic energy of the pion candidate based on the charge collected from the track, K_π;
- the mean stopping power of the first third of the muon track, $\langle dE/dx \rangle_\mu$. This parameter was added to help discriminate events where the start of the muon and pion tracks overlap.

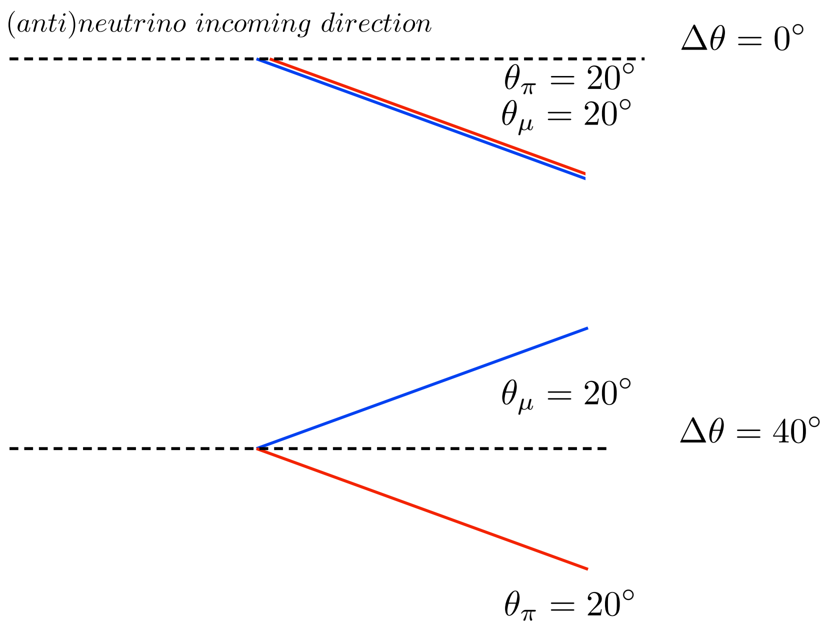

Figure 4.12: Illustration of the usefulness of the $\Delta\theta = \theta_\mu - \theta_\pi$ variable. The track angles are measured as absolute value from the neutrino incoming direction. In order to disambiguate the angle between the pion and muon tracks, the $\Delta\theta$ value is necessary. On the two cases shown, both tracks make 20° angles with the neutrino direction but $\Delta\theta$ can be either 0° or 40°.

Distributions of all the input parameters is shown in Figures 4.13 and 4.14. Some parameters show a clear shape difference between signal and background, making their discrimination power evident. However, parameters that don't exhibit the same shape difference can still provide discrimination power when combined with other variables. The search for this type of correlation is a key to the success of the multivariate analysis. In the end, the event classification exploits all the kinematic features mentioned and delivers a single output parameter, a *classification value*, with more powerful discrimination. This approach is valid if there is good agreement between the Monte Carlo and data distributions for each input parameter. Such comparison is shown in Figures 4.15 and 4.16. Despite the low statistics, there seems to be a reasonable agreement.

The following section explains how the classification algorithms, Boosted Decision Trees, were built.

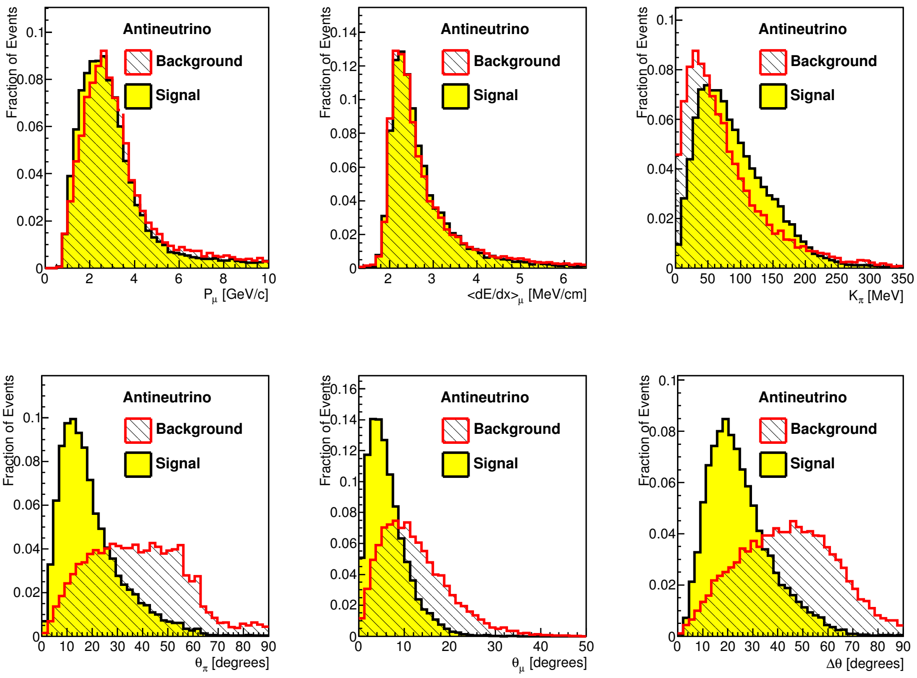

Figure 4.13: Antineutrino mode, input parameters for the multivariate analysis. Signal and background have area normalised. Difference in shape between signal and background is more noticeable for the angular distributions. These differences between signal and background shapes will be used for event discrimination.

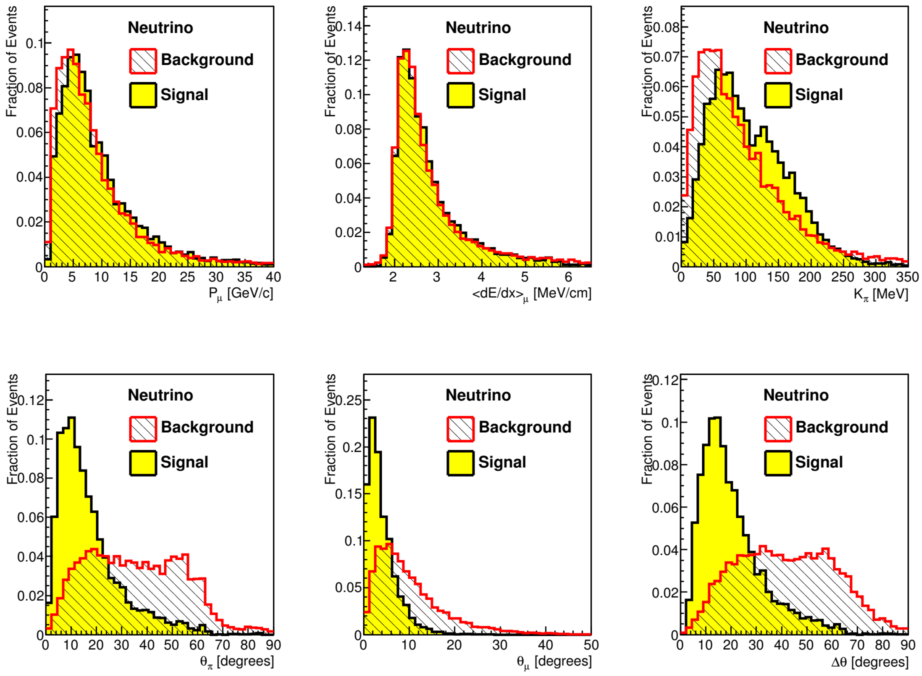

Figure 4.14: Same as 4.13 but for neutrinos.

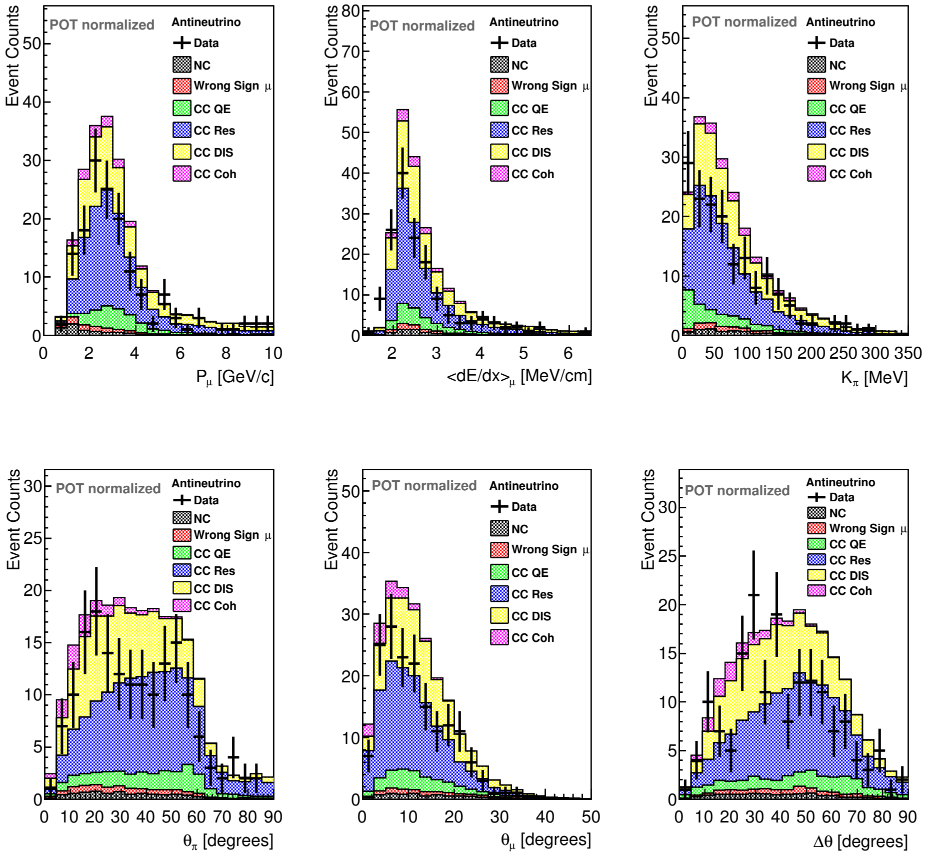

Figure 4.15: Monte Carlo and data distributions of the parameters used in the multivariate analysis. The signal and background expectations are stacked. The Monte Carlo is scaled to data POT. Overall, there is good agreement between the data and the Monte Carlo expectation.

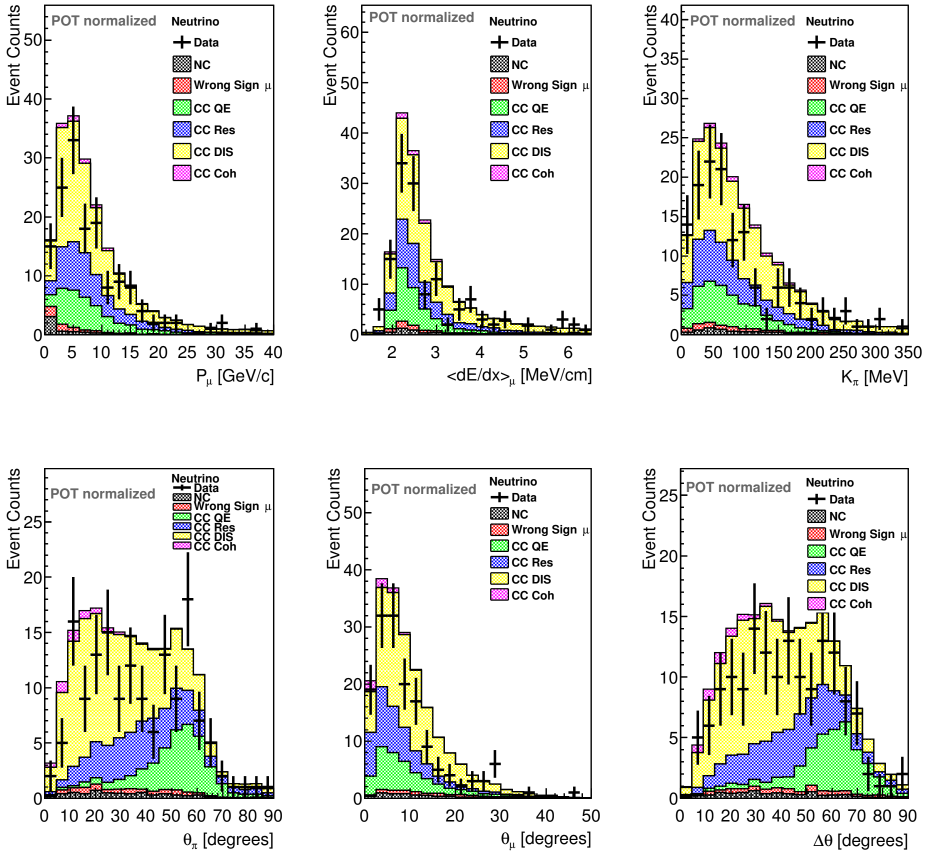

Figure 4.16: Same as Figure 4.15 but for neutrino interactions.

4.5.1 The Boosted Decision Trees

The classification algorithm relies on the use of the Monte Carlo simulation to *learn* the discriminating features of signal and background events and summarise the classification in one output value which retains most of the variation present in all the input parameters. This purpose is accomplished using two Boosted Decision Trees (BDTs) to classify neutrino and antineutrino events separately. The ROOT Toolkit for Multivariate Analysis [134] provides a library of tuneable machine-learning algorithms and it was used to create the BDT's used in this analysis. The BDTs are trained using the characteristics of the events generated by GENIE. The following paragraphs summarise the main properties of the BDTs used and how they are optimised to evaluate the ArgoNeuT data.

A decision tree [135] consists of a chain of cuts that, depending on the brach followed, leads to a signal or a background classification. A decision tree used in this analysis is shown in Figure 4.17. As outlined in the previous sections, the decision is made by considering a set of input parameters $\mathbf{x} = (\theta_\pi, \theta_\mu, \Delta\theta, P_\mu, K_\pi, \langle dE/dx \rangle_\mu)$ and each decision tree is defined by a set of parameters, $\mathbf{p}$, which are cut values or decision values at each tree node. The classification provided by one decision tree alone, $f(\mathbf{x}, p_i)$, is very sensitive to statistical fluctuations on the training data. This is overcome by the use of *Boosting* [136], which consists on the construction of a robust classifier based on many weak classifiers. The BDT combines the prediction of many decision trees to deliver a classification which is more stable with respect to fluctuations in the input parameters. In practice, the BDT response, $F(\mathbf{x})$, is averaged over the N decision trees used:

$$F(\mathbf{x}) = \sum_{i=1}^{N} \beta_i f_i(\mathbf{x}, p_i). \tag{4.10}$$

The weights, β_i, and the tree parameters, $\mathbf{p}_i$, have to be optimised to minimise a loss function $L(y', F(\mathbf{x}))$, which evaluates the difference between the true classification value (y') and the BDT output. This is accomplished using the Gradient Descent Method [137], which evaluates in which direction in the (β_i, p_i) phase space the gradient $\partial L/\partial F$ is steepest. This optimisation search is iterative and the steps given in any given direction of the parameter space can be reduced by an *ad hoc* factor, the learning rate or shrinkage parameter ($\in]0, 1]$).

In this analysis, a small shrinkage parameter is used, 0.01. This enhances the robustness of the classification but demands more trees to be grown, which increases the computational burden associated to the training and use of the BDT. For the analysis shown, 10000 trees were used. The performance of the BDT improves as the number of trees increases, although above some number there is no significant improvement of the results. The weights associated to each tree were found by minimising a loss function the "gini-index" $P(1-P)$, there P is the purity of the selection.

The BDT built for this classification also benefits from the use of *Bagging.* Bagging consists in the partitioning of the training data into random subsamples. Each tree is grown using 80% of the available data set, with events randomly selected. This effectively corresponds to a smearing of the training data and stabilises the response of the BDT as, in practice, the response is averaged over subsets of the training data set.

The issue of "overfitting" is particularly important in this analysis, as the modelling of especially the signal is a matter of debate. The most important measure taken to minimise the bias towards the training model was the rebinning of the GENIE signal and background templates. The histograms in Figure 4.18 show the expected pion momentum and angle for signal events in $\bar{\nu}_\mu$ interactions. The prediction is shown for two different neutrino generators – GENIE and NuWro. The top histograms have small bins which allow for fine structure features to arise, enhancing the difference between the two generators. Using a coarser binning – histograms on the bottom – that fine structure is removed. In the BDTs used, the entire range of possible values for each input parameters is divided in only twelve bins, which affects the decision values which can be selected for each tree node (again, see Figure 4.17). This strategy makes the final BDTs less sensitive to differences between the data and the training sample. The goal is to have the BDT perform at least as well as human hand-scanning while keeping a systematic and automated analysis scheme. In the hand-scanning approach, "small-angle" events are classified as signal and larger angles are classified as background without relying on detailed information on the priors – the model expectation. Inspection of event displays revealed that the classification obtained with the BDTs was in agreement with the physicist-decision. An example of an event classified as signal is shown in Figure 4.19.

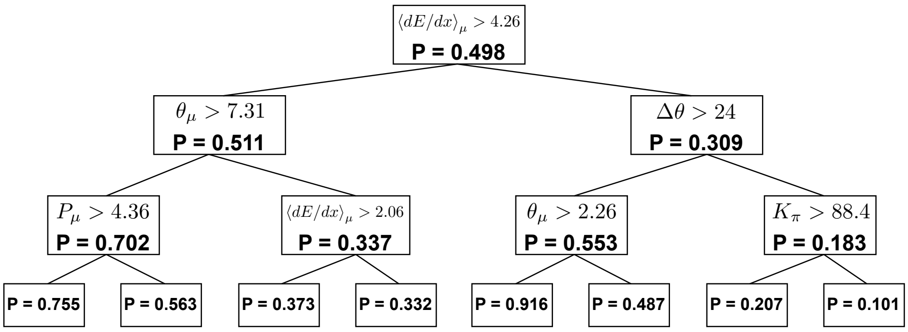

Figure 4.17: One of the 10 000 decision trees used for classifying the events. The purity, $P = s/(s+b)$, is shown. For decision nodes (the three first layers) the purity values are the result of each decision node alone; for the bottom nodes, the purity is the one achieved by combining the decision nodes above.

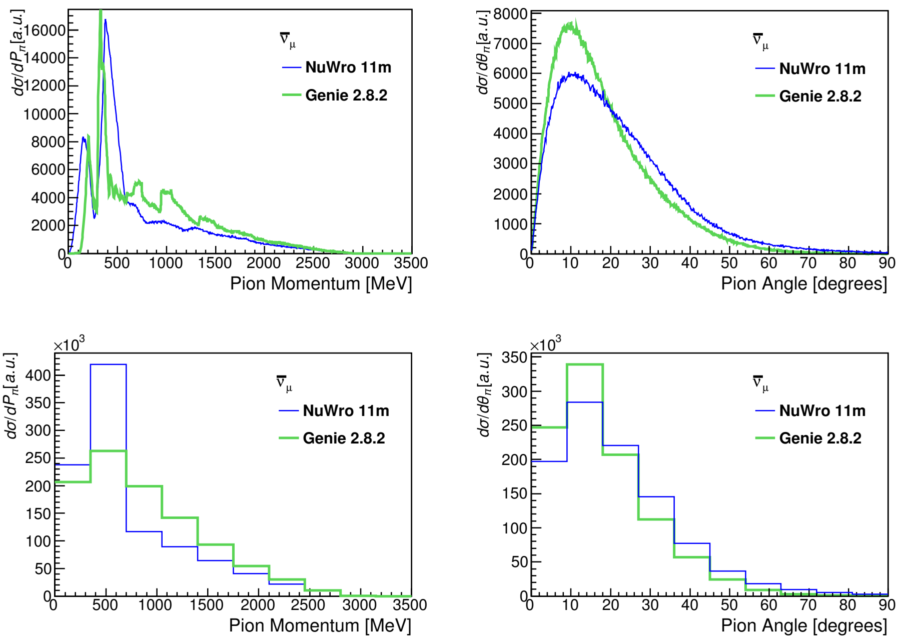

Figure 4.18: On the top, antineutrino probability of generating pions at some value of momentum and angle as given by GENIE 2.8.2 and NuWro 11m. On the bottom, the same probabilities rebinned. Rebinning the Monte Carlo decreases the bias towards the model used to train the BDT.

4.5.2 Summary of the Event Classification

Two BDTs were trained to independently classify ν_μ and $\bar{\nu}_\mu$ interactions using Monte Carlo samples of signal and background events. The Monte Carlo is based on GENIE 2.8.2 which uses the RS model for modeling the coherent production of pions. The events which are used for the BDT training pass a set of reconstruction cuts. The observables used for classification are the angles of the muon and pion with respect to the neutrino incoming direction, the opening angle between the muon and the pion, the momentum of the muon, the energy deposited by the pion in ArgoNeuT, and the average stopping power of the first third of the muon track. The reconstruction cuts and the BDT are applied on the data and on a Monte Carlo sample of events different from the one used in the training of the BDT. The results are shown in the histograms of Figure 4.20 which will be used to estimate the coherent signal present in the data sample. From these histograms it stands out that there is a disagreement on the background scale. The separation between the background and signal peaks found in the Monte Carlo expectation can also be seen in the data. There seems to be good shape agreement, although a conclusion can only be made after the fit discussed in the next section.

The performance of each selection stage is summarised in Tables 4.3 and 4.4 where we define the signal region of the BDT as all events assigned with an output value greater than zero. The signal region is defined here only for a benchmarking purpose, it is not used to define the number of signal events for the cross section calculation. The fitted signal is worked out in a later section of this work and it results from a statistical analysis of the entire range of BDT output values. As can be seen in Tables 4.3 and 4.4 and Figure 4.20, a relatively pure sample of signal events is expected to be identified.

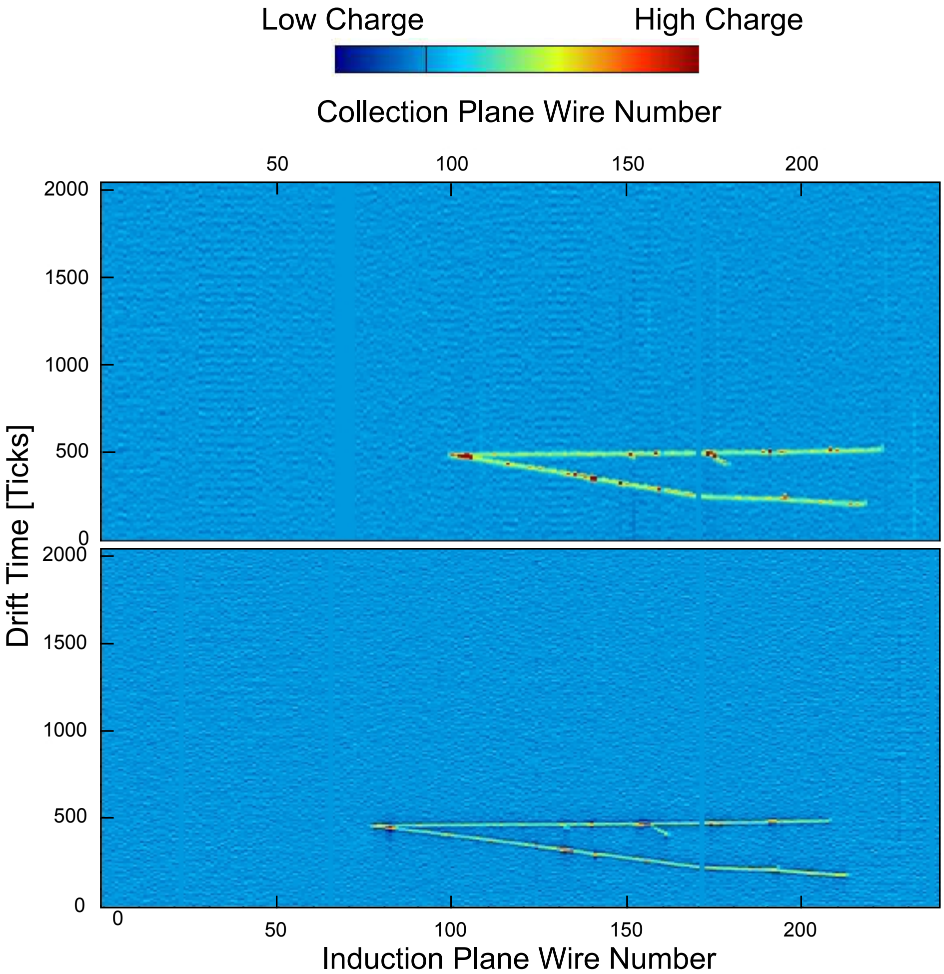

Figure 4.19: Example of a data event classified as signal by the BDT. The neutrino's incoming direction is along the horizontal coordinate; the muon track corresponds to the most forward going one, making an angle of 1.2° with the incoming neutrino direction. The opening angle between the muon and the pion track is 10.6°. A kink in the pion track can be seen.

Table 4.3: Expected number of signal and background events along with the number of events observed in data. The BDT signal region corresponds to a BDT classification value greater than 0. This Table summarises the results shown in Figure 4.20. The fractions of background and signal contained in each sample are shown. High purity is obtained in the BDT signal region: only 8.8% of the background events passing the reconstruction cuts leak into the signal region (3.7 from 42.2). The absolute scale of the background is still to be tuned to the data.

		Number of $\bar{\nu}_\mu$ After Selection (frac. of total)		
		2-Track Sample	Recon. Cuts	$BDT > 0$
Monte Carlo	NC	7.1 (3.0%)	1.4 (2.8%)	0.0
	CCQE	22.1 (9.5%)	5.0 (10.0%)	0.2 (1.8%)
	CCRES	110.1 (47.3%)	24.8 (49.5%)	2.6 (23.6%)
	CCDIS	78.8 (33.8%)	9.5 (19.0%)	0.7 (6.4%)
	Wrong-Sign muon	7.0 (3.0%)	1.5 (3.0%)	0.2 (1.8%)
	Total Background	225.1 (96.6%)	42.2 (84.2%)	3.7 (33.6%)
	CC Coh π	7.9 (3.4%)	7.9 (15.8%)	7.3 (66.4%)
	Background + Signal	233.0	50.1	11
Data		165	30	9

Table 4.4: The same as Table 4.3 but for neutrino events. Again, good separation between background and signal is obtained, with only 5.6% of the background having a BDT classification value greater than 0.

		Number of ν_μ After Selection (frac. of total)		
		2-Track Sample	Recon. Cuts	$BDT > 0$
Monte Carlo	NC	5.7 (2.8%)	1.2 (2.7%)	0.0
	CCQE	34.3 (17.1%)	12.3 (27.8%)	0.3 (5.8%)
	CCRES	43.8 (21.8%)	6.5 (14.7%)	0.5 (9.6%)
	CCDIS	108.3 (54.0%)	20.4 (46.1%)	1.3 (25%)
	Wrong-Sign muon	5.5 (2.7%)	0.9 (2.0%)	0.2 (3.8%)
	Total Background	197.6 (98.6%)	41.3 (93.4%)	2.3 (44.2%)
	CC Coh π	2.9 (1.4%)	2.9 (6.6%)	2.9 (55.8%)
	Background + Signal	200.5	44.2	5.2
Data		139	24	8

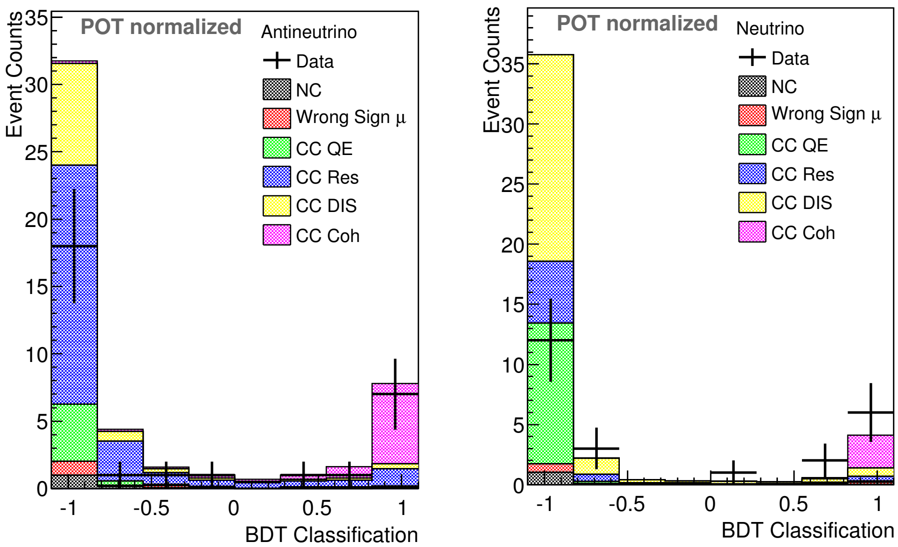

Figure 4.20: Classification output for data and Monte Carlo samples. The Monte Carlo prediction, which is normalised to the same POT as the data, overestimates the number of events found in the data. The signal fit will be insensitive to this difference, only the shape of the background and signal are important. The histograms show all individual background contributions and signal stacked. The leakage of background into A small contribution from NC background can be seen. This is due to the matching of charged particles emerging from the neutrino interaction to muons in the MINOS detector which are not related to the ArgoNeuT event.

4.6 Extraction of the Signal

Figure 4.20 shows the binned expectation of signal and background with the observed data superimposed on it. The expected content u_i of each bin is given by:

$$u_i = Bb_i + Ss_i; \tag{4.11}$$

where b_i and s_i describe background and signal shapes while the scales B and S determine the total level of background and signal. The fit of the

Monte Carlo expectation to the data will preserve the shapes while changing the scales. The statistic used for the estimation and goodness-of-fit testing is the Poisson likelihood χ^2 [138]:

$$\chi^2 = -2\ln\lambda = 2\sum_{i=1}^{N}\left[\mu_i - d_i + d_i \ln\frac{d_i}{\mu_i}\right]; \tag{4.12}$$

where the sum is over all bins and d_i is the number of data events found in bin i. For bins with no data entry, the logarithmic term is zero. The total number of signal events, n_s, is the integral of the best-fit signal histogram:

$$n_s = S\sum_{i=1}^{N} s_i. \tag{4.13}$$

The number of background events, n_b, is found in an equivalent way.

The statistic defined in Equation 4.12 covers a two-dimensional phase space, where a χ^2 value is calculated for each signal and background scale hypothesis. In Figures 4.21 and 4.22, the best fit results are shown along with the χ^2 values found for each signal hypothesis (n_s). Note that for each n_s value shown an optimal estimation of the background, n_b, was found. The $\chi^2(n_s)$ curved represented is a projection of $\chi^2(n_s, n_b)$. The statistical error is found by evaluating the central confidence interval determined by $\Delta\chi^2 = \chi^2 - \chi^2_{min} = 1$. The number of degrees of freedom is equal to the number of bins minus the number of parameters in the fit – which are two, the signal and background scales B and S. The best fit values found were verified to be robust against different choices of binning (three to ten bins in total).

The best-fit background histograms correct the background scale. Figure 4.20 overestimates the number of background events to expect, this is due to well-known flux scale uncertainties. The number of background events leaking into the high BDT value is low, so a high purity sample of CC coherent π events is identified.

The significance with which the absence of coherent signal is excluded is also estimated repeating the fit assuming $S = 0$. Table 4.5 lists the χ^2 values obtained. The no-signal model is disfavoured with respect to the signal hypothesis at 2.5 and 2.2 standard deviations (antineutrino and neutrino, respectively).

It stands out that the statistical uncertainty associated with the number of signal events is large, 37% to 47%, and will dominate the total uncertainty associated to the cross section estimation. A large statistical error was expected from the beginning, due to the small cross section of CC coherent π production and the limited exposure available for analysis.

Table 4.5: χ^2 values for best fit to signal+background and background only hypothesis. The no signal model is disfavoured with respect to the signal hypothesis at 2.5 and 2.2 standard-deviation levels.

	$\bar{\nu}_\mu$	ν_μ
χ^2_{min}/ndf	1.6/6	8.6/6
χ^2_{min}/ndf (no signal)	7.8/5	13.6/5
$\sigma = \sqrt{\Delta\chi^2}$	2.5	2.2

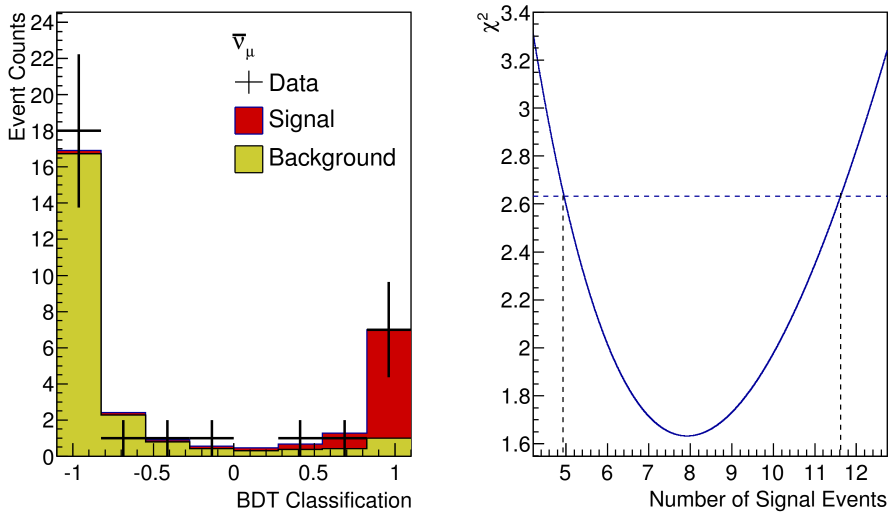

Figure 4.21: On the left hand side, antineutrino data with the best background and signal fit. The background estimation is 22.3 events; the signal is 7.9 events. The minimum χ^2 is 1.6. On the right hand side, the horizontal dashed line represents $\Delta\chi^2 = \chi^2_{min} + 1$ and it defines the statistical error interval $^{+3.7}_{-3.0}$.

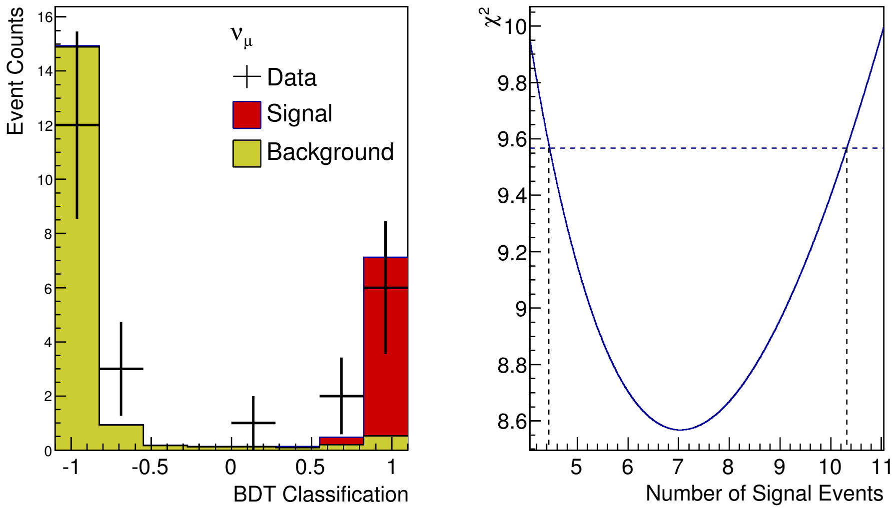

Figure 4.22: The equivalent to Figure 4.21, but for the neutrino data. The best background estimation is 16.5 events; the best signal fit $7.0^{+3.3}_{-2.6}$. The minimum χ^2 is 8.6.

4.7 Systematic Errors

Several sources of systematic uncertainty affecting this cross section measurement have been considered. The estimation of the uncertainty associated with most sources of systematic error has already been performed in previous ArgoNeuT and MINOS analyses. The next paragraphs summarise these sources and describe how the errors are propagated to the cross section uncertainty. A breakdown of all systematic errors is shown in Table 4.7.

4.7.1 Background Scale

The cross section for the background processes (the charged current QE, RES, DIS and a negligible NC) have large uncertainties in the few GeV energy range, $\sim 20\%$ [50]. These uncertainties are propagated to the cross section estimation by scaling each background component present in histograms of Figure 4.20 by $\pm 20\%$. The signal extraction is repeated and the number of signal events found leads to a new cross section value. The difference between this value and the original cross section is the systematic error.

4.7.2 Wrong-sign Muon

The mis-identification rate of the muon charge in MINOS is estimated in the Monte Carlo simulation. The muon charge can be mis-identified when the muon leaving ArgoNeuT is matched to the wrong muon track in MINOS or when the muon is correctly matched but the MINOS charge identification fails to evaluate correctly the curvature of the trajectory, which can happen for very short or straight tracks. The expected background of wrong-sign muons can be seen in Figure 4.20. The uncertainty associated with this background should be relatively large: a value of 20% was assumed. The signal extraction was repeated scaling the background by the hypothesised uncertainty and the difference in the final cross section was kept as the systematic uncertainty.

4.7.3 Nuclear Interactions

Final state interactions (FSI) emerging before the particles produced by the neutrino interaction leave the target nucleus have an impact on the visible topology of the events. GENIE does not add FSI to coherent interactions and this analysis will keep that assumption. All that needs to be evaluated is the FSI impact on the background. This is done by finding the fraction of events that had their interaction products changed to $\pi + \mu$ by FSI – shown in Table 4.6. We associate a large uncertainty to these estimations ($\pm 20\%$) and reweigh each FSI-added event accordingly. The uncertainty assumed is conservative and at the same level as the uncertainties associated to the background scale.

Table 4.6: Fraction of background added by FSI, listed by interaction mode and neutrino parent. The table is built by analysing the Monte Carlo sample that passes the reconstruction cuts; for these events, the number of pions and protons produced by the neutrino interaction (prior to any addition of FSI effects) are counted. Events that are generated with some other topology that 2 charged tracks are counted as FSI generated.

	FSI Generated [%]	
	$\bar{\nu}_\mu$	ν_μ
CC QE	100	100
CC RES+DIS	34.4	78.7
NC	22.5	14.4

4.7.4 Muon Momentum Resolution in MINOS

The MINOS muon momentum has an associated error of [139]:

$$\frac{\delta P_\mu}{P_\mu} \approx 4\%.$$

The impact of this error on the cross section is estimated by repeating the entire analysis using a reconstructed Monte Carlo MINOS muon momentum scaled up or down by 4%.

4.7.5 Angle Resolution in ArgoNeuT

The evaluation of this systematic is similar to 4.7.4. The angular resolution for tracks reconstructed in ArgoNeuT is 1° [131], found by comparing true trajectory angles with reconstructed ones in the Monte Carlo simulation of the detector. The uncertainty on the cross section is found by repeating the analysis with the ArgoNeuT reconstructed track angles smeared by 1°.

4.7.6 POT, Flux Normalisation, Efficiency

The POT and flux normalisation systematic errors are 1% [140] and 11% [139] respectively. These errors only affect the final cross section calculation after the the signal has been estimated (see equation 4.3). The calculation is repeated assuming integrated fluxes scaled by the POT and flux normalisation errors.

Just in the same way, the uncertainty associated to the efficiency is propagated by scaling the efficiency estimated by its uncertainty.

4.7.7 Number of Argon Targets

The uncertainty on the number of Argon targets originates from the uncertainty on determining the active volume [131]. The uncertainty on the Y and Z dimensions, measured using the crossing positions of the wires has an uncertainty of 1 mm; the X dimension is obtained from the electron drift-time has an uncertainty of approximately 1 cm. Combined, these lead to an uncertainty on the number of argon targets equal to 2.2%. Uncertainties associated with the density of the liquid argon or Avogadro's constant are considered negligible.

4.7.8 Signal Modeling

Most of the debate concerning the analysis presented was about the model dependancy due to the use of the BDTs which are trained using GENIE priors. In order to evaluate the dependance of the measurement on the priors, another generator (NuWro) was used to provide the signal template used to fit the data. Note that the BDTs used remain the same, only the Monte Carlo on which they are applied is different. The difference found was in the estimation of the number of signal events was 0.9% and 5.7% and these values are fixed as the systematic uncertainty associated to the choice of model. Note that despite the fact that the two generators use the same model (Reign-Sehgal), they deliver different signal shapes due to the use different hadronic data and more or less updates to the formalism – GENIE is the most up-to-date.

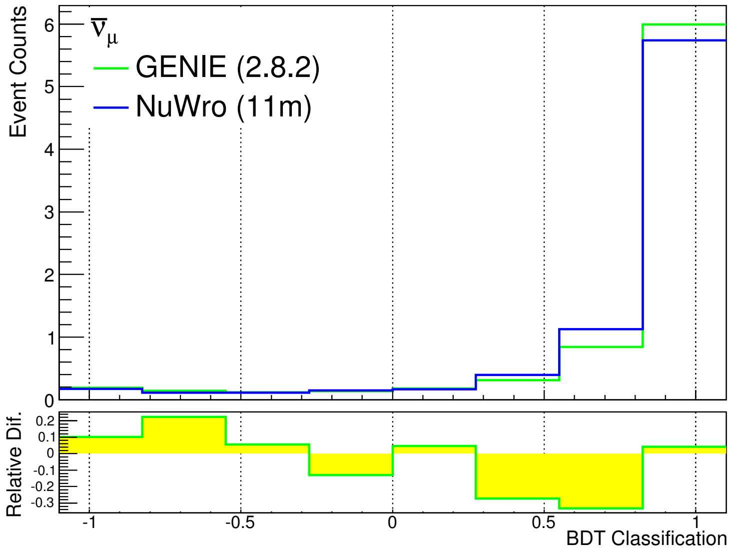

Figure 4.23: Comparison of the signal templates obtained with NuWro and GENIE. The the difference in the number of signal events obtained with the two is kept as the systematic error (0.9%).

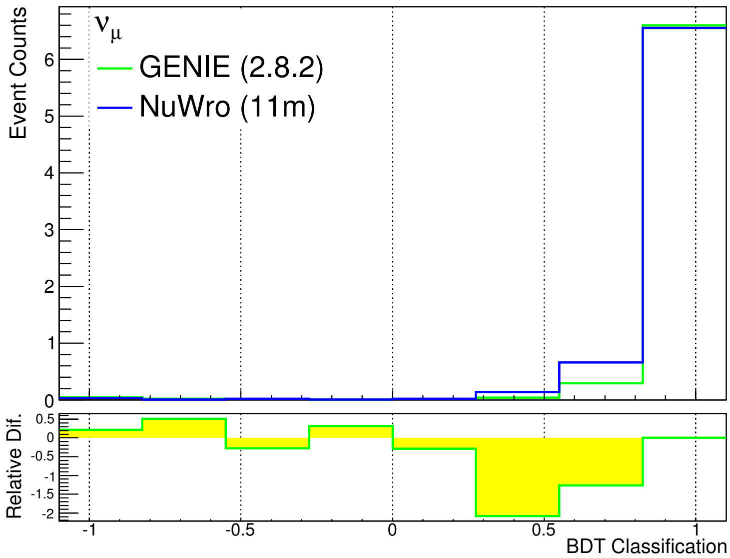

Figure 4.24: Same as Figure 4.24 but for neutrino. The difference on the number of signal events estimated is more significant in this case, 5.7%.

		Cross section uncertainty [%]	
	Systematic Effect	$\bar{\nu}_\mu$	ν_μ
Background	CC QE	$^{+0.3}_{-0.4}$	$^{+1.2}_{-0.6}$
	CC RES	$^{+0.2}_{-0.5}$	$^{+0.4}_{-0.3}$
	CC DIS	± 0.1	± 0.3
	NC	± 0.1	± 0.1
	Wrong-sign μ	± 0.1	± 0.2
Nuclear Effects		± 0.3	± 0.7
Recon.	MINOS momentum res.	± 4.1	± 4.3
	ArgoNeuT angle res.	± 1.6	± 2.7
POT		± 1.0	± 1.0
Flux normalization		$^{+10.0}_{-12.0}$	$^{+10.0}_{-12.0}$
Number of Ar targets		± 2.2	± 2.2
Efficiency		± 0.8	± 1.8
Signal modeling		± 0.8	± 5.7
Total systematics		$^{+11.3}_{-13.1}$	$^{+12.9}_{-14.5}$

Table 4.7: Breakdown of systematic errors. The systematic errors associated to the background shape and scale have small contributions. This is due to the low number of background events expected in the signal region bins. The reconstruction uncertainties, in particular the angular one, are more relevant as the discrimination between signal and background depends on them. The leading systematic uncertainty comes from the flux normalisation.

4.8 The Cross Sections

The cross sections are calculated using Equation 4.3. The number of targets is 2.26×10^{27} argon atoms, estimated using the fiducial volume $41\,\mathrm{cm} \times 32\,\mathrm{cm} \times 80\,\mathrm{cm} = 104.96\,\mathrm{dm}^3$. The efficiencies and integrated fluxes are listed in Table 4.8. Using the estimations of the number of signal events

	$\epsilon(\%)$	$\int \phi\, dE$ (neutrinos.cm^{-2})
$\bar{\nu}_\mu$	21.8	2.94×10^{12}
ν_μ	18.4	6.56×10^{11}

Table 4.8: Efficiencies and integrated flux values used for the calculation of the cross section. The efficiency is calculated in Section 4.4.4 and the integrated fluxes result from the integration of the histograms in Figure 4.2.

(Section 4.6), the flux-averaged cross sections for CC coherent π production are found to be:

$$\left\langle \sigma_{\bar{\nu}_\mu} \right\rangle = \left(5.5^{+2.6}_{-2.1}(stat)^{+0.6}_{-0.7}(syst)\right) \times 10^{-39} cm^2, \tag{4.14}$$

$$\left\langle \sigma_{\nu_\mu} \right\rangle = \left(2.6^{+1.2}_{-1.0}(stat)^{+0.3}_{-0.4}(syst)\right) \times 10^{-38} cm^2. \tag{4.15}$$

A comparison with neutrino generator predictions and other experimental data is shown in Figure 4.25. The antineutrino measurement is in agreement with the generators while the neutrino measurement shows a 1.2σ deviation.

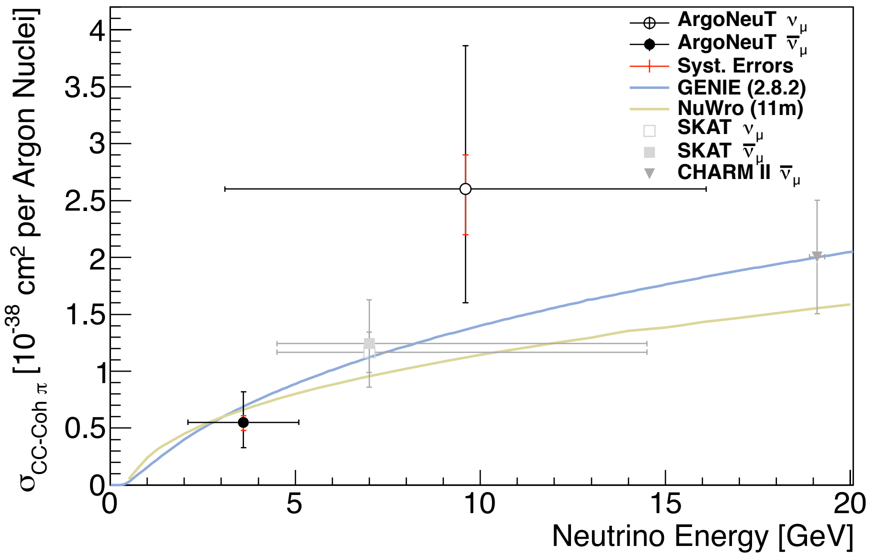

Figure 4.25: ArgoNeuT's cross section measurements (○ and ●) compared to generator prediction. Existing data from other experiments measuring CC coherent π production in the few GeV energy range is also shown. These consist in measurements made by SKAT (■,□) and CHARM II (▼) [82, 141]. All measurements are scaled to Argon assuming the $A^{1/3}$ dependance from the Rein-Sehgal model.

4.9 Conclusion

A sample of CC coherent π production events was identified in the ArgoNeuT detector and cross section values for neutrino and antineutrino interactions were extracted. The analysis relies on a set of cuts and a BDT classification for identification of the signal events. The analysis is robust as small differences in the final results are found by tweaking the cuts, the BDT training or the binning of the histograms for the final signal fit. Hand-scanning was also used to confirm the BDT classification.

There is some tension between the measurements presented and the null results from K2K and SciBooNE. The cross sections found are also in good agreement with the state-of-the-art RS prediction encoded in GENIE, although model testing is not the goal of this analysis, owing to the large statistical uncertainties. The low number of events available are a limiting factor, but nevertheless, the capabilities of the detector were well exploited and a measurement was possible: the resolution of the event vertex and the precise calorimetry of the events are at the foundation of this analysis. Similar experiments due to start operating soon such as MicroBooNE and LAr1-ND will collect hundreds/thousands of coherent π production events and may provide measurements crucial for the modelling of this interaction.

The success of this analysis is also important for future long baseline neutrino oscillation experiments which are planned to use liquid argon detectors. The capability to produce automated analysis of liquid argon data is a necessary feature as the number of interactions to be analysed in those experiments makes hand-scanning impractical.

It is also important to point out that the leading systematic error in this analysis, the flux uncertainty, is likely to persist in future experiments. As discussed in Chapter 3, this is an issue inherent to all cross section measurements and will remain inescapable until new ways of generating neutrino beams are put into practice.

5 Muon ionization Cooling and the MICE Experiment

5.1 Introduction

What most distinguishes nuSTORM from a Neutrino Factory is the lack of a muon acceleration stage. This would require ionization cooling, a technique set to be demonstrated by the Muon ionization Cooling Experiment, MICE. In this Chapter, an overview of some fundamental accelerator concepts is given and the MICE experiment is introduced.

5.2 Beam Emittance

A few accelerator concepts are necessary for the understanding of what MICE is set to measure. The most fundamental of these is the *beam emittance.* It is frequently used as a figure of merit for the quality of particle beams as it is a measure of the dispersion and divergence of the particles in the beam.

As particles move along an accelerator, they oscillate in the plane transverse to the beam line axis due to non-zero divergence angles which cause them to stray from the central trajectory. The use of quadrupole magnets brings particles back to the central trajectory but only by inverting the direction of the divergence. These transverse oscillations are known as *betatron oscillations.* From the mathematical description of this movement arises an important quantity, the Courant-Snyder invariant [142]:

$$C(x, x') = \frac{1}{\beta}\left[x^2 + (\alpha x + \beta x')^2\right] = \gamma x^2 + 2\alpha x x' + \beta x'^2; \qquad (5.1)$$

where x represents one of the directions transverse to the beam axis, and

$x' = dx/ds$ is the divergence angle of the particles trajectory with respect to the beam line direction where s is the total path length of the particle's trajectory. Equation 5.1 represents an ellipse in the (x, x') plane. The phase-space enclosed by this ellipse is equal to $\pi\epsilon$ and ϵ is known as the transverse emittance of the particle and has units of length or length×angle and is fully determined from the initial conditions. Even though other parameters might change, modifying the shape of the ellipse, the area remains constant all around the accelerator length, as long as only conservative forces come into play. This is the single-particle emittance.

When considering a many-particle beam, the emittance can be specified in a different way. After measuring x and x' for each particle in the beam, many points can be added to the (x, x') phase-space. An ellipse can then be drawn, containing a certain percentage of the points. A 95% emittance would correspond to a ellipse area containing 95% of the particles. Figure 5.1 illustrates this concept.

The emittance, ϵ, defined as the area of the ellipse described by Equation 5.1 is not invariant when the energy of the particle changes, for example due to transport with acceleration. For this reason, a *normalised emittance*, conserved during acceleration, is defined using the Lorentz relativistic factor (γ):

$$\epsilon_N = \beta\gamma\epsilon. \tag{5.2}$$

In conjugate phase-space coordinates (x, p_x) with $p_x = px' = mc\beta\gamma x'$, where m is the mass of the particle and p its momentum, we obtain the Liouville invariant phase-space area [143].

From studying the evolution of the (x, x') distributions in beams it follows that the emittance can be quantified using the the moments of the beam (variances and covariances) in an "r.m.s. emittance" defined by Lapostolle [144]:

$$\epsilon_N^{4D} = \frac{1}{mc} \left|\mathrm{V}(x, p_x, y, p_y)\right|^{1/4}; \tag{5.3}$$

where m is the mass of the particle in the beam and V is the covariance matrix of the beam phase-space parameters. This is a 4D emittance value because it is computed from the 4 transverse parameters x, p_x, y, p_y; the full 6D emittance can be calculated when measurements of time and particle energy are added.

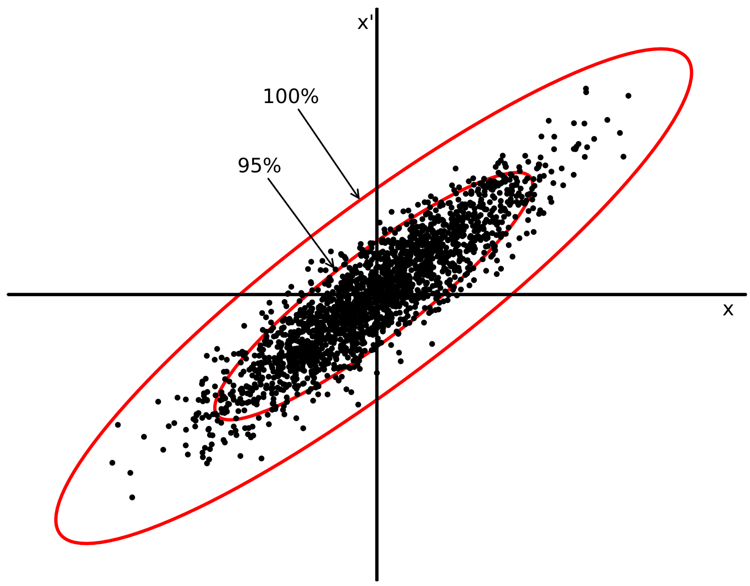

Figure 5.1: An example of (x, x') phase-space distribution. Ellipses containing 100% and 90% of the particles are shown.

5.3 ionization Cooling

Cooling techniques are used to control the emittance of particles in a beam, decreasing the space and momentum phase-space they occupy along the acceleration process. Currently, electron, laser and stochastic cooling are the methods available for this purpose, and the theorised ionization cooling technique [45] remains untested. Compared to other cooling techniques, ionization cooling has the advantage of taking effect in a much shorter timescale.

The principle of ionization cooling is to pass the particle beam through an absorber in which both transverse and longitudinal momentum are reduced, followed by momentum restitution in the longitudinal direction by RF cavities. The process can be repeated a number of times, resulting in progressive reduction of the transverse emittance. Multiple Coulomb Scattering introduces an undesired counter effect (see Figure 5.2), so the choice of absorber material must be optimised to maximise the net emittance change. For a muon beam crossing an absorber in a focusing magnetic lattice the rate of change of the normalised transverse emittance is [145]:

$$\frac{d\epsilon_N}{dz} = -\frac{1}{\beta^2}\left|\frac{dE_\mu}{dz}\right|\frac{\epsilon_N}{E_\mu} + \frac{\beta_\perp(0.014\mathrm{GeV})^2}{2\beta^3 E_\mu m_\mu X_0}, \tag{5.4}$$

where $\beta_\perp$ is the lattice beta function, X_0 the radiation length of the absorber medium, E_μ and m_μ the muon energy and mass, $\beta = v/c$ and $\left|\frac{dE_\mu}{dz}\right|$ is the mean rate of muon energy loss in the medium, given by the Bethe-Bloch equation. The first term in Equation 5.4 is the "cooling" part, which describes the emittance reduction via energy loss; the second term is the "heating" term due to the multiple scattering in the absorber material. The best balance is obtained by choosing low atomic number materials such as liquid hydrogen. It is also important to note that the cooling is more efficient if the absorber is placed in a region where the beam highly convergent or divergent. To achieve this, superconducting magnets are added to the absorber region, which makes the design and construction of cooling cells a complex problem.

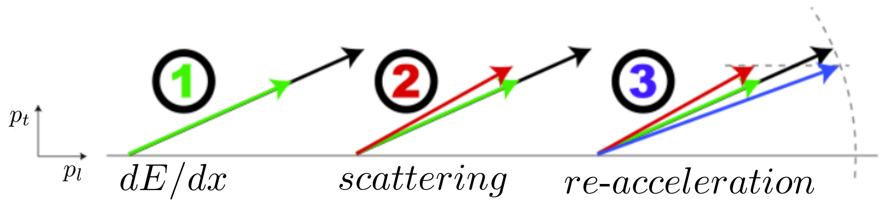

Figure 5.2: Schematic representation of the cooling concept. The change in transverse momentum (p_t) and longitudinal momentum p_l is shown using the coloured arrows. (1) and (2) take place in the absorber material while (3) is introduced by RF cavities. In (1), the particle's momentum is reduced due to the energy loss in the absorber (black to green arrow). (2) represents the multiple scattering which adds some "heating" (green to red arrow). At (3), the re-acceleration in the RF cavity restitutes the longitudinal momentum, the net effect is a reduction of the transverse momentum. *Image credit:* [146].

5.4 MICE

The MICE collaboration aims to demonstrate ionization cooling. This is part of the pathway to the construction of a Neutrino Factory or Muon Collider as these facilities would require high quality muon beams which cannot be cooled using conventional techniques as they are not compatible with the short muon lifetime. The fundamental part of the MICE beam line is a section of what could be a neutrino factory cooling channel, the performance of which is to be measured in several modes of operation and beam conditions. In its final form, MICE's cooling channel is expected to reduce the emittance by about 10% [147]. The experiment is being constructed at the Rutherford Appleton Laboratory [148].

5.4.1 Beam line and Detectors

The production of muons for the MICE experiment starts at the ISIS 800 MeV proton-beam [149]. When a titanium target is dipped into the proton-beam halo, a pion beam is extracted from the synchrotron and transported into the MICE Hall (Figure 5.3). The transport starts with the capture of charged particles by an arrangement of three quadrupoles (triplet). This is followed by a dipole which is used to bend the particle's trajectory through the ISIS wall, selecting them according to their momentum. Embedded in the ISIS wall, there's a 5 m long superconducting 5 T decay solenoid where the field induces helical trajectories which increase the path length of the charged particles coming through and in which most pions decay to muons. A second dipole is used to produce a clean muon beam by accepting muons of a desired momentum and excluding protons and undecayed pions. Finally, a large acceptance transport channel consisting of two sets of quadruple triplets delivers the beam to MICE.

A detailed drawing of the MICE components is shown in figure 5.4. As can be seen, the arriving beam finds a sequence of three detectors, used to identify particles within the beam - muons, and contaminating pions and protons. The first set of detectors the muon beam arrives at are two time-of-flight chambers (Time-Of-Flight (TOF)0 and TOF1) and a Cherenkov detector. These are followed by a tungsten or brass diffuser which is used to control the input emittance of the beam. The beam then reaches the first scintillating fibre (Scintillating fibre detector (SciFi)) spectrometer which

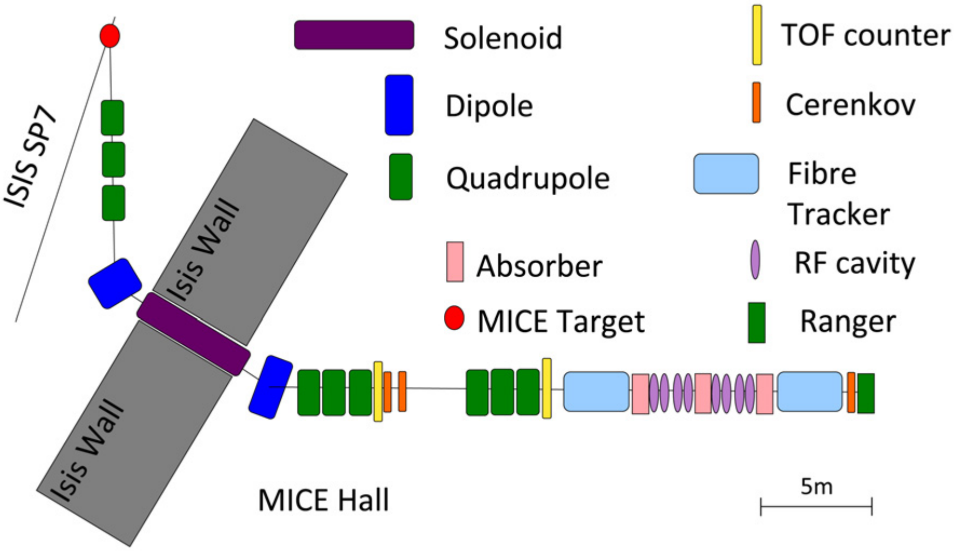

Figure 5.3: Extraction beam line, from ISIS to MICE. *Image credit: MICE collaboration.*

is inside a 4 T solenoid. The upstream spectrometer will provide precise measurements of position and transverse momentum which will be used for the calculation of the 4D emittance just before the muon beam reaches the cooling channel; combined with the time measurements of the TOF detectors, the full 6D emittance can be calculated. The cooling channel consists of a sequence of absorbers and 201.25 MHz RF cavities placed within a solenoidal magnetic field. After the cooling channel, another SciFi spectrometer and a TOF detector (TOF2) are in place to measure the change in emittance and an electromagnetic calorimeter (KLOE-like scintillating fibre detector (KL)/Electron-Muon Ranger (EMR)) is also added at the end of the beam-line in order to reject beam contamination via further particle identification.

The cooling channel cell is composed of an absorber module (made of liquid hydrogen or lithium hydride) followed by an RF cavity which cool the muon beam according to the simple scheme depicted in Figure 5.2. The absorber material used in the cooling cell is chosen taking into account the effectiveness of the cooling provided and the liability of its usage. Low Z materials are preferred as the cooling performance depends on keeping the scattering low compared to the amount of energy loss induced (see Equation 5.4). Liquid-hydrogen is a favoured option, as the cooling it induces is maximised by a combination of large ionization energy loss and small probability for multiple-scattering. However, some tests with lithium-hydride are also being planned, since it is a more practical alternative, even though it is a less effective "cooler". The focus coils which surround each absorber module are used to reduce the transverse beta function ($\beta_\perp$), a requirement for optimal cooling - again, see Equation 5.4. In the complete setup, the last absorber is installed in order to protect the downstream spectrometer from dark current and X-ray backgrounds arising in the RF cavities.

Finally, the two pairs of matching coils shown in Figure 5.4, match the beam such that there is a smooth transition from the cooling channel to the upstream and downstream spectrometers.

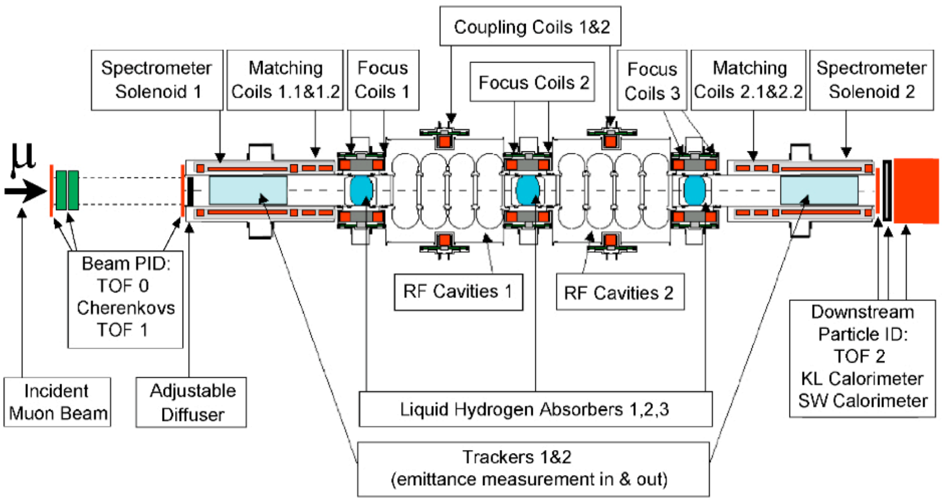

Figure 5.4: Schematic view of the MICE cooling channel and the two SciFi spectrometers. The layout depicts two cooling cells (absorber followed by RF cavity) and beam line elements used to control the optics of the beam (matching coils and focus coils). *Image credit: MICE collaboration.*

5.5 Experimental Stages

The final shape of the MICE experiment shown in Figure 5.4 was envisaged to be achieved in a set of steps, where detectors and beam components are gradually added. In an early stage, the muon beam was characterised using only the TOF and Cherenkov detectors, on a beam line which only contained the quadrupoles, dipoles and decay solenoid.

At the time of this writing, the SciFi spectrometers are also in place but have not been operated inside the solenoidal field. They have been used in test runs, measuring cosmic rays. The addition of parts to the cooling channel is due to start within months, with the installation of the first absorber and focus coil. This is to be followed by the addition of the first RF cavity which completes the first cooling cell, at which point a measurement of ionization cooling can be attempted.

5.6 The SciFi Spectrometers

The set of detectors deployed along the beam line aims at characterising the muon beam before and after the cooling channel. Fundamental in these measurements are the two SciFi spectrometers or trackers, as they are commonly referred to. These detectors are identical, each is composed by five stations, 32 cm diameter, made of three planes of scintillating fibre. The fibres in each plane make an angle of 120° with the fibres in other planes. The spacing between stations is unique (see Table 5.1) in order to disambiguate the turning angles of the particles travelling in the solenoidal field.

The main fibre material is polystyrene doped with compounds to produce scintillation light and to re-emit this light at a frequency suitable for the electronic readout. Polythiophene is the primary scintillating dopant and it is present at the level of 1.25% by weight; the wavelength shifting dopant is 3-Hydroxyflavone and it is present at 0.25% by weight. The fibres are 350 μm diameter and they are arranged in a double layer for each plane. The light output to the electronics is arranged in a seven-fibre gauged readout as shown in Figure 5.6. The pitch of these readout channels is 427 μm. By combining the measurements made in each plane, it is possible to track particles crossing these detectors with sub-mm scale position resolution – see Figure 5.7.

The light produced in the fibres is transported to Visible Light Photon Counters (VLPCs) which are operated at cryogenic temperatures [150]. The VLPCs are impurity band conduction silicon diodes with high gain (20000 to 60000) and high quantum efficiency (better than 80%). Each photon

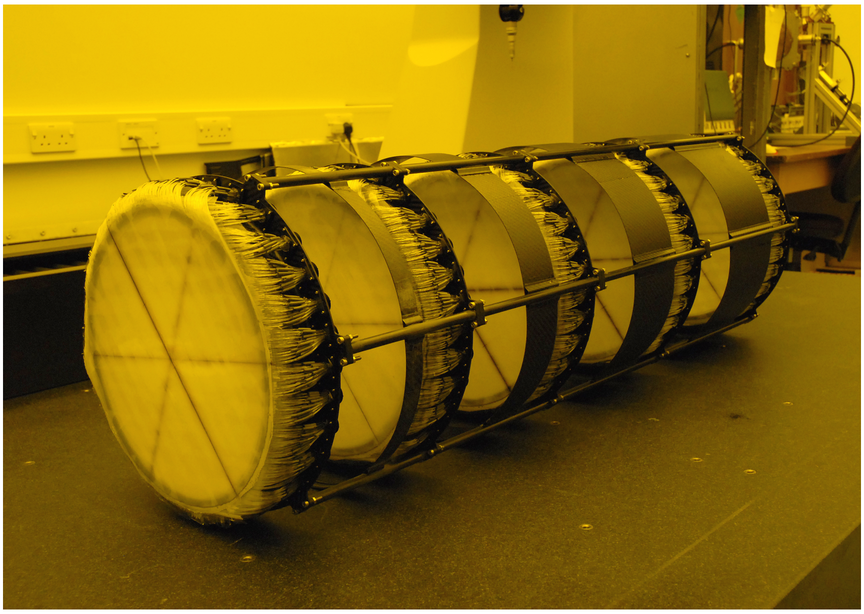

Figure 5.5: The tracker stations photographed outside the coffin which protects them from the light.

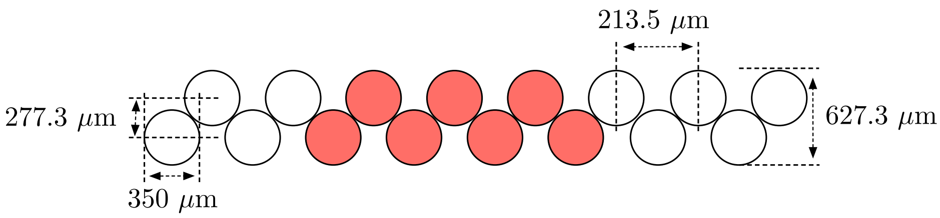

Figure 5.6: Fibre arrangement in each tracker plane. The fibres in red represent a readout channel.

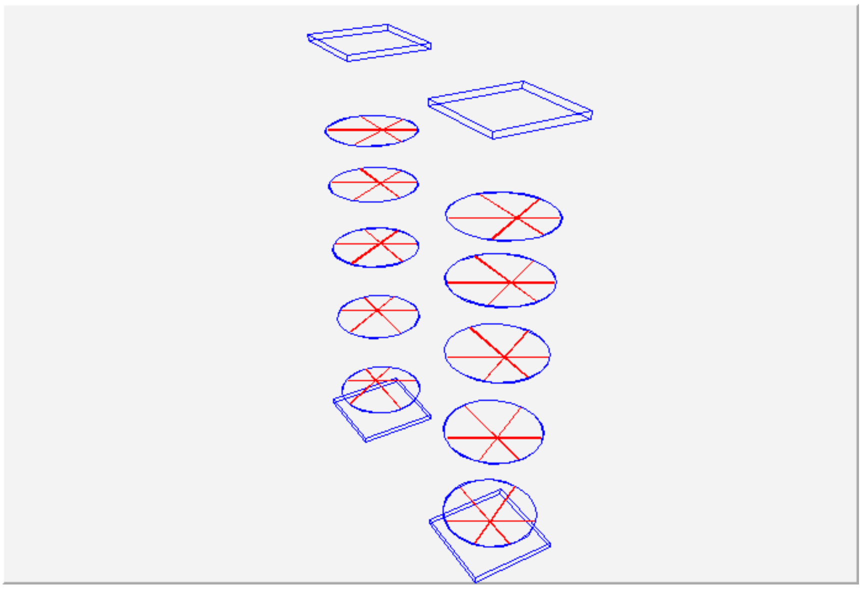

Figure 5.7: Example of two cosmic-ray events in both trackers during a cosmic test run. The fibre plane orientation in each station is used to locate the crossing position of particles coming through with 470 μm resolution per layer.

collected induces an electron avalanche which generates a signal amplitude sufficient to be measured.

5.6.1 Reconstruction

Reconstruction of tracks of particles crossing the trackers follows a single-particle method. Such a method has the advantage of improving the precision in the measurements, as the presence of the solenoidal magnetic field in the tracker and cooling channels leads to strong correlations between the coordinates to be measured, introducing a bias in the emittance measurement. Also, the single-particle reconstruction makes it easier to take into account particle losses, separating this effect from the cooling measurement. The stages of track reconstruction are described in the following paragraphs.

Hit finding

The hits must be identified on the individual VLPC channel and associated with the appropriate group of seven scintillating fibres. Only signals corresponding to one photo-electron or more are accepted.

Table 5.1: Specifics of each of the SciFi spectrometers.

Parameter	Value
Number of stations	5
Station Diameter (cm)	32
Station Spacing 1-5 (cm)	20;25;30;35
Number of planes per station	3
Number of Channels per plane	212-214
Fibre radius	350 μm
Channel Pitch	427 μm

Clustering

Because there is some superposition between adjacent readout channels (see Figure 5.6), a particle might produce a signal in two neighbouring channels at the same time. If this happens, the two channel hits are clustered and a pulse-height weighted mean position is calculated for the hit. Clusters, which might be composed of one or two hits, are only accepted if the signal is equal or higher to two photo-electrons.

Space-point reconstruction

A space-point results from the intersection of clusters in a station. The search for intersections of three clusters is attempted first and these are called "triplets". Figure 5.7 shows cosmic-ray events producing triplets in all stations. Once all triplets are found, any remaining clusters which belong to a same station but different views are combined to form a "duplet". The plane efficiency is very high ($\sim 99\%$) so most events produce triplets.

Track finding

The muons traveling through the solenoidal field inside the spectrometer have helical trajectories. The track finding algorithm finds collections of space-points which fit a helix and estimates the corresponding transverse and longitudinal momentum.

Track fitting

A Kalman Filter is used to determine with improved precision the track parameters that describe the track candidate found by the track finding routine. The following Chapter presents a detailed description of this reconstruction stage.

5.7 Precision Requirements

The precision requirements for the success of the experiment have been formulated in references such as [151–153]. It is stated that, in order to measure the expected change of emittance ($\sim 10\%$), the absolute emittance before and after the cooling channel must be measured with a precision level of 0.1%. This translates into a requirement on the precision with which the phase-space parameters are reconstructed: the resolution must be better than 14% for each parameter. The next Chapter documents the construction of a precise track fitting routine which uses the measurements made with the SciFi spectrometers. The precision of the track fitting is evaluated and compared to the requirement for the success of the emittance measurement.

5.7.1 Emittance Unfolding

The emittance calculated using Equation 5.3 is affected by detector errors. The unfolding of the emittance value in MICE has been worked out in reference [153]. Assuming each measured parameter, m, is affected by errors, δ, the true parameter value, w, is

$$w_i = m_i + \delta_i. \tag{5.5}$$

Using this expression to expand the true covariance matrix in terms of measurements and errors, one finds that the true covariance, V_{true}, is related to the measured on, V_{meas}, through the covariance matrices:

$$\mathrm{C}_{ij} = \mathbf{cov}(\delta_i, \delta_j) \tag{5.6}$$

and

$$\mathrm{R}_{ij} = \mathbf{cov}(w_i, \delta_j). \tag{5.7}$$

The final relation between measured and true covariance matrix is

$$\mathrm{V}_{true} = \mathrm{V}_{meas} - \mathrm{R} - \mathrm{R}^{\mathrm{T}} - \mathrm{C}. \tag{5.8}$$

Finding the correction matrices 5.6and **??** requires running the Monte Carlo simulation with a setup that replicates the one in which the measurements are made. The formulas here shown, extracted from [153], will be used in the next Chapter.

5.8 Summary

The MICE collaboration which aims at making precise measurement of emittance change in a portion of a Neutrino Factory cooling channel relies on the SciFi spectrometers placed before and after the cooling section to make precise measurements of the position and transverse momentum of the muons, which will yield a measurement of the 4D emittance $\epsilon(x, p_x, y, p_y)$. The track fitting routines must render a precision better than 14% on each parameter. This is so that the desired resolution in the emittance (1%) is compatible with the emittance change expected in the cooling channel (10%).

6 Track Fitting with the MICE Scintillating Fibre Trackers

Track fitting consists in characterising the position and momentum of the particles which left signal in a detector. In High Energy Physics, this is typically a task which must be as precise as possible as the physics results depend on it. To satisfy this purpose, the Kalman filter technique is applied to the measurements made with the SciFi spectrometers. The method was introduced by Kalman in his 1960 seminal paper [154] and then widespread in high energy physics after Frühwirth's [155] and Billoir's [156] publications in the 80s. This Chapter documents the implementation of the technique taking into account the SciFi spectrometers specifics. The results obtained using Monte Carlo simulation of the detectors are also shown.

6.1 Track Fitting Generics

Decades of expertise have been accumulated on pattern recognition and track fitting techniques in High Energy Physics. The building blocks for a tracking algorithm are: a *track model* which describes the path of the particle in the detector, a *measurement equation* which relates the (x, y) coordinate in the detector volume with the corresponding detector measurement (α), the resolution of the measurements (σ_α) and, finally, an accurate description of the geometry of the detector. When it comes to discussing the options for the track fitting method, the argument is usually about the benefits of the Kalman Filter when compared to the Global Least Squares Method (LSM) [157]. The LSM minimises a χ^2 of the form

$$\chi^2 = \sum_{i=1}^{N} \left(\frac{\alpha_i - h_i(\mathbf{a})}{\sigma_\alpha} \right)^2 \tag{6.1}$$

where the numerator is the difference between measurement i, and the expected measurement $h_i(\mathbf{a})$, assuming a set of fit parameters $(\mathbf{a})$. Therefore, the resulting best-fit track corresponds to an unscattered prolongation of the same set of parameters across the whole detector - see Figure 6.1. In matrix notation the χ^2 can be written:

$$\chi^2 = r^T \mathrm{V}^{-1} r; \tag{6.2}$$

where r is the residual vector and V is the measurement covariance matrix assumed to be diagonal. The Kalman Filter, on the other hand, is a recursive algorithm in which the track parameters are free to change, to some degree, at each point the particle being tracked finds some material. This is because multiple Coulomb scattering (MCS) and energy loss add noise to the otherwise deterministic track model which defines the trajectory of the particle. In the absence of process noise, the Kalman Filter is equivalent to the global least squares fit.

Although the foundations of the Kalman Filter formalism assume that the process and measurement errors are Gaussian random variables, it can be shown that the Kalman Filter is still the best linear estimator if these assumptions are dropped [158]. The validity of the Gaussian assumptions will have an impact on the χ^2 of the fit, as will be discussed in a later section of this Chapter.

Traditionally, the track fitting routine is preceded by a *track finding* algorithm which associates collections of hits which are likely to belong to the same track. There are, however, a few instances where algorithms have been designed to perform track finding and track fitting simultaneously using the Kalman Filter. This might be desirable, for instance, in collider experiments where the track fitting starts from the outward layers and propagates towards the inner layers where the hit density is higher. In this case, the outer hits are used to build an estimate of the track parameters which, extrapolated to the inner region, can suggest which hits belong to the track.

Besides grouping the measurements that are likely to form the same track, the track finding algorithm provides also an initial estimate of the track parameters. The Global Least Squares Method is a suitable option for this purpose. In the following stage, the track fitting algorithm, employing the Kalman Filter, produces the optimal estimate of the track parameters. In

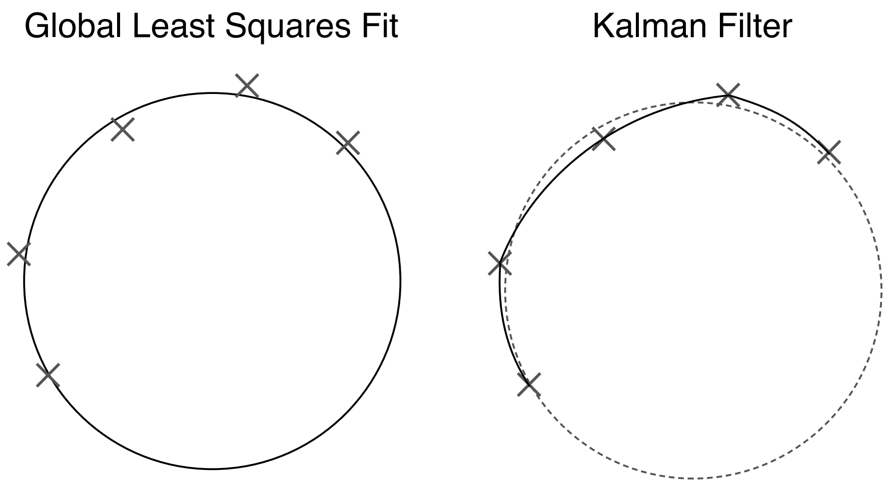

Figure 6.1: Illustration of the difference between the Global Least Squares fit and the Kalman Filter for the fitted parameters. The same set of points is shown on the left and right hand side. On the left, the Global Least Squares fit finds a unique set of parameters which minimises the residuals over the whole track. On the right, the Kalman Filter finds the best set of parameters at each measurement point. Multiple scattering changes the momentum direction, which means the arc line is broken at each interaction point. The Kalman Filter finds the optimal fit in the sense that the residuals are minimal and the position resolution is determined only by the measurement resolution.

this setup, the track finding routine must have a broad acceptance and the track candidate constructed is ultimately kept or rejected by a goodness-of-fit test performed by the track fitting routine.

Summarising, the goals of the track fitting routine are to compute the best estimate of the track parameters and to produce a confidence test which confirms the hypothesis that the measurements put together represent a particle's trajectory. In order to compute this test statistic, a covariance matrix must be associated to each fitted point. In the following sections, it will be shown how these goals are met by a Kalman Filter, while keeping tracking routines numerically stable and robust against error estimates. The final track parameters are optimal at the plane nearest to the cooling channel, to be used in emittance studies and also optimal at the opposite end of the detector, for extrapolation to other MICE detectors.

6.2 Geometry Layout

The SciFi trackers are laid out in a forward geometry (in contrast with cylindrical geometry of collider detectors), with fixed z planes of scintillating fibres. The measurements in these planes must be used to find the optimal estimation of position and momentum for the MICE muons before and after the cooling channel. In each tracker, the stations are numbered from 1 to 5, with the first station placed closest to the cooling channel. The symmetric layout of the tracker stations is shown in Figure 6.2. Each station is composed of three layers of scintillating fibre making an angle of 120° with respect to the others. The magnetic field in each detector points towards the cooling channel and has 4 T magnitude.

Following the symmetry of the detector arrangement, the muons crossing the spectrometers are reconstructed using a “detector-local” reference frame which is mirrored around the cooling channel. For each of the two detectors, the reference frame is centred at the plane closest to the cooling channel, with the positive z axis pointing down the detector and the y axis pointing vertically upwards.

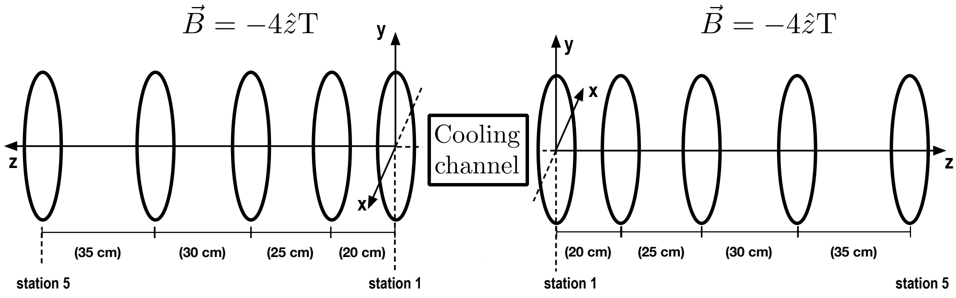

Figure 6.2: Schematic representation of the placement of the SciFi spectrometer stations with respect to the cooling channel. The reference frame adopted for the track fit in each detector is also shown. The magnetic field in each detector is parallel to the axis and has the direction of the increasing z. Each station contains three fibre planes.

6.3 Track Parameters and Track Model

Each track is characterised by a set of parameters which are allowed to change along the propagation through the detector. This parametrisation contains information about the position (x, y, z) and momentum (p_x, p_y, p_z) of the particle. In this work, the parametrisation chosen consists of the 5-dimensional state vector:

$$\mathbf{a} = \begin{bmatrix} x \\ p_x \\ y \\ p_y \\ \kappa \equiv Q/p_z \end{bmatrix}; \tag{6.3}$$

where Q is the charge of the particle. The rule to extrapolate the state vector along the detector length is a fundamental ingredient in the track fitting routine and it is usually referred to as the *track model.* Typically, the state vector is chosen such that the correlation between elements is minimised. The track fitting set up is prepared to handle both helical and straight trajectories.

6.3.1 Helical Trajectories

If the solenoidal field inside the tracker volume is set, the particles describe helical trajectories from which the transverse momentum components can be determined. The projection of the helical path on the xy plane renders a circle of radius R which is related to the transverse momentum of the particle p_t by:

$$p_t = cBQR \tag{6.4}$$

where B is the magnitude of the magnetic field, Q is the charge of the particle and $c \approx 0.299\,\mathrm{MeV/cT^{-1}mm^{-1}}$. The magnetic field in the tracker volume is expected to be uniform (4 T) and aligned with the axis of the detector which we defined as the z direction (revisit Figure 6.2). The distance between planes, Δz, is constrained to fixed, well known, distances and the turning angle between measurements, $\Delta\theta$, depends on these. $\Delta\theta$ can be calculated using the ratio between longitudinal and transverse momentum:

$$\frac{\Delta z}{R\Delta\theta} = \frac{p_z}{p_t}; \tag{6.5}$$

from which:

$$\Delta\theta = \frac{p_t \Delta z}{R p_z} \tag{6.6}$$

$$= \frac{cBQR\Delta z}{R p_z} \tag{6.7}$$

$$= \frac{u\Delta z}{p_z}, \tag{6.8}$$

where $u \equiv cBQ$. The charge of the particle defines the sense of rotation: for positive charged particles $\Delta\theta < 0$ so the rotation is counterclockwise (see Figure 6.3).

The helical trajectory of the muons follows the system of parametric equa-

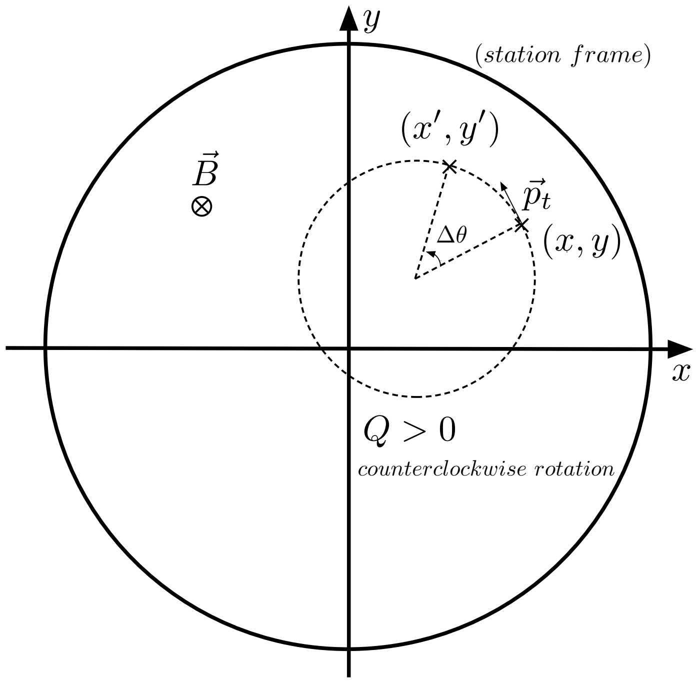

Figure 6.3: Some of the track parameters for the helical fit. For positively charged particles, the rotation is counterclockwise. The station frame, which corresponds to the boundary of the active volume of the detector planes is represented only as a reference.

tions:

$$x' = x + \frac{p_x}{p_t} R \sin\Delta\theta - \frac{p_y}{p_t} R(1 - \cos\Delta\theta) \tag{6.9}$$

$$y' = y + \frac{p_y}{p_t} R \sin\Delta\theta + \frac{p_x}{p_t} R(1 - \cos\Delta\theta) \tag{6.10}$$

$$z' = z + \Delta z \tag{6.11}$$

$$p'_x = p_x \cos\Delta\theta - p_y \sin\Delta\theta \tag{6.12}$$

$$p'_y = p_y \cos\Delta\theta + p_x \sin\Delta\theta \tag{6.13}$$

$$p'_z = p_z; \tag{6.14}$$

from which we can write the evolution of the state vector, noting that $R/p_t = 1/u$:

$$a' = \begin{bmatrix} x' \\ \\ p'_x \\ \\ y'_k \\ \\ p'_y \\ \\ \kappa' \end{bmatrix} = \begin{bmatrix} x + \frac{p_x}{u}\sin\Delta\theta - \frac{p_y}{u}(1-\cos\Delta\theta) \\ \\ p_x\cos\Delta\theta - p_y\sin\Delta\theta \\ \\ y + \frac{p_y}{u}\sin\Delta\theta + \frac{p_x}{u}(1-\cos\Delta\theta) \\ \\ p_y\cos\Delta\theta + p_x\sin\Delta\theta \\ \\ \kappa \end{bmatrix} \tag{6.15}$$

where we also defined $\kappa = Q/p_z$. The equations of motion for the helical trajectories are non-linear and, as a consequence, the Kalman Filter can not be applied in its standard form. The variation used is known as the Extended Kalman Filter. The particularities of both are discussed in Section 7.5.

6.3.2 Straight Trajectories

It is desirable to be able to fit tracks in the absence of magnetic field. In this case, the momentum can not be determined, only the gradients $m_x = p_x/p_z$ and $m_y = p_y/p_z$. The state vector used in this case is simply $a = [x, m_x, y, m_y]^{\mathrm{T}}$.

The equations of motion for the straight trajectories are trivial. They can be interpreted as a particular case of the equations for the helical motion. Using the small angles approximation ($\sin\Delta\theta \approx \Delta\theta$, $\cos\Delta\theta \approx 1$) and

$\Delta\theta/u = \Delta z/p_z$ we can write:

$$\mathbf{a}' = \begin{bmatrix} x' \\ \\ m'_x \\ \\ y' \\ \\ m'_y \end{bmatrix} = \begin{bmatrix} x + m_x \Delta z \\ \\ m_x \\ \\ y + m_y \Delta z \\ \\ m_y \end{bmatrix}. \tag{6.16}$$

In the absence of process noise (MCS and energy loss), the track gradients remain unchanged. The capability of fitting straight lines will be useful for test runs and alignment verifications. It is also practical for track fitting studies as it can be used to check several detector and material assumptions while using a simpler, linear, track model.

6.4 Measurement Equation

Each (x, y) point in a detector plane corresponds to a fibre channel measurement – see Figure 6.4. In the track fitting formalism, the measurement is represented by a vector, $\mathbf{m} = [\alpha]$, which in this case is unidimensional. The measurement equation transforms the track-parameter vector into the measurement vector:

$$h(\mathbf{a}) = \mathbf{m} = [\alpha]. \tag{6.17}$$

The transformation depends on the direction of each fibre plane, $\mathbf{d} = (d_x, d_y, 0)$. For any point $\mathbf{P} = (x, y, z)$, the perpendicular distance $d_\perp$ to the central channel is the modulus of the cross product:

$$d_\perp = |\mathbf{d} \times \mathbf{P}| \tag{6.18}$$

$$= y d_x - x d_y (\text{mm}). \tag{6.19}$$

Using the channel width, w, this corresponds to a channel distance:

$$\alpha = \frac{d_\perp}{w} = \frac{y d_x - x d_y}{w}. \tag{6.20}$$

It is desirable to be able to write the transformation 6.17 in matrix notation:

$$h(\mathbf{a}) = \mathrm{H}\mathbf{a}. \tag{6.21}$$

Using 6.20, we can write

$$\mathrm{H} = \begin{bmatrix} -dy/w & 0 & dx/w & 0 & 0 \end{bmatrix}. \tag{6.22}$$

The error associated with the measurement is stored in the measurement covariance matrix:

$$\mathrm{V} = [\sigma_\alpha^2]; \tag{6.23}$$

where $\sigma_\alpha = w/\sqrt{12}$ is the variance of the channel measurement, given that the probability of measuring α is uniform over the channel width $w = 1$. This uniformity is in conflict with the assumption of Gaussian errors.

The matrices H and V will be used in the Kalman Filter. The considerations made so far deserve several remarks. First, it is worth pointing out that the raw channel measurements are used in the fit, rather than spacepoints constructed from these. The construction of spacepoints can represent both the loss of information and addition of bias to the position estimation. Secondly, one could consider that the measurement vector is in fact two-dimensional, with a second coordinate ω being added. This would be a measurement in the direction of the fibre plane and the uncertainty in each measurement would correspond to the total length of the channel hit. The measurement error in this coordinate is very large and can lead to divergence of the filter. By not adding this coordinate, we are approximating that ω does not add information to the filter.

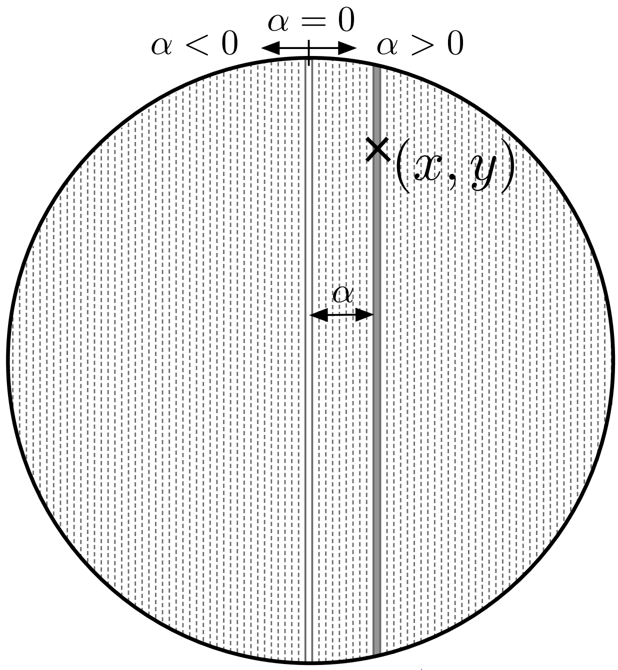

Figure 6.4: The plane measurements correspond to scintillating fibre channel, α, which is the number of channels measured from the center. $\alpha > 0$ towards the right and increasing negative from the left.

6.5 Kalman Fitting Routines

Some of the tools necessary for the task of track fitting have already been introduced: the geometry definition, the track model, the measurement equation and the estimation of the measurement resolution. In this section we explore how these are employed by the Kalman Filter to deliver an optimal estimation of the track parameters. The stages of the Kalman filtering are standard and these paragraphs are meant to provide only an overview of the process for completeness. The superscript/subscript notation followed in this text is the same as in Frühwirth's [155]. The matrices (capital roman letters) and vectors (lower case bold) are tagged with superscript and subscript indices that run over the discrete measurement sites $k = 0, 1, 2, ..., 15$ for events where all detector planes yield a measurement.

Initialisation

Being a recursive algorithm, the Kalman filter requires an estimate of the initial values to be fitted. At the initialisation stage, an initial *state vector* ($\mathbf{a}$) and *covariance matrix* (C) are defined for the first measurement plane. The covariance matrix is constructed under the assumption that the initial errors are uncorrelated, so it is assumed to be diagonal. The initial position estimate, (x, y), is taken from the spacepoint formed in that station; the variance associated to it is the spacepoint resolution. The other components of the state vector are as found by the Pattern Recognition and the variance associated to them is randomly large ($\mathrm{C}_{ii} = 1000$), giving them little weight in the following steps of the filter, so that the final result isn't biased towards the initial values.

Some caution is necessary at this stage: if the covariance matrix is initialised with values too large, the early steps of the calculation might diverge. It can be shown that for the estimation error remains bounded if the initial estimation error and the measurement error are small enough [159].

After the first guess of state vector and its covariance is built, a measurement is added. The track is then extrapolated to the next measurement plane where a new measurement is added and this two-step sequence is repeated until all measurements are used. The step in which a measurement is added into the fit is known as the *filtering* stage.

Filtering

The filtered matrices and vectors are written with a subscript denoting the site k where they are constructed. For example, the measurement vector at site k is $\mathbf{m}_k$ and the filtered state vector at the same site is $\mathbf{a}_k$. The filtered estimates are the result of combining the measurement information with the projected estimations. The projected vectors and matrices are written with two indices, a superscript denoting the site extrapolated from and a subscript denoting the site extrapolated to. Using these conventions, the filtered state is written as:

$$\mathbf{a}_k = \mathbf{a}_k^{k-1} + \mathrm{K}_k \left(\mathbf{m}_k - \mathrm{H}_k \mathbf{a}_k^{k-1} \right) . \tag{6.24}$$

The term in parenthesis is easy to interpret: it is the difference between the measurement vector registered at site k and an *expected measurement* at that site computed using the H matrix. This difference is known as the *measurement pull*. It is used to update the projected state estimation, $\mathbf{a}_k^{k-1}$, using a weight matrix, the Kalman Gain, K_k. The Kalman Gain is computed from the error matrices for the measurement (V) and for the projected state (C):

$$\mathrm{K}_k = \mathrm{C}_k^{k-1}\mathrm{H}_k^{\mathrm{T}}\left(\mathrm{V}_k + \mathrm{H}_k\mathrm{C}_k^{k-1}\mathrm{H}_k^{\mathrm{T}}\right)^{-1}. \tag{6.25}$$

The covariance matrix is also updated, according to:

$$\mathrm{C}_k = \left(\mathrm{I} - \mathrm{K}_k\mathrm{H}_k\right)\mathrm{C}_k^{k-1}. \tag{6.26}$$

In practice, the Kalman Gain defines how strong the pull towards the measurement is. For example, if the measurements are very precise and the confidence on the state estimation is small (large values in the covariance matrix) then the pull towards the measurement will be strong. This is the case at the first steps of the filter. Once enough measurements have been accumulated, the track extrapolation errors become comparable to the measurement error.

Extrapolation

After the addition of the measurement at a given site $(k-1)$, the track is extrapolated to the following measurement plane (site k) by following the deterministic equations of motion:

$$\mathbf{a}_k^{k-1} = f(\mathbf{a}_{k-1}). \tag{6.27}$$

The extrapolation requires the propagation not only of the state vector but also the covariance matrix associated with it. For that purpose, the *propagator matrix*, which is is the Jacobian of the track model is built. In the simple case where the track model is analytic, the Jacobian is also analytic:

$$\mathrm{F}_{k-1} = \frac{\partial \mathbf{a}_k^k}{\partial \mathbf{a}_k^{k-1}}. \tag{6.28}$$

In the case of straight-track fitting, one can write the predicted state vector as:

$$\mathbf{a}_k^{k-1} = \mathrm{F}_{k-1}\mathbf{a}_{k-1}. \tag{6.29}$$

For helical motion, the non-linearity of the equations of motion on the track parameters requires another approach, a variant of the basic Kalman Filter. In this method, the state vector is extrapolated using equation 6.27 directly and the matrix F is then calculated using a Taylor expansion about the local values of the state vector. This is the Extended Kalman Filter, which linearises about the current estimate at each measurement point.

In both the standard and Extended Kalman Filter cases, the covariance matrix is propagated taking into account the process noise. For minimum ionising particles, this consists of multiple Coulomb scattering (MCS) and energy loss (for higher energy particles, effects such as Bremsstrahlung might need to be taken into account). The projected covariance matrix is:

$$\mathrm{C}_k^{k-1} = \mathrm{F}_{k-1}\mathrm{C}_{k-1}\mathrm{F}_{k-1}^{\mathrm{T}} + \mathrm{Q}_{;k-1} \tag{6.30}$$

where Q_{k-1} is the multiple scattering covariance matrix. The multiple scattering affects the direction of the track in both planes perpendicular to the incoming particle's direction independently. This is a white noise process, the expected mean values are zero and the variance (θ_{MCS}) is given by the Highland Formula [160]:

$$\theta_{MCS} = \frac{13.6}{\beta cp} Z \sqrt{\frac{L}{L_0}}\,[1 + 0.038\ln(L/L_0).] \tag{6.31}$$

The multiple scattering angle distribution has non-Gaussian tails but the central distribution fits a Gaussian very well and can be accurately described by the Highland formula. Taking the momentum vector $\mathbf{p} = (p_x, p_y, p_z)$ and the position vector $\mathbf{x} = (x, y, z)$, the multiple scattering covariance matrix is calculated as [161]:

$$Q = \theta_{MCS}^2 \left[p^2 \frac{\partial \mathbf{a}}{\partial \mathbf{p}} P \frac{\partial \mathbf{a}}{\partial \mathbf{p}}^T + \frac{pl}{2} \frac{\partial \mathbf{a}}{\partial \mathbf{p}} P \frac{\partial \mathbf{a}}{\partial \mathbf{x}}^T + \frac{pl}{2} \frac{\partial \mathbf{a}}{\partial \mathbf{x}} P \frac{\partial \mathbf{a}}{\partial \mathbf{p}}^T + \frac{l^3}{3} \frac{\partial \mathbf{a}}{\partial \mathbf{x}} P \frac{\partial \mathbf{a}}{\partial \mathbf{x}}^T \right], \tag{6.32}$$

where an auxiliary matrix $P = I_{3\times3} - \hat{p}\hat{p}^T$ is used and l is the thickness of the material being transversed. Approximating 6.32 to the first term only is the thin layer approach; this approximation will not be made and the full calculation is performed when taking into account the length of air or scintillating fibre that is crossed.

The energy loss due to ionization is taken into account by subtracting the average energy loss from the particle's momentum, according to the Bethe-Bloch formula:

$$\Delta p = \int_0^l \frac{dp}{dx} dx = \int_0^l \frac{1}{\beta} \frac{dE}{dx} dx \approx \frac{1}{\beta} \frac{dE}{dx} l; \tag{6.33}$$

where the approximation consists of assuming that the velocity and stopping power of the muon are constant over the length of a fibre plane. The dE/dx is calculated using the formula and constants found in the Particle Data Group [162]:

$$-\frac{dE}{dx} = Kz^2 \frac{Z}{A} \frac{1}{\beta^2} \left[\frac{1}{2} \ln \frac{2m_e^2 c^2 \beta^2 \gamma^2 T_{max}}{I^2} - \beta^2 - \frac{\delta(\beta\gamma)}{2} \right]. \tag{6.34}$$

The direction of the fit is important: if the extrapolations follow the real direction of the propagation of the particle, it is said that the filter follows the energy loss and the correction to the energy corresponds to the small decrements of Equation 6.34; if the opposite direction is followed, then the energy correction corresponds to small increments. In this work, it was chosen to have the propagation follow the energy loss in the upstream detector and the opposite direction downstream so that in both detectors, the last site extrapolated to is the plane closest to the cooling channel.

The estimation of the system noise is an important step in the filtering process, as it affects the pull of the track parameters towards the measurements. While the MCS correction follows a stochastic model, which allows for some randomness, the energy loss is a deterministic correction, where the exact amount of momentum loss at each scattering layer is fully determined by the muon's momentum and the layer material.

Not all planes need to contain a measurement. If a plain lacks a measurement, the track is extrapolated through, taking into account the scattering error and the energy loss.

Smoothing

In the absence of stochastic noise the filtering stage renders the optimal estimate of the state vector for all sites. Otherwise, the filtered estimation at site k is more precise than the filtered estimate at site $k - n$ because it integrates information of n more measurements. In order to propagate all measurement information to the first measurement site, the smoothing stage reverts the direction of the filter, it back propagates all measurement information. The fundamental element for this task is the back-transportation matrix:

$$\mathrm{A}_k = \mathrm{C}_k \mathrm{F}_k^{\mathrm{T}} (\mathrm{C}_{k+1}^k)^{-1}; \tag{6.35}$$

from which the smoothed state vectors are calculated as:

$$\mathbf{a}_k^n = \mathbf{a}_k + \mathrm{A}_k(\mathbf{a}_{k+1}^n - \mathbf{a}_{k+1}^k); \tag{6.36}$$

and the covariance matrices as:

$$\mathrm{C}_k^n = \mathrm{C}_k + \mathrm{A}_k(\mathrm{C}_{k+1}^n - \mathrm{C}_{k+1}^k)\mathrm{A}_k^{\mathrm{T}}. \tag{6.37}$$

The smoothing stage ends the Kalman Filter routines.

6.6 Treatment of Detector Misalignments

Detector misalignments have an impact on the estimation of the track residuals and therefore must be taken into account. The complete integration of the misalignment information into the Kalman Filter not only handles the correction of the projected x and y values into the misaligned plane but also takes into account the precision of the misalignment estimation.

The addition of detector misalignments affects only the filtering stage. If an estimation of the misalignment values exists, $\mathbf{s} = [\Delta x, \Delta y, \Delta z = 0]^{\mathrm{T}}$, it is taken into account in the measurement equation:

$$h(\mathbf{a}) = \mathrm{H}\mathbf{a} + \mathrm{H}'\mathbf{s} \tag{6.38}$$

where H' converts the misalignment estimation into channel space in a manner similar to H in the filtering process for the state vector (see reference [163] for more details). This update to the measurement equation changes the measurement pull in Equation 6.24. The weight of the pull (Equation 6.25) is also changed by the uncertainties in the estimation of the misalignments, stored in the covariance matrix S:

$$\mathrm{K}_k = \mathrm{C}_k^{k-1}\mathrm{H}_k^{\mathrm{T}} \left(\mathrm{V}_k + \mathrm{H}_k \mathrm{C}_k^{k-1} \mathrm{H}_k^{\mathrm{T}} + \mathrm{H}'_k \mathrm{S}_k \mathrm{H}'^{\mathrm{T}}_k\right)^{-1}; \tag{6.39}$$

where the last term in parenthesis is the difference with respect to the

Kalman Gain introduced previously (Equation 6.25).

6.7 Goodness of Fit

For each fitted track, a figure of merit or test statistic evaluating the goodness of fit is computed. For a track made of N measurements, this corresponds to:

$$\chi^2_{track} = \sum_{k=1}^{N} \chi^2_k; \tag{6.40}$$

where the χ^2_k are computed from the residuals at each measurement:

$$\chi^2_k = r_k^T \mathrm{R}_k^{-1} r_k. \tag{6.41}$$

The residual r_k is computed from the filtered state vector:

$$r_k = m_k - \mathrm{H}_k a_k; \tag{6.42}$$

and the covariance matrix of the residuals is:

$$\mathrm{R}_k = \mathrm{V}_k - \mathrm{H}_k \mathrm{C}_k \mathrm{H}_k^T. \tag{6.43}$$

In contrast with Equation 6.2, the χ^2 introduced takes into account correlations in the measurement predictions. The multiple scattering introduces correlations between the measurements because a deviation of the trajectory in a plane affects the residuals in all planes that follow.

The number of degrees of freedom (ndf) in the fit is equal to the number of measurements (ideally 15) minus the number of parameters to be estimated (5). To some extent, the χ^2 distribution itself can already be used for testing the track fitting model: the mean must be equal to the expected ndf and the variance equal to $2ndf$.

The final goodness of fit test arises from the calculation of the probability value $P(\chi^2, ndf)$ associated to each track. This is the probability of observing a χ^2 as extreme or more than the one measured, admitting the *null hypothesis* is true, which in this case is the assumption that the measurements put together represent a particle's trajectory in the uniform solenoidal field. Very high residuals will correspond to low p-values and in practice a threshold P_{min} is set on the minimum p-value acceptable. Typically,

$P_{min} = 0.05$, and this can be used as a selection criteria for the acceptance of events for physics analysis. If all assumptions made during the track fit are valid, the p-value is uniformly distributed when the track candidates correspond to a real tracks. The failure of the Gaussian assumptions leads to a χ^2 which is not exactly χ^2 distributed and a p-value distribution not completely flat.

It is worth noting that the correction of misalignments is important as these affect the residuals. For a misaligned detector, the χ^2 does not follow a χ^2-distribution.

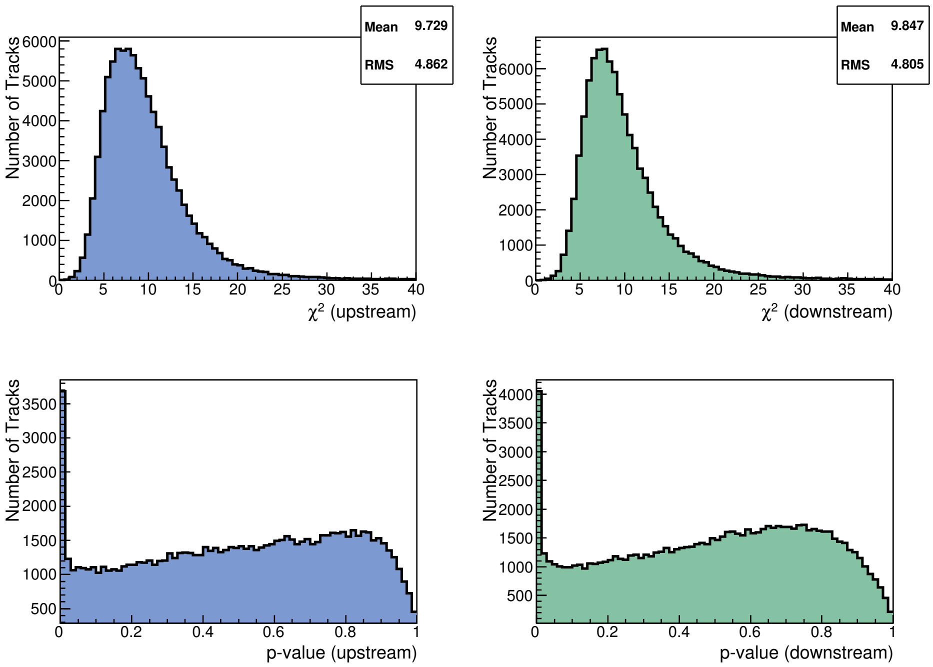

Figure 6.5: χ^2 and p-value of helical tracks fitted in the detectors upstream and downstream from the cooling channel. The peak near zero doesn't necessary mean that the fitted track is bad, it rather suggest the failure of the Gaussian assumptions made throughout the construction of the filter.

6.8 Resolution on the Track Parameters

The resolution on the track parameters is fundamental for the 4D emittance analysis which uses the position estimations (x, y) and the momentum components (p_x, p_y). In this section, the resolutions on these parameters are estimated using Monte Carlo simulation.

For each parameter $i = 1, ..., 5$ in the state vector, the residual

$$\Delta \mathbf{a}_i = \mathbf{a}_i^{fit} - \mathbf{a}_i^{MC} \tag{6.44}$$

is used to estimate the resolution of the fit – Figure 6.6. The histograms are obtained from the simulation of muon beams generated with emittance values uniformly distributed in the interval $[0.5,\ 9.5]\pi$ mm, which is representative of the emittance expected in the experiment. All central values are compatible with zero. The performance for fitting all transverse parameters, being that position or momentum, is very satisfactory. The residuals on the longitudinal momentum, however, show non-zero means. This limited precision on the longitudinal momentum is expected and it is one of the reasons why there are TOF detectors in the MICE beam line – the other one being particle identification.

It is also convenient to histogram the normalised residual:

$$\Delta \mathbf{a}_i^N = \frac{\Delta \mathbf{a}_i}{C_{ii}^{fit}}, \tag{6.45}$$

where C_{ii}^{fit} is the fit error. These distributions are shown in Figure 6.7. The normalised residuals are expected to be Gaussian distributed, with mean zero and variance equal to one. The distributions obtained are compatible with this expectation.

Finally, the resolution of the fit is estimated using a sample of muons generated with an emittance of 4.5 mm rad. The resolution is calculated as the fraction of the residual on the parameter over the beam RMS on the same parameter – see Figure 6.8. The resolutions obtained are better than required for the success of the experiment (14%) and they represent an improvement of $40 - 50\%$ comparatively to previous versions of the reconstruction [151]. The values obtained are also listed in Table 6.1.

The dependance of the resolution on the momentum of the fitted particle

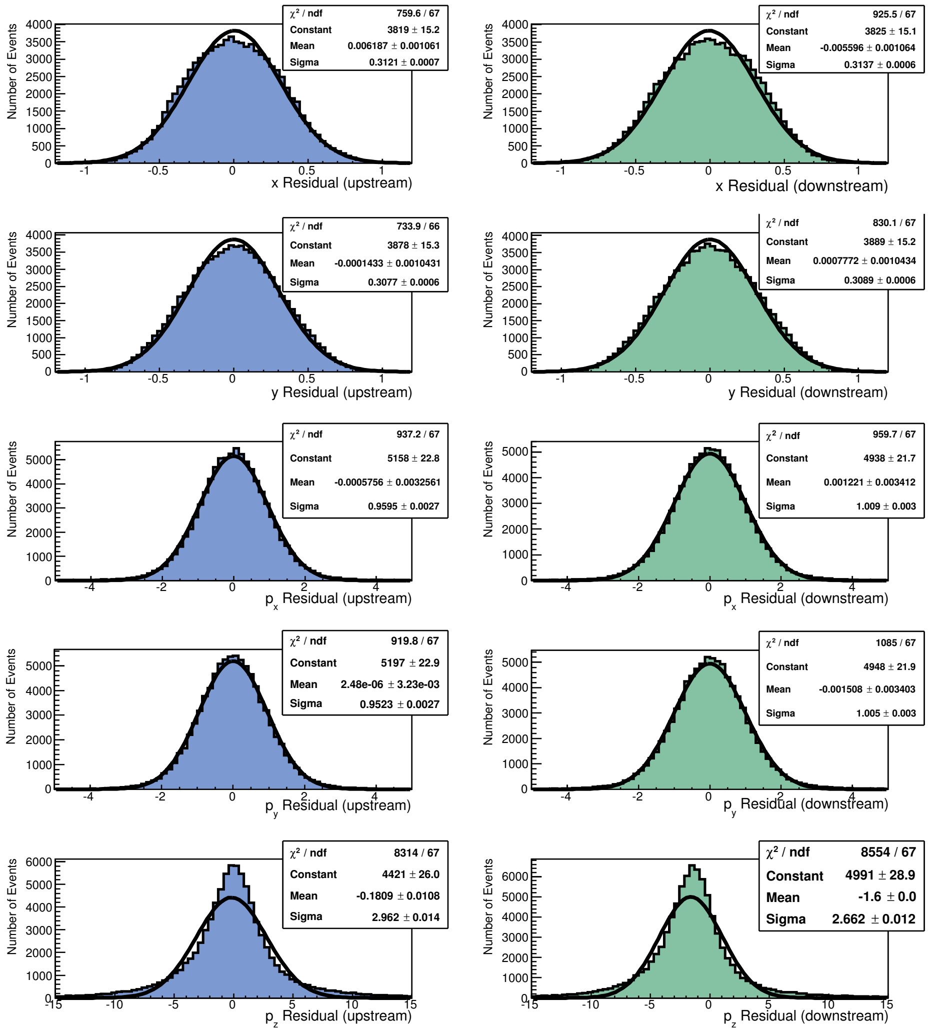

Figure 6.6: Pull on the track parameters. For the transverse position and momentum parameters, the distributions are well fitted by a Gaussian from which we can extract the fit resolution ($\sim 0.31\,\mathrm{mm}$ for position variables, $\sim 1\,\mathrm{MeV/c}$ for transverse momentum). The performance for fitting longitudinal momentum is not as good, in particular because the values estimated are biased. Precision on this parameter will require integration of information from the TOF detectors.

is shown in Figure 6.9.

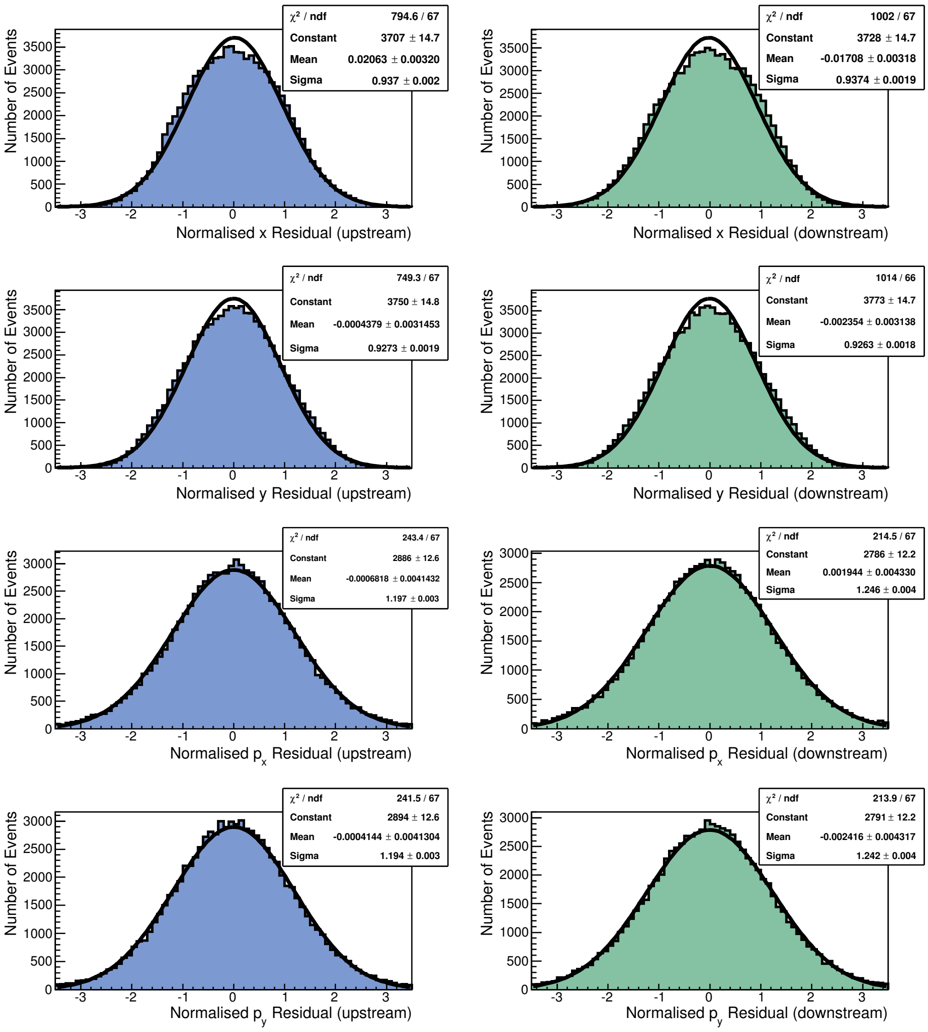

Figure 6.7: Normalised residual for the track parameters. A Gaussian is fitted to each distribution. A standard normal result (mean zero, variance one) means all assumptions in the fit are correct. Small deviations from this are expected.

Table 6.1: Track fit resolution on the track parameters. These are computed from Figure 6.8.

Parameter	Resolution	Relative Resolution (%)
x	0.3 mm	1.1
y	0.3 mm	1.1
p_x	0.6 MeV/c	4.3
p_y	0.6 MeV/c	4.3

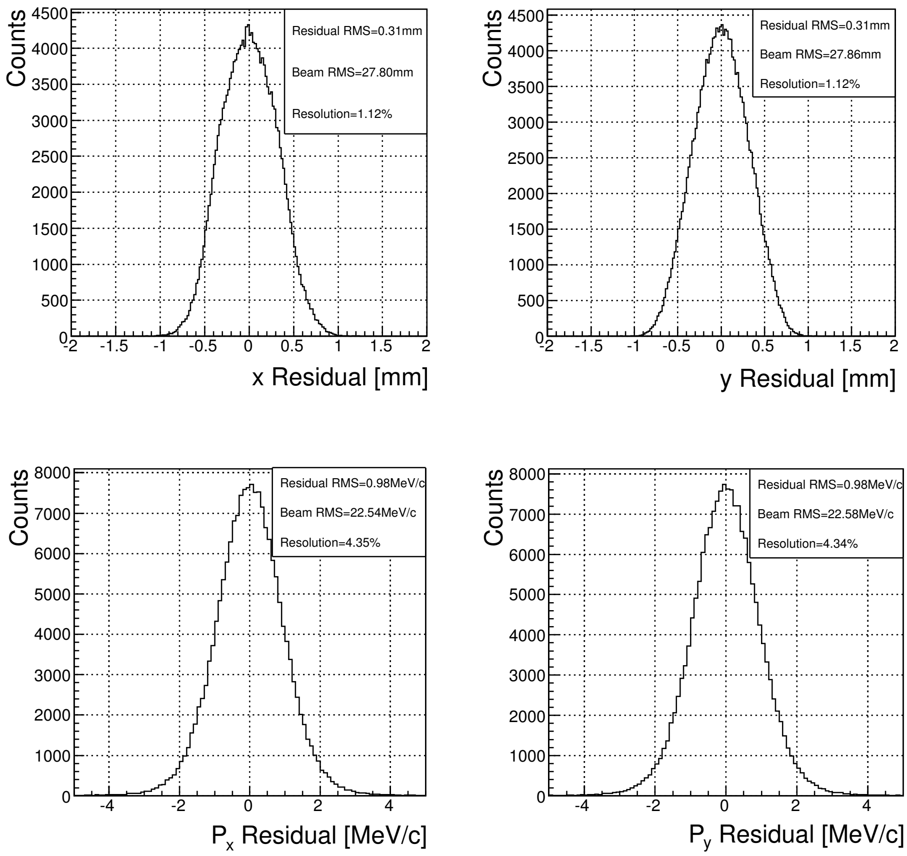

Figure 6.8: Residuals for track parameters, computed as the difference between the reconstructed and the true values. The RMS value of the beam distribution for each parameter is also shown and used to calculate the percentual resolution which is the fraction of the residual RMS over the beam RMS.

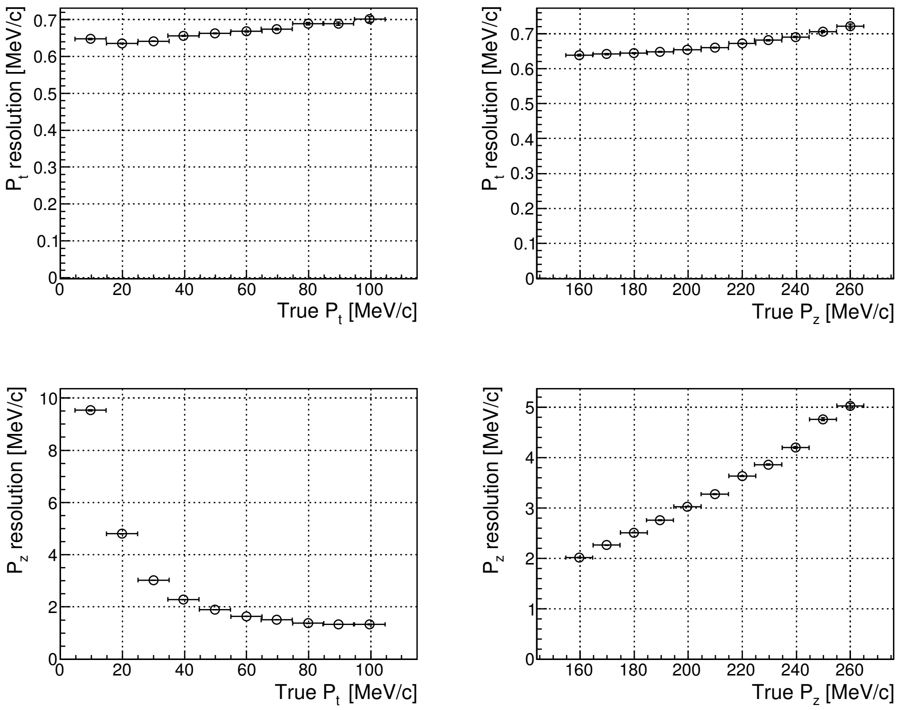

Figure 6.9: Dependance of the transverse and longitudinal momentum resolution on the true momentum. The sample used contains muons generated with emittance in the interval [0.5, 9.5] πmm.

6.9 Emittance Resolution

Using the precise reconstruction of the track parameters, the emittance of the muon beam transversing the SciFi detectors can be calculated. In this section, the accuracy of that measurement is analysed. Using Equation 5.3, the 4D emittance can be calculated with precision, using the SciFi measurements alone. The histograms shown in Figure 6.10 result from the simulation of a muon beam with emittance $4.5\,\pi$mm. The percentual emittance resolution is computed as:

$$\epsilon_{res} = \frac{\epsilon_{recon} - \epsilon_{MC}}{\epsilon_{MC}} \times 100; \tag{6.46}$$

where each emittance value is calculated using ensembles of two thousand particles. This resolution is biased due to reconstruction effects (Figure 6.10, top). By generating correction matrices from an independent sample of muons with the same emittance, the resolution found when applying a correction, computed using Equation 5.8, is shown in Figure 6.10, bottom.

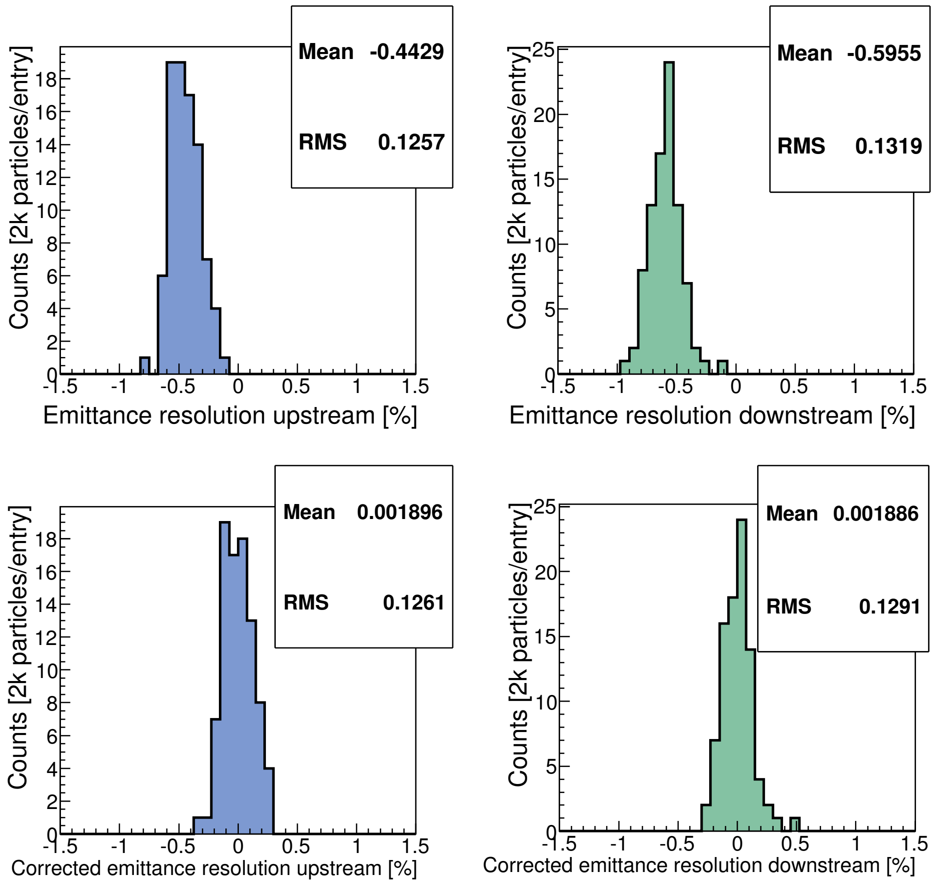

Figure 6.10: Reconstructed emittance before unfolding (top) and after unfolding (bottom). The emittance values after correction are unbiased and the resolution is $\sim 0.1\%$.

6.10 Conclusion

In this Chapter, a Kalman Filter capable of handling straight and helical tracks travelling across the MICE SciFi spectrometers was developed. The high resolution on the track parameters was demonstrated and it is better than the minimum required for the success of the experiment. The fitting routine can handle multiple scattering, energy loss, detector misalignments and it provides a confidence test for the quality of the fitted track. The emittance resolution achievable is 0.1%.

The robustness against the failure of the Gaussian assumptions could be improved by using a Gaussian Sum Filter [164]. In this approach, the probability distribution functions of the measurement and multiple scattering errors is better approximated by a sum of gaussians; the fit would be repeated for each gaussian and the final result would be a weighted sum of all fits.

Using the SciFi spectrometers alone, high precision in position and transverse momentum are achievable. This leads to a high precision measurement of the 4D emittance. In order to achieve the same precision in the 6D emittance, TOF information which will add precision to the longitudinal momentum needs to be added. The standard approach to achieve this would consist of adding the TOF measurement planes to the Kalman fit. However, this approach might introduce issues related to the extrapolation of the covariance matrix over such large distances as the separation between the TOF and the SciFi spectrometers, through a beam line with magnetic fields and for which the transport equations might be non-trivial. In a minimalistic approach, information can be added and potential problems avoided by simply improving the p_z estimation at the start of the fit with the TOF measurements.

7 Summary and Conclusions

Constraining cross section and beam systematic uncertainties will be essential for the discovery of CP violation in the neutrino sector and the determination of the neutrino mass hierarchy. This thesis comprises work related with both the production of neutrino beams and the measurement of neutrino-nucleus cross sections.

The MICE collaboration is due to demonstrate ionization cooling in the near future thereby allowing the performance of the Neutrino Factory cooling channel to be estimated with confidence. The precise tracking of muons in the MICE lattice will benefit from the Kalman Filter developed in this work which performs better than the requirement for the success of the experiment: the resolution achieved is 1.1% for position coordinates and 4.3% for transverse momentum components.

The measurement of the cross sections for CC coherent pion production in the ArgoNeuT detector, using a very limited exposure, is a demonstration of the capabilities of the liquid argon technique. This is the first time this interaction has been measured in a liquid argon detector and the first time it has been measured using an automated analysis. The cross sections measured were $2.6^{+1.2}_{-1.0}(stat)^{+0.3}_{-0.4}(syst) \times 10^{-38}\mathrm{cm}^2/\mathrm{Ar}$ for neutrinos at a mean energy of 9.6 GeV and $5.5^{+2.6}_{-2.1}(stat)^{+0.6}_{-0.7}(syst) \times 10^{-39}\mathrm{cm}^2/\mathrm{Ar}$ for antineutrinos at a mean energy of 3.6 GeV. These results are in good agreement with the Rein-Sehgal model.

Bibliography

[1] S. F. King. "Neutrino mass". In: *Contemp. Phys.* 48 (2007), pp. 195–211.

[2] B. Pontecorvo. "Neutrino Experiments and the Problem of Conservation of Leptonic Charge". In: *Sov. Phys. JETP* 26 (May 1968), p. 984.

[3] Z. Maki, M. Nakagawa and S. Sakata. "Remarks on the Unified Model of Elementary Particles". In: *Prog. Theor. Phys.* 28.5 (1962), pp. 870–880.

[4] J. Beringer and others (Particle Data Group). "Neutrino mass". In: *Phys. Rev.* D 86 (2012 and 2013 partial update for the 2014 edition), p. 010001.

[5] K. Abe et al. "Evidence of electron neutrino appearance in a muon neutrino beam". In: *Phys. Rev.* D 88 (3 2013), p. 032002.

[6] X. Guo et al. "A Precision measurement of the neutrino mixing angle θ_{13} using reactor antineutrinos at Daya-Bay". In: arXiv:hep-ex/0701029 (2007).

[7] P. Di Bari. "An introduction to leptogenesis and neutrino properties". In: *Contemp. Phys.* 53.4 (2012), pp. 315–338.

[8] S. Schael et al. "Precision electroweak measurements on the Z resonance". In: *Phys. Rept.* 427 (2006), pp. 257–454.

[9] J. Lesgourgues and S. Pastor. "Neutrino Mass from Cosmology". In: *Advances in High Energy Physics* 2012 (2012), p. 34.

[10] P. A. R. Ade et al. "Planck 2013 results. XVI. Cosmological parameters". In: arXiv:1303.5076 (2013).

[11] C. L. Bennett et al. “Nine-Year Wilkinson Microwave Anisotropy Probe (WMAP) Observations: Final Maps and Results”. In: *Astrophys. J. Suppl.* 208 (2013), p. 20.

[12] G. Hinshaw et al. “Nine-Year Wilkinson Microwave Anisotropy Probe (WMAP) Observations: Cosmological Parameter Results”. In: *Astrophys. J. Suppl.* 208 (2013), p. 19.

[13] C. L. Reichardt et al. “New limits on Early Dark Energy from the South Pole Telescope”. In: *Astrophys. J.* 749 (2012), p. L9.

[14] J. L. Sievers et al. “The Atacama Cosmology Telescope: Cosmological parameters from three seasons of data”. In: *JCAP* 1310 (2013), p. 060.

[15] K. T. Story et al. “A Measurement of the Cosmic Microwave Background Damping Tail from the 2500-square-degree SPT-SZ survey”. In: *Astrophys. J.* 779 (2013), p. 86.

[16] B. Pontecorvo. “Neutrino Experiments and the Problem of Conservation of Leptonic Charge”. In: *Sov. Phys. JETP* 26 (1968), pp. 984–988.

[17] C. L. Cowan et al. “Detection of the Free Neutrino: A Confirmation”. In: *Science* 124 (1956), pp. 103–104.

[18] K. Zuber. *Neutrino Physics*. Series in High Energy Physics, Cosmology and Gravitation. Taylor & Francis, 2003.

[19] L. Wolfenstein. “Neutrino oscillations in matter”. In: *Phys. Rev.* D 17 (9 1978), pp. 2369–2374.

[20] J. N. Bahcall, A. M. Serenelli and S. Basu. “New solar opacities, abundances, helioseismology, and neutrino fluxes”. In: *Astrophys. J.* 621 (2005), pp. L85–L88.

[21] B. T. Cleveland et al. “Measurement of the Solar Electron Neutrino Flux with the Homestake Chlorine Detector”. In: *Astrophys. J.* 496.1 (1998), p. 505.

[22] T. K. Gaisser and M. Honda. “Flux of atmospheric neutrinos”. In: *Ann. Rev. Nucl. Part. Sci.* 52 (2002), pp. 153–199.

[23] T. Kajita. “Atmospheric Neutrinos”. In: *Adv. High Energy Phys.* 2012 (2012).

[24] Y. Fukuda et al. “Evidence for Oscillation of Atmospheric Neutrinos”. In: *Phys. Rev. Lett.* 81 (8 1998), pp. 1562–1567.

[25] K. S. Hirata et al. “Observation in the Kamiokande-II detector of the neutrino burst from supernova SN1987A”. In: *Phys. Rev.* D 38 (2 1988), pp. 448–458.

[26] J. C. Van Der Velde et al. “Neutrinos from SN1987A in the IMB detector”. In: *Nucl. Instrum. Meth. A* 264 (1988), pp. 28–31.

[27] C. Athanassopoulos et al. “The Liquid scintillator neutrino detector and LAMPF neutrino source”. In: *Nucl. Instrum. Meth.* A 388 (1997), pp. 149–172.

[28] A. Aguilar et al. “Evidence for neutrino oscillations from the observation of ν_e appearance in a ν_μ beam”. In: *Phys. Rev.* D 64 (11 2001), p. 112007.

[29] A. A. Aguilar-Arevalo et al. “Unexplained Excess of Electronlike Events from a 1-GeV Neutrino Beam”. In: *Phys. Rev. Lett.* 102 (10 2009), p. 101802.

[30] A. A. Aguilar-Arevalo et al. “Event Excess in the MiniBooNE Search for $\bar{\nu}_\mu \rightarrow \bar{\nu}_e$ Oscillations”. In: *Phys. Rev. Lett.* 105 (18 2010), p. 181801.

[31] B. Armbruster et al. “KARMEN limits on electron-neutrino $\rightarrow$ tau-neutrino oscillations in two neutrino and three neutrino mixing schemes”. In: *Phys. Rev.* C 57 (1998), pp. 3414–3424.

[32] C. Giunti and M. Laveder. “Short-baseline electron neutrino disappearance, tritium beta decay, and neutrinoless double-beta decay”. In: *Phys. Rev.* D 82 (5 2010), p. 053005.

[33] G. Mention et al. “The Reactor Antineutrino Anomaly”. In: *Phys. Rev.* D 83 (2011), p. 073006.

[34] W. Winter. “Neutrino mass hierarchy determination with IceCube-PINGU”. In: *Phys. Rev. D* 88.1 (2013), p. 013013.

[35] Y. F. Li et al. “Unambiguous Determination of the Neutrino Mass Hierarchy Using Reactor Neutrinos”. In: *Phys. Rev.* D 88 (2013), p. 013008.

[36] D. S. Ayres et al. "NOvA: Proposal to build a 30 kiloton off-axis detector to study $\nu_\mu \to \nu_e$ oscillations in the NuMI beamline". In: arXiv:hep-ex/0503053 (2004).

[37] NOvA Collaboration. *NOvA Official Plots and Figures.* 2014. URL: `http://www-nova.fnal.gov/plots_and_figures/plot_and_figures.html` (visited on 01/09/2014).

[38] E. S. Kopp. "Accelerator-based neutrino beams". In: *Phys. Rept.* 439 (2007), pp. 101–159.

[39] C. Adams et al. "The Long-Baseline Neutrino Experiment: Exploring Fundamental Symmetries of the Universe". In: arXiv:1307.7335[hep-ex] (2013).

[40] A. Stahl et al. *Expression of Interest for a very long baseline neutrino oscillation experiment (LBNO).* Tech. rep. CERN-SPSC-2012-021. SPSC-EOI-007. Geneva: CERN, 2012.

[41] P. Zucchelli. "A novel concept for a $\bar{\nu}_e/\nu_e$ neutrino factory: the beta beam". In: *Phys. Lett.* B 532 (2002), pp. 166–172.

[42] S. Geer. "Neutrino beams from muon storage rings: Characteristics and physics potential". In: *Phys. Rev.* D 57 (1998), pp. 6989–6997.

[43] A. Bandyopadhyay et al. "Physics at a future Neutrino Factory and super-beam facility". In: *Rept. Prog. Phys.* 72 (2009), p. 106201.

[44] J. Kopp P. Coloma P. Huber and W. Winter. "Systematic uncertainties in long-baseline neutrino oscillations for large θ_{13}". In: *Phys. Rev.* D 87 (3 2013), p. 033004.

[45] A. Skrinsky and V. Parkhomchuk. "Cooling Methods for beams of charged particles". In: *Sov. J. Part. Nucl.* 12 (1981), pp. 223–247.

[46] U. Bravar et al. "MICE: the Muon Ionization Cooling Experiment. Step I: First Measurement of Emittance with Particle Physics Detectors". In: arXiv:1110.1813 (2011).

[47] R. Barlow et al. "EMMA–The worlds first non-scaling FFAG". In: *Nucl. Instrum. Meth. A* 624.1 (2010), pp. 1 –19.

[48] S. Choubey et al. "International Design Study for the Neutrino Factory, Interim Design Report". In: arXiv:1112.2853[hep-ex] (2011).

[49] D. Adey et al. "nuSTORM - Neutrinos from STORed Muons: Proposal to the Fermilab PAC". In: arXiv:1308.6822 (2013).

[50] J. G. Morfin, J. Nieves and J. T. Sobczyk. "Recent Developments in Neutrino/Antineutrino - Nucleus Interactions". In: *Adv. High Energy Phys.* 2012 (2012), p. 934597.

[51] S. S. Gerstein and Y. B. Zeldovich. In: *Sov. Phys. JETP* 2 (1956), p. 576.

[52] R. P. Feynman and M. Gell-Mann. "Theory of the Fermi Interaction". In: *Phys. Rev.* 109 (1 1958), pp. 193–198.

[53] S. L. Adler. "Tests of the Conserved Vector Current and Partially Conserved Axial-Vector Current Hypotheses in High-Energy Neutrino Reactions". In: *Phys. Rev.* 135 (4B 1964), B963–B966.

[54] F. J. Hasert et al. "Observation of neutrino-like interactions without muon or electron in the gargamelle neutrino experiment". In: *Phys. Lett.* B 46.1 (1973), pp. 138 –140.

[55] E. J. Konopinski. "Beta-Decay". In: *Rev. Mod. Phys.* 15 (4 1943), pp. 209–245.

[56] D. Z. Freedman. "Coherent effects of a weak neutral current". In: *Phys. Rev.* D 9 (5 1974), pp. 1389–1392.

[57] A. J. Anderson et al. "Coherent neutrino scattering in dark matter detectors". In: *Phys. Rev.* D 84 (1 2011), p. 013008.

[58] K. Scholberg. "Prospects for measuring coherent neutrino-nucleus elastic scattering at a stopped-pion neutrino source". In: *Phys. Rev.* D 73 (3 2006), p. 033005.

[59] D. Akimov et al. "Detection of reactor antineutrino coherent scattering off nuclei with a two-phase noble gas detector". In: *JINST* 4.06 (2009), P06010.

[60] E. Santos et al. "Single electron emission in two-phase xenon with application to the detection of coherent neutrino-nucleus scattering". In: *JHEP* 2011.12 (2011), pp. 1–20.

[61] D. Y. Akimov et al. "Prospects for observation of neutrino-nuclear neutral current coherent scattering with two-phase Xenon emission detector". In: *JINST* 8 (2013), P10023.

[62] C. H. Llewellyn Smith. “Neutrino reactions at accelerator energies”. In: *Phys. Rep.* 3.5 (1972), pp. 261 –379.

[63] N. J. Baker et al. “Quasielastic neutrino scattering: A measurement of the weak nucleon axial-vector form factor”. In: *Phys. Rev.* D 23 (11 1981), pp. 2499–2505.

[64] T. Kitagaki et al. “High-energy quasielastic $\nu_\mu n \to \mu^- p$ scattering in deuterium”. In: *Phys. Rev.* D 28 (3 1983), pp. 436–442.

[65] K. L. Miller et al. “Study of the reaction $\nu_\mu d \to \mu^- p p_s$”. In: *Phys. Rev.* D 26 (3 1982), pp. 537–542.

[66] M. O. Wascko. “Recent Measurements of Neutrino-Nucleus Quasi-Elastic Scattering”. In: *Nucl. Phys. Proc. Supl.* 229-232 (2012), pp. 179–183.

[67] A. M. Ankowski, O. Benhar and N. Farina. “Analysis of the Q^2-dependence of charged-current quasielastic processes in neutrino-nucleus interactions”. In: *Phys. Rev.* D 82 (2010), p. 013002.

[68] R. Gran et al. “Measurement of the quasielastic axial vector mass in neutrino interactions on oxygen”. In: *Phys. Rev.* D 74 (5 2006), p. 052002.

[69] X. Espinal and F. Sanchez. “Measurement of the axial vector mass in neutrino-carbon interactions at K2K”. In: *AIP Conf. Proc.* 967 (2007), pp. 117–122.

[70] A. A. Aguilar-Arevalo et al. “First Measurement of the Muon Neutrino Charged Current Quasielastic Double Differential Cross Section”. In: *Phys. Rev.* D 81 (2010), p. 092005.

[71] M. Dorman. “Preliminary results for CCQE scattering with the MINOS near detector”. In: *AIP Conf. Proc.* 1189 (2009), pp. 133–138.

[72] V. Lyubushkin. “A Study of Quasi-Elastic Muon (Anti)Neutrino Scattering in the NOMAD Experiment”. In: *AIP Conf. Proc.* 1189 (2009), pp. 157–162.

[73] E. A. Paschos, J. Y. Yu and M. Sakuda. “Neutrino production of resonances”. In: *Phys. Rev.* D 69 (2004), p. 014013.

[74] J. A. Formaggio and G. P. Zeller. “From eV to EeV: Neutrino Cross Sections Across Energy Scales”. In: *Rev. Mod. Phys.* 84 (2012), p. 1307.

[75] O. Nachtmann. “Coulomb corrections to Adler’s {PCAC} test in nuclei”. In: *Nucl. Phys.* B 22.2 (1970), pp. 385 –396.

[76] J. S. Bell. “Nuclear Optical Model for Virtual Pions”. In: *Phys. Rev. Lett.* 13 (2 1964), pp. 57–59.

[77] J. S. Bell and C. H. Llewellyn Smith. “Near-forward neutrino reactions on nuclear targets”. In: *Nucl. Phys.* B 24 (1970), pp. 285–304.

[78] K. S. Lackner. “Coherent meson production as a test for neutral weak currents of exotic space-time structure”. In: *Nucl. Phys.* B 153.0 (1979), pp. 526 –545.

[79] H. Faissner et al. “Observation of neutrino and antineutrino induced coherent neutral pion production off Al^{27}”. In: *Phys. Lett.* B 125.2–3 (1983), pp. 230–236.

[80] E. Isiksal, D. Rein and J.G. Morfin. “Evidence for Neutrino- and Antineutrino-Induced Coherent Production”. In: *Phys. Rev. Lett.* 52 (13 1984), pp. 1096–1099.

[81] D. Rein and L. M. Sehgal. “Coherent π^0 production in neutrino reactions”. In: *Nucl. Phys. B* 223.1 (1983), pp. 29 –44.

[82] F. Bergsma et al. “Measurement of the Cross-section of Coherent π^0 Production by Muon Neutrino and Anti-neutrino Neutral Current Interactions on Nuclei”. In: *Phys. Lett.* B 157 (1985), p. 469.

[83] H.-J. Grabosch et al. “Coherent pion production in neutrino and antineutrino interactions on nuclei of heavy freon molecules”. In: *Z Phys. C Part. Fields* 31.2 (1986), pp. 203–211.

[84] P. Marage et al. “Coherent single pion production by antineutrino charged current interactions and test of PCAC”. In: *Z Phys. C Part. Fields* 31.2 (1986), pp. 191–197.

[85] M. Hasegawa et al. “Search for coherent charged pion production in neutrino-carbon interactions”. In: *Phys. Rev.Lett.* 95 (2005), p. 252301.

[86] K. Hiraide et al. "Search for Charged Current Coherent Pion Production on Carbon in a Few-GeV Neutrino Beam". In: *Phys. Rev.* D 78 (2008), p. 112004.

[87] Ch. Berger and L. M. Sehgal. "Partially conserved axial vector current and coherent pion production by low energy neutrinos". In: *Phys. Rev.* D 79 (5 2009), p. 053003.

[88] A. A. Aguilar-Arevalo et al. "The MiniBooNE Detector". In: *Nucl. Instrum. Meth.* A 599 (2009), pp. 28–46.

[89] E. A. Paschos and D. Schalla. "Neutrino-induced pion production at low energies and in the small Q^2 region". In: *Adv. High Energy Phys.* 2013 (2013), p. 270792.

[90] L. Alvarez-Ruso et al. "Charged current neutrino induced coherent pion production". In: *Phys. Rev.* C 75 (2007), p. 055501.

[91] E. Hernandez, J. Nieves and M. J. Vicente-Vacas. "Neutrino Induced Coherent Pion Production off Nuclei and PCAC". In: *Phys. Rev.* D 80 (2009), p. 013003.

[92] S. X. Nakamura et al. "Dynamical Model of Coherent Pion Production in Neutrino-Nucleus Scattering". In: *Phys. Rev.* C 81 (2010), p. 035502.

[93] D. Scully. "Neutrino Induced Coherent Pion Production". PhD thesis. University of Warwick, 2013.

[94] A. Higuera et al. "Measurement of Coherent Production of $\pi^{\pm}$ in Neutrino and Anti-Neutrino Beams on Carbon from E_ν of 1.5 to 20 GeV". In: arXiv:1409.3835[hep-ex] (2014).

[95] A. A. Aguilar-Arevalo et al. "Measurement of the neutrino neutral-current elastic differential cross section on mineral oil at $E_\nu \sim 1$ GeV". In: *Phys. Rev.* D 82 (9 2010), p. 092005.

[96] P. Adamson et al. "Measurement of ν_μ and ν_e Events in an Off-Axis Horn-Focused Neutrino Beam". In: *Phys. Rev. Lett.* 102 (21 2009), p. 211801.

[97] A. A. Aguilar-Arevalo et al. "Measurement of ν_μ-induced charged-current neutral pion production cross sections on mineral oil at $E_\nu \in 0.5 - 2.0$ GeV". In: *Phys. Rev.* D 83 (2011), p. 052009.

[98] A. A. Aguilar-Arevalo et al. "First measurement of the muon neutrino charged current quasielastic double differential cross section". In: *Phys. Rev.* D 81 (9 2010), p. 092005.

[99] K. Abe et al. "Measurement of the Inclusive NuMu Charged Current Cross Section on Carbon in the Near Detector of the T2K Experiment". In: arXiv:1302.4908[hep-ex] (2013).

[100] F. D. Snider. "Neutrino Cross Section Measurements at MINERνA". In: *FERMILAB-CONF-12-664-E* (2012).

[101] S. R. Mishra, R. Petti and C. Rosenfeld. "A High Resolution Neutrino Experiment in a Magnetic Field for Project-X at Fermilab". In: *PoS* NUFACT08 (2008), p. 069.

[102] S. Mishra. "HiResMν QE systematic errors". Private communication. 2013.

[103] G. Fanourakis et al. "Study of Low-Energy Anti-Neutrino Interactions on Protons". In: *Phys. Rev.* D 21 (1980), p. 562.

[104] S. Bonetti et al. "Study of Quasielastic Reactions of Neutrino and anti-neutrino in Gargamelle". In: *Nuovo Cim.* A 38 (1977), pp. 260–270.

[105] L. B. Auerbach et al. "Measurements of charged current reactions of muon neutrinos on C-12". In: *Phys. Rev.* C 66 (2002), p. 015501.

[106] S. V. Belikov et al. "Quasielastic Neutrino and Anti-Neutrinos Scattering: Total Cross-Sections, Axial Vector Form-Factor". In: *Z. Phys.* A 320 (1985), p. 625.

[107] J. Brunner et al. "Quasielastic Nucleon and Hyperon Production by Neutrinos and Anti-Neutrinos with Energies below 30-GeV". In: *Z. Phys.* C 45 (1990), p. 551.

[108] W. A. Mann et al. "Study of the reaction $\nu\ n \rightarrow \mu^- p$". In: *Phys. Rev. Lett.* 31 (1973), pp. 844–847.

[109] N. J. Baker et al. "Quasielastic Neutrino Scattering: A Measurement of the Weak Nucleon Axial Vector Form-Factor". In: *Phys. Rev.* D 23 (1981), pp. 2499–2505.

[110] M. R. Whalley. "A New neutrino cross section data resource". In: *Nucl. Phys. Proc. Suppl.* 139 (2005), pp. 241–246.

[111] F. Bergsma et al. “Measurement of the cross section of coherent π^0 production by muon-neutrino and antineutrino neutral-current interactions on nuclei”. In: *Phys. Lett.* B 157.CERN-EP-85-37 (1985), pp. 469 –474.

[112] A. A. Aguilar-Arevalo et al. “First Observation of Coherent π^0 Production in Neutrino Nucleus Interactions with $E_\nu < 2$ GeV”. In: *Phys. Lett.* B 664 (2008), pp. 41–46.

[113] C. T. Kullenberg et al. “A Measurement of Coherent Neutral Pion Production in Neutrino Neutral Current Interactions in NOMAD”. In: *Phys. Lett.* B 682 (2009), pp. 177–184.

[114] Y. Kurimoto et al. “Improved measurement of neutral current coherent π^0 production on carbon in a few-GeV neutrino beam”. In: *Phys. Rev.* D 81 (11 2010), p. 111102.

[115] P. Marage et al. “Coherent production of π^+ mesons in ν-neon interactions”. In: *Z Phys. C Part. Fields* 43.4 (1989), pp. 523–526.

[116] S. Willocq et al. “Coherent production of single pions and ρ mesons in charged-current interactions of neutrinos and antineutrinos on neon nuclei at the Fermilab Tevatron”. In: *Phys. Rev.* D 47 (7 1993), pp. 2661–2674.

[117] P. Vilain et al. “Coherent single charged pion production by neutrinos”. In: *Phys. Lett.* B 313.1–2 (1993), pp. 267–275.

[118] K. Anderson et al. “The NuMI Facility Technical Design Report”. In: (1998).

[119] S. E. Kopp. “The NuMI neutrino beam at Fermilab”. In: *FERMILAB-CONF-05-093-AD* (2005).

[120] C. Anderson et al. “The ArgoNeuT detector in the NuMI low-energy beam line at Fermilab”. In: *JINST* 7 (Oct. 2012), 19P.

[121] P. Adamson et al. “Measurement of Neutrino and Antineutrino Oscillations Using Beam and Atmospheric Data in MINOS”. In: *Phys. Rev. Lett.* 110.25 (2013), p. 251801.

[122] L. Aliaga et al. “Design, Calibration, and Performance of the MINERvA Detector”. In: *Nucl. Instrum. Meth.* A 743 (2014), pp. 130–159.

[123] C. Alt et al. "Inclusive production of charged pions in p+C collisions at 158-GeV/c beam momentum". In: *Eur. Phys. J.* C49 (2007), pp. 897–917.

[124] C. Rubbia. *The liquid-argon time projection chamber: a new concept for neutrino detectors.* Tech. rep. CERN-EP-INT-77-8. Geneva: CERN, 1977.

[125] ArgoNeuT Collaboration. *ArgoNeuT: Mini LArTPC Exposure to Fermilab's NuMI Beam.* 2013. URL: `http://t962.fnal.gov/`.

[126] E. Church for the LArSoft Collaboration. "LArSoft: A Software Package for Liquid Argon Time Proportional Drift Chambers". In: arXiv:1311.6774 (2013).

[127] C. Andreopoulos et al. "The GENIE Neutrino Monte Carlo Generator". In: *Nucl. Instrum. Meth.* A 614 (2010), pp. 87–104.

[128] S. Agostinelli et al. "Geant4a simulation toolkit". In: *Nucl. Instrum. Meth. A* 506.3 (2003), pp. 250 –303.

[129] J. Birks. "Scintillations from Organic Crystals: Specific Fluorescence and Relative Response to Different Radiations". In: *Proc. Phys. Soc. A* 64 (1951), p. 874.

[130] P. Cennini et al. "Performance of a three-ton liquid argon time projection chamber". In: *Nucl. Instrum. Meth. A* 345.2 (1994), pp. 230 –243.

[131] J. Spitz. "Measuring Muon-Neutrino Charged-Current Differential Cross Sections with a Liquid Argon Time Projection Chamber". PhD thesis. Yale University, [FERMILAB-THESIS-2011-36], 2011.

[132] M. Ester et al. "A density-based algorithm for discovering clusters in large spatial databases with noise". In: AAAI Press, 1996, pp. 226–231.

[133] A. A. Aguilar-Arevalo et al. "Unexplained Excess of Electronlike Events from a 1-GeV Neutrino Beam". In: *Phys. Rev. Lett.* 102 (10 2009), p. 101802.

[134] A. Hoecker et al. "TMVA: Toolkit for Multivariate Data Analysis". In: *PoS* ACAT (2007), p. 040.

[135] L. Rokach. *Data Mining with Decision Trees: Theory and Applications*. World Scientific, 2008.

[136] J. H. Friedman. "Stochastic gradient boosting". In: *Comput. Stat. Data An.* 38.4 (2002). Nonlinear Methods and Data Mining, pp. 367 –378.

[137] Y. Freund and R. E. Schapire. "A Decision-Theoretic Generalization of On-Line Learning and an Application to Boosting". In: *J. Comput. Syst. Sci.* 55.1 (1997), pp. 119 –139.

[138] S. Baker and R. D. Cousins. "Clarification of the use of CHI-square and likelihood functions in fits to histograms". In: *Nucl. Instrum. Methods* 221 (1984), pp. 437–442.

[139] P. Adamson et al. "Neutrino and Antineutrino Inclusive Charged-current Cross Section Measurements with the MINOS Near Detector". In: *Phys. Rev.* D 81 (2010), p. 072002.

[140] A. McGowan. "Observation of a Deficit in NuMI Neutrino-induced Rock and Non-fudical Muons in the MINOS Far Detector and Measurement of Neutrino Oscillation Parameters". PhD thesis. University of Minnesota, 2003.

[141] H.-J. Grabosch et al. "Coherent pion production in neutrino and antineutrino interactions on nuclei of heavy freon molecules". In: *Z Phys. C Part. Fields* 31.2 (1986), pp. 203–211.

[142] K. Takayama. "Note on the Courant and Snyder Invariant". In: *IEEE T. Nucl. Sci.* 30 (Aug. 1983), pp. 2412–+.

[143] J. Liouville. "Note on the Courant and Snyder Invariant". In: *J. Math. Pures. Appl.* 16 (1837).

[144] P. M. Lapostolle. "Emittance, Entropy and Information". In: *IEEE Trans. Nucl. Sci.* NS-18 (1971), pp. 1101–1104.

[145] T. L. Hart and D. M. Kaplan. "Emittance Measurement in MICE". In: (2008).

[146] A. Fish. *Construction and testing of the scintillating fibre trackers for MICE.* Ph.D. Thesis, Blackett Laboratory, Imperial College of London. 2009.

[147] G. Gregoire et al. “An International Muon Ionization Cooling Experiment (MICE)”. In: *MICE Note* 167 (2003).

[148] Rutherford Appleton Lab. “Rutherford Appleton Laboratory”. In: *INIS-GB* 24 (16 1993).

[149] ISIS. *ISIS Pulsed Neutron & Muon Source*. 2014. URL: `http://www.isis.rl.ac.uk/` (visited on 10/07/2014).

[150] M. D. Petroff and M. G. Stapelbroek. “Photon-Counting Solid-State Photomultiplier”. In: *IEEE T. Nucl. Sci.* 36.1, Part 1 (1989), 158–162.

[151] A. Khan et al. “MICE Scintillating-Fibre Tracker First Progress Report”. 90. 2005.

[152] C. Rogers and M. Ellis. “High Precision Measurement of Muon Beam Emittance Reduction in MICE”. 122. 2005.

[153] C. Rogers. “Beam Dynamics in an Ionisation Cooling Channel”. PhD thesis. Imperial College London, 2008.

[154] R. E. Kalman. “A New Approach to Linear Filtering and Prediction Problems”. In: *T. ASME–J. Basic Eng.* 82.Series D (1960), pp. 35–45.

[155] R. Fruhwirth. “Application of Kalman filtering to track and vertex fitting”. In: *Nucl. Instrum. Methods Phys. Res. A* 262.HEPHY-PUB-503 (1987), 444. 19 p.

[156] P. Billoir. “Track fitting with multiple scattering: A new method”. In: *Nucl. Instrum. Methods* 225.2 (1984), pp. 352 –366.

[157] R. K. Bock et al. “Data Analysis Techniques for High-Energy Physics Experiments”. In: ed. by M. Regler. Cambridge University Press, 1990. Chap. Track and Vertex Fitting, pp. 240–333.

[158] B. D. O. Anderson and J. B. Moore. *Optimal Filtering*. Dover Books on Electrical Engineering. Dover Publications, 2012.

[159] K. Reif et al. “Stochastic stability of the discrete-time extended Kalman filter”. In: *IEEE T. Automat. Contr.* 44 (1999), pp. 714 –728.

[160] V. L. Highland. “Some practical remarks on multiple scattering”. In: *Nucl. Instrum. Methods* 129.2 (1975), pp. 497 –499.

[161] R. Harr. “Calculation of track and vertex errors for detector design studies”. In: *IEEE T. Nucl. Sci.* 42.3 (1995), pp. 134–147.

[162] W-M Yao et al. “Review of Particle Physics”. In: *J. Phys. G: Nucl. Part. Phys.* 33.1 (2006), p. 1.

[163] R. Fruhwirth, T. Todorov and M. Winkler. “Estimation of detector alignment parameters using the Kalman filter with annealing”. In: *Journal of Physics G: Nuclear and Particle Physics* 29.3 (2003), p. 561.

[164] R. Fruhwirth and M. Regler. “On the quantitative modelling of core and tails of multiple scattering by Gaussian mixtures”. In: *Nucl. Instrum. Meth. A* 456.3 (2001), pp. 369 –389.